Titre: Title:	Thermal Decomposition of a Rare Earth Ore
Auteur: Author:	Adrian Carrillo Garcia
Date:	2019
Type:	Mémoire ou thèse / Dissertation or Thesis
Référence: Citation:	Carrillo Garcia, A. (2019). Thermal Decomposition of a Rare Earth Ore [Thèse de doctorat, Polytechnique Montréal]. PolyPublie. https://publications.polymtl.ca/4147/

POLYTECHNIQUE MONTRÉAL

affiliée à l'Université de Montréal

Thermal Decomposition of a Rare Earth Ore

ADRIÁN CARRILLO GARCÍA

Département de génie chimique

Thèse présentée en vue de l'obtention du diplôme de *Philosophiæ Doctor*

Génie chimique

Novembre 2019

POLYTECHNIQUE MONTRÉAL

affiliée à l'Université de Montréal

Cette thèse intitulée :

Thermal Decomposition of a Rare Earth Ore

présentée par **Adrián CARRILLO GARCÍA**

en vue de l'obtention du diplôme de *Philosophiæ Doctor*

a été dûment acceptée par le jury d'examen constitué de :

Louis FRADETTE, président
Jamal CHAOUKI, membre et directeur de recherche
Daria Camilla BOFFITO, membre
Chen XIA, membre externe

DEDICATION

To my beloved family and Papi Paco may he rest in peace

ACKNOWLEDGEMENTS

Acknowledgements goes first to the supervisor of the project, but hoping this action is not misunderstood as lack of respect to the people that welcomed me into this adventure, I would like to turn the tides and acknowledge first and foremost my grand father, who was and will always be a source of inspiration and a model to follow in the future to come; and my father and mother, whose tangible and intangible sacrifices allowed me to pursue this path.

Returning to the core of this adventure, I would like to express my gratitude to my supervisor, Pr. Jamal Chaouki, for his guidance, conviction power to turn me into Ph.D. and friendship. With all the technical knowledge Pr. Chaouki transferred to me, I just hoped that I was able to repay some of this gratitude to him by guiding him towards a better vision about football, I completely failed but at least we had nice discussions. Pr. Chaouki, I thank you for everything you have done for me.

In this long trip that is a PhD I also had the guidance and great support of Dr Mohammad Latifi, whom I consider a friend. He encouraged me to grow my scientific thinking and advised me in other aspects of life.

I would also like to express my appreciations to my colleagues, members of PEARL research group, for the many discussions we had during our meetings and encounters. My apologies for not mentioning you by name but the list of members is too long. And to the NAA lab for all the hard work they put to accelerate our projects, thank you Cornelia Chilian, Maryam and Darren.

At Polytechnique we also have amazing technicians who helped me a lot especially during the first years where finding reagents or building a setup was not so obvious, thank you to you all, Gino, Martine, Sylvain, Daniel, Sébastien and Robert. I am also thankful to the Chemical Engineering Department, professors and staff.

Changing course to slightly get away from the research and work, I would like to thank you the group of amazing people and friends I met along the years, Navid, Iván, Julien, Charles, Mario and Jihène, may all transport phenomena laws be with you, Emma, Matthieu (I won't miss our TGA discussions), Hamed and El Mahdi. Having you around was a pleasure. But let's not forget the friends that even from abroad were able to cheer me up, Javier, Jorge, Daniela, Lor, Myriam and

Los Vergas (Charly, Martinxo, Guille, Serpo, Mario, Iker San, Miguel y Fer), we will meet soon Beverly T26 Team.

Also, I would not be here if it weren't for Anne Sophie, thank you for welcoming me in Montreal and for having time for me.

Last but not least, I'm grateful to my partner and my family. They were the pillar that hold me when I needed the most. Fatma, thank you for your support and patience during the PhD and for every time I came to you insomniac or with a new injury from football. Dear family, thank you for your long-distance support, the sacrifices you made for me are unmeasurable.

Time for a new adventure.

RÉSUMÉ

Les terres rares (REE) sont des métaux représentés par le Scandium, l'Yttrium et le groupe des lanthanides avec un grand nombre d'applications dans les technologies de pointe. Leur demande croissante, en particulier dans les applications où la durabilité, l'efficacité élevée et les faibles émissions de carbone sont obligatoires, e.g. les aimants permanents pour les éoliennes, en font un métal critique malgré leur abondance. Contrairement à leur nom « rare », les REE se trouvent dans de nombreux gisements répartis dans le monde. D'autre part, la similitude de leurs propriétés physico-chimiques et leur présence à faible teneur dans la plupart de ces gisements, rend le processus d'extraction extrêmement difficile avec une gamme compliquée de traitements et un impact important sur l'environnement.

Le processus conventionnel de production de terres rares à partir d'un gisement peut être divisé en quatre étapes principales : extraction et broyage, enrichissement physique, hydrométallurgie et séparation individuelle des terres rares. Alors que la première et la dernière étape sont inévitables et des procédés bien connus, l'enrichissement physique et l'hydrométallurgie font souvent l'objet de recherches et ont un effet négatif sur l'environnement. L'utilisation de conditions sévères en particulier, e.g. une température élevée associée à un ratio acide (acide sulfurique) / minerai élevé, est l'une des principales préoccupations.

L'application de traitements à haute température est une alternative pour réduire les émissions de gaz dangereux et désactiver en même temps le fluor. L'efficacité du processus de calcination sur un minerai dépend des formes minérales.

Cette étude a porté sur la production directe d'oxydes de terres rares (REO) par la calcination d'un minerai à base de carbonatite provenant d'un gisement situé à Saguenay, Canada. Le procédé a été effectué entre 700 et 900 °C dans des micro réacteurs à lit fluidisé et des analyses qualitatives (diffraction des rayons X) et quantitatives (QEMSCAN) ont été effectuées avant et après la réaction.

En raison de la composition complexe et hétérogène du minerai, son mécanisme de décomposition a été étudié pour avoir une meilleure compréhension fondamentale du processus de calcination et comprendre la contribution de chaque minéral à la cinétique de réaction globale. Ainsi, en se basant sur le mécanisme réactionnel et de la minéralogie du minerai, les cinétiques de calcination des

minéraux individuels ont été étudiés par analyse thermogravimétrique (TGA), en mettant l'accent sur les minéraux de carbonatites puisqu'ils représentaient environ 79% en poids du minerai.

La comparaison des paramètres de décomposition et de cinétique des minéraux a révélé que la calcination du bastnäsite a lieu à une température beaucoup plus basse (400 ºC) que celle des minéraux de la gangue ; tandis que la monazite ne se décompose pas en dessous de 1000 ºC. Contrairement aux observations sur la calcination de minéraux individuels, l'association de monazite et de calcite dans le minerai a permis de réduire la température de décomposition du phosphate et une production plus élevée d'oxyde de terres rares. En se basant sur des études de décomposition et de cinétique des minéraux du minerai, un modèle cinétique représentant la calcination du minerai de Niobec a été développé. Le modèle qui a été d'abord développé pour les particules de petite taille en raison de sa similarité avec la décomposition individuelle des minéraux, a été adapté à des particules plus grosses.

La calcination a ensuite été effectuée dans un microréacteur à lit fluidisé, où l'avantage de la calcination de particules plus grosses pour augmenter la production d'oxyde de terres rares, a été démontré. Comme l'association de la monazite et de la calcite a joué un rôle majeur dans la décomposition du minerai de phosphate, travailler avec une taille de particule plus grande du minerai a augmenté l'interaction de la monazite avec la calcite. En conséquence, la conversion des minéraux des terres rares en oxydes de terres rares a également augmenté. Une étude morphologique des particules lors de la calcination a montré la formation de fissures (par imagerie BET et SEM) augmentant la porosité des particules. Avec une porosité plus élevée, le gaz dégagé s'est échappé plus rapidement de la particule en évitant la possibilité d'une augmentation de la pression à l'intérieur de la particule pouvant entraîner la rupture de la même ou la présence de réactions inverses.

Le produit calciné a ensuite été lixivié dans des conditions ambiantes avec un acide peu concentré pour solubiliser environ 90% en poids de la matrice principale des éléments de la gangue, à savoir calcium et magnésium. Avec ce processus à deux étapes, la concentration de terres rares a augmenté de 2,1 à 7% en poids dans le matériau solide, ce qui correspond à un taux d'enrichissement de 3,3. Lorsque la calcination a été effectuée sur des particules plus petites, la production d'oxydes de terres rares était plus faible et le taux d'enrichissement est réduit à 2,35.

Comparé aux procédés conventionnels où la récupération maximale de REE est d'environ 50%, cette combinaison de processus pourrait atteindre une récupération de REE de 90%.

Ainsi, contrairement aux techniques conventionnelles d’enrichissement physique où la taille de libération des minéraux de terres rares joue un rôle majeur, le rendement de la calcination augmente avec la taille des particules puisqu’il est possible d’obtenir une meilleure production de REO et une meilleure lixiviation de la gangue. Travailler avec des particules plus grosses pourrait également réduire la consommation d’énergie en amont, c’est-à-dire la section minière, et compenser une partie des besoins élevés en énergie du processus de calcination.

ABSTRACT

Rare earth elements (REE) are metals represented by scandium, yttrium and the lanthanide group with a vast number of applications in advanced technologies. Their increasing demand especially in applications where durability, high efficiency and low carbon emissions are mandatory, e.g. permanent magnets for wind turbines, makes of them a critical metal despite their abundance. Contrary to their name "rare", REE are found in many deposits spread around the world. On the other hand, the similarity between their physico-chemical properties and their presence in low grade in most of those deposits, make the extraction process extremely difficult with a complicated array of treatments and a high environmental impact.

The conventional process for production of rare earths from a deposit can be divided in four main steps: mining and milling, physical beneficiation, hydrometallurgy and REE individual separation. While the first and last steps are unavoidable and well-known process, physical beneficiation and hydrometallurgy are often the focus of study and have a negative effect on the environment. The use of severe conditions, e.g. high temperature combined with high acid (sulfuric acid) to ore ratio, is one of the main concerns.

An alternative to reduce hazardous gas emissions and deactivate fluorine at the same time is the application of high temperature treatments. The effectivity that the calcination process may have on an ore depends on the mineral forms.

This study focused on the direct production of rare earth oxides (REO) through the calcination of a carbonatite-based ore from a deposit found in Saguenay, Canada. The process was performed between 700 and 900 ºC in micro fluidized bed reactors, and qualitative (X-Ray Diffraction) and quantitative analysis (QEMSCAN) were performed before and after reaction.

Due to the complex and heterogeneous composition of the ore, the decomposition mechanism of the ore was studied to have a better fundamental comprehension of the calcination process and understand the contribution of each mineral to the overall reaction kinetics. So, based on the reaction mechanism and the modal mineralogy of the ore, the calcination kinetics of individual minerals was investigated by thermogravimetric analysis (TGA), with a focus on carbonatite minerals since they represented approximately 79 wt.% of the ore.

The comparison of the decomposition and the kinetic parameters of the minerals revealed that bastnäsite's calcination occurred at much lower temperature (400 ºC) than the gangue minerals; while monazite mineral did not decompose below 1000 ºC. As opposed to the observations of the calcination of individual minerals, the association of monazite with calcite within the ore reduced the decomposition temperature of the phosphate mineral and allowed a higher production of rare earth oxide. Herein, based on the decomposition and kinetics studies of the minerals of the ore, a kinetic model representing the calcination of Niobec's ore was developed. The model developed first for small particle sizes due to its similarity to individual decomposition of minerals, was adapted to bigger particles sizes.

The calcination was then performed in a fluidized bed micro reactor, where the advantage of calcining bigger particles to increase the rare earth oxide production was demonstrated. As the association of monazite with calcite played a major role in the decomposition of the phosphate mineral, working with a bigger particle size of the ore increased monazite's interaction with calcite. As consequence, rare earth minerals conversion to rare earth oxide also increased. A morphological study of the particles during calcination showed the formation of cracks (by BET and SEM imaging) that increased the porosity of particles. With a higher porosity, the evolved gas swept out of the particle faster avoiding the possibility of a pressure increase inside the particle which could result in the breakage of the particle or the presence of reverse reactions.

The calcined product was subsequently leached at ambient conditions with low concentrated acid to solubilize approximately 90 wt.% of the main matrix of gangue elements, i.e. calcium and magnesium. With this two-step process, the concentration of REE increased from 2.1 to 7 wt.% in the solid material, corresponding to a 3.3 enrichment ratio. When calcination was performed on smaller particles, rare earth oxides production was lower, and the enrichment ratio was reduced to 2.35. Compared to the conventional processes where the maximum recovery of REE is around 50%, this combination of processes could attain a 90% REE recovery.

So, as opposed to conventional physical beneficiation techniques where the liberation size of rare earth minerals plays a major role, calcination's performance increases with the particle size since a better REOs production and gangue leaching can be achieved. Working with bigger particles could also reduce the energy consumption upstream, i.e. mining section, and compensate for part of the high energy requirements of the calcination process.

TABLE OF CONTENTS

LIST OF TABLES

LIST OF FIGURES

LIST OF SYMBOLS AND ABBREVIATIONS

FBTGA	Fluidized Bed Thermogravimetric Analyzer
REE	Rare Earth Elements
REO	Rare Earth Oxides

LIST OF APPENDICES

CHAPTER 1 INTRODUCTION

Rare earth elements (REE) are used in many applications affecting the chemical, environmental or metal alloys industries all over the world. They are imbedded in our everyday life as they are also part of all the technological equipment that is used daily, smartphones, computers or televisions. However, their market, controlled by China as main producer, pushed other countries to start their own research and development for rare earth production.

Rare earths production might have different sources, e.g. waste recycling, but their main production is from mining. Although people often think that mining is quite a conventional and known process, REE extraction is a complicated process that depends on the mineralogy of the deposit, e.g. REE bearing minerals and gangue minerals, and the grade of REEs ([1]). The process is thus characterized by two main steps, physical beneficiation and extraction, the latter is often related to hydrometallurgy. The beneficiation process is necessary for the concentration of REE minerals, it is highly dependent on the mineralogy and size of the treated ore; working preferably with lower sizes where minerals are more liberated [2, 3]. On that regard, the process loses efficiency and has a limited REE recovery, often around 50 to 60% [3-5]. In order to increase the REE production efficiency, a new process must be considered, particularly when the REE concentration in the ore is low and the REE minerals have a small liberation particle size. When both conditions are met, the grinding process becomes costly and is related to the production of fine particles that induce higher losses and increase the operating cost. Moreover, as part of the beneficiation process, froth flotation is often used in industry. This technology is related to numerous environmental issues since recyclability of the chemical agents and surfactants used to increase the process performance proves to be difficult. Many research studies on REE extraction focus on this step since a new beneficiation process must be studied and developed for each deposit.

As for physical beneficiation, REE extraction by hydrometallurgy is also dependent on the REE bearing minerals, since in function of the form of the mineral, e.g. carbonatite or phosphate, the digestion step might require more aggressive conditions, i.e. more acidic and higher temperature, as it is the case of sulfuric acid baking. For instance, monazite is often digested with sulfuric acid at temperatures between 220 and 300ºC. This step of the REE processing is problematic due to the high amount of chemicals, that combined with the high temperate are source of production of hazardous compounds, e.g. HF. This generates a waste management issue for the solid and liquid

wastes [6, 7]. As environmental regulations became more stringent, research focuses on more eco-friendly rare earth extraction process. On that behalf, some processes include the deactivation of fluorine which is related to a high temperature treatment of the concentrated ore [8-10]. In less complex terms, this process is related to the thermal decomposition of the concentrated mineral.

Thermal decomposition of minerals involves techniques such as roasting, calcination or chlorination, and has been investigated on different rare earth minerals. These investigations focused on the results of applying thermal cracking on high concentrated rare earth bearing ores. When applied on bastnäsite, the process aims to produce rare earth oxides and capture fluorine by the addition of an agent, often alkali [10-12]. In the case of phosphate minerals, e.g. monazite and xenotime, the addition of an agent aims to reduce the decomposition temperature of the mineral [9, 11, 13-15]. In both cases, a much less aggressive operative conditions may be used downstream to digest the REEs as REE oxides are easier to digest compared to the mineral form.

As previous studies on thermal decomposition focused on the concentrate of the REE mineral, there is a lack of scientific comprehension of the process regarding the decomposition mechanism and kinetics of the decomposition of the ore including the gangue minerals. Only few studies presented the kinetics of the decomposition of REE minerals [12, 16, 17].

This project, in association with Niobec Inc., a Canadian mining company, and the Natural Sciences and Engineering Research Council of Canada (NSERC), focuses on the thermal decomposition of a rare earth ore that contains the REE in the form of bastnäsite (rare earth fluorocarbonate) and monazite (rare earth phosphate). Applying a high temperature treatment on the natural ore aims to decompose the main minerals into a metal oxide and modify the morphology of the particles. Both actions combined would thus be able to open a new path for the extraction of the rare earth oxides. As thermal decomposition of an ore undergoes a complex transformation due to the heterogeneous composition of the ore, a comprehensive study focusing on the mechanism and kinetics of the reaction was investigated. With the appropriate understanding of the reaction mechanism, the importance of the mineral association during the thermal decomposition will be highlighted as a possibility to reduce the decomposition temperatures of some minerals. The kinetic study could set a basis for future calcination studies of a complex carbonatite base ore.

CHAPTER 2 LITERATURE REVIEW

2.1 Introduction – What are the rare earth elements?

Rare earth elements (REE) are a group of seventeen metals represented in the Mendeleev periodic table by the lanthanides, scandium and yttrium. These elements can be divided in two main groups, the light rare earths (LREE) with atomic number from 52 to 62, scandium and yttrium, and the heavy rare earth (HREE) with atomic number from 63 to 71. Despite the impression their name might give, the abundance of some of these elements on the earth's crust is high, for instance, cerium, with 68 ppm, is more abundant than gold or silver [1, 18]. The subjectivity of advertising them as "rare" is due to their low-grade presence in deposits and similar physico-chemical properties which renders their extraction difficult, and as a result, their economical exploitation is often non viable [18, 19].

Rare earth elements are soft iron gray to silvery metals, malleable, ductile and reactive, especially at high temperature [1]. In nature, REEs do not occur in the elemental state, and are found as mixtures in minerals [1, 20]. They have, most of the time, 3+ valences. Some exceptions are europium and cerium which can also form 2+ and 4+ valences respectively, depending on the temperature, pressure, composition and redox conditions [21]. Since chemical interaction of atoms is governed by the outer electrons, the similar configuration of the outer electrons (3+) of rare earth elements causes challenges in the separation and purification of REEs [1, 21].

The 3+ valance rare earth are the main form of REEs and are found in more than 200 minerals, from which the LREEs minerals are more abundant than the HREEs. Bastnäsite, monazite and xenotime are some of the richer rare earth containing and exploitable minerals in the earth crust (Table 2. 1) [1, 18, 19, 22, 23].

Table 2. 1 REE bearing minerals and gangue minerals from deposits [1, 3, 24]

Type of mineral	Mineral	Formula	REO (wt.%)	Main deposits
Carbonate	Ancylite	$Sr(Ce,La)(CO_3)_2OH \cdot H_2O$	46	Weishan (China)
	Bastnäsite	**$(Ce,La)CO_3F$**	**74**	**Bayan Obo (China) Mountain Pass (USA)**
	Parisite	$Ca(RE)_2(CO_3)_3F_2$	59	Bayan Obo (China)
Phosphate	Apatite	$Ca_5(PO_4)_3(F,Cl,OH)$	19	Kola Peninsula (Russia)
	Britholite	$(RE,Ca)_5(SiO_4,PO_4)_3(F,OH)$	56	Kola Peninsula (Russia)
	Monazite	**$(RE,Th)PO_4$**	**35-71**	**Bayan Obo (China)**
	Xenotime	**YPO_4**	**61**	**Mt Weld (Australia)**
Oxide	Brannerite	$(U,RE,Ca)(Ti,Fe)_2O_6$	6	Elliot Lake (Canada)
	Perovskite	$(Ca,RE)TiO_3$	<37	Powderhorn (USA)
Silicate	Allanite	$(RE,Ca)_2(Al,Fe)_3(SiO_4)_3(OH)$	30	Alice Springs(Australia)

2.2 Market and Application of Rare Earth Elements

2.2.1 Market

Despite their discovery in the late 18th century, industrial rare earth elements production started during the 1950's mainly by Brazil, India and South Africa [25, 26]. Later, in the early 1960's, Mountain Pass mine (California) started to operate, and gave the upper hand of REE world production to United States. By the beginning of the 1980's, United States was the biggest REE producer in the world, until China's production emerged in the same period. That's when REE production in the rest of the world started to dwarf.

In the late 1980's, China started to take over the rare earth market with the exploitation of the mine of Bayan Obo, which is nowadays the biggest REE producer. The discovery and operation of new mines in China reduced at the same time the cost of REEs and the competition. Since then and driven by the ceased production of Molycorp's Mountain Pass deposit in the early 2000's, China controls the rare earth market, and in 2011, was producing 95% of the REEs in the world (Table 2. 2) [27]. During this time it presented three different strategies of production: liberalization (late 1970's – early 2000's), focused on the establishment of local industrial processes; mild regulation (early 2000's – 2009), with the objective to have the industry at the service of the government and involved a taxes reduction; and "reregulations" (2009 – present), during which new export quotas

and restrictions were introduced [28]. These quotas can be found in a recent publication and were introduced to have a better control over the environmental impact, and encourage domestic technology and production [29]. The latter triggered a bubble in the rare earth market, increasing REEs' prices by more than 1000% for some specific rare earths [29-31]. The export quotas were abolished in March 2015, after the World Trade Organization ruled against them in December 2014 [31].

Table 2. 2 World's rare earth production: 2009-2015 [32-38]

Year	Rare earth production (Mton)				China's production (%)
	China	US	India	World total production	
2009	120000	0	2700	124000	96.8
2010	130000	0	2700	133000	97.7
2011	130000	0	2800	133000	97.7
2012	95000	7000	2800	110000	86.4
2013	100000	4000	2900	110000	90.9
2014	95000	7000	3000	110000	86.4
2015	105000	4100	NA	124000	84.5

As a result of China's monopoly of the last two decades, countries from the rest of the world started to invest in exploration and production of REEs [39-41]. Although Mountain Pass production has environmental and economical issues to restart their production [31, 42], the emergence of two main commercial plants from Lynas Corporation, Mount Weld in Western Australia in 2011 and Lynas Advanced Material Plant (LAMP) in Malaysia in 2013, has weakened China's dominancy over REE's (Table 2. 2). On that regard, to mitigate supply risks, Canada invested to build up a national network to develop rare earth extraction from domestic deposits [30, 43]. Some

estimations regarding the market of rare earth elements have been made to evaluate the possibility of market inclusion for countries other than China [30, 44].

2.2.2 Applications

Due to the physical and chemical properties of each element, REEs have had applications in many sectors of industry over the past decade [1, 40, 41, 45, 46]. Their increasing demand is particularly growing in energy, environment and high technology fields where low carbon emissions and durability are required. Even, some of those high technology products rely on REEs and can be categorized into mature and emerging applications [47]. Mature applications are well-known technologies such as metal alloys, catalysts or lightning, while emerging ones have high potential of development, such as permanent magnets. Even if their demand is almost equally distributed between these two categories, the demand of individual rare earth elements is very different [1, 30, 43]. Nowadays, emerging applications cover 85% of praseodymium, dysprosium and especially neodymium's market. The latest is used in permanent magnets, which is a highly demanded product employed in transportation, renewable power, e.g. wind turbines, national defense or medical imaging [30, 43, 48, 49].

Some other renewable applications of REEs are in solar panels for the photovoltaic cells (cerium and europium mainly) or electric and hybrid vehicles (lanthanum) [43, 48, 50]. Main REEs applications are summarized in Figure 2. 1.

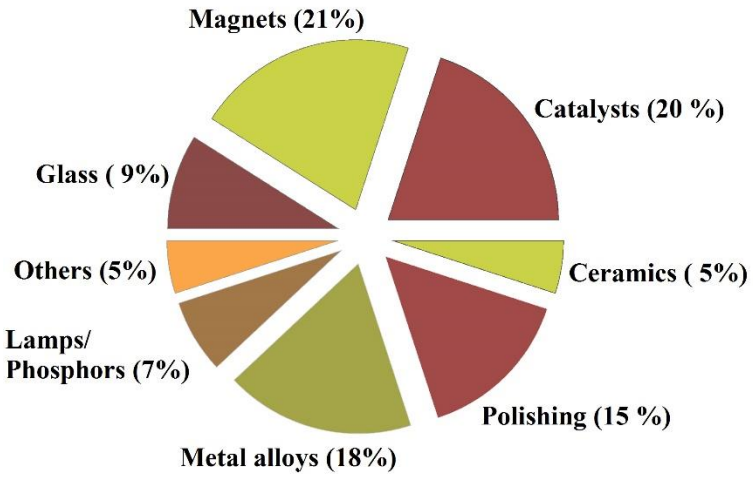

Figure 2. 1 Rare earth element applications

2.3 Deposits and Resources

2.3.1 Deposits and Resources Worldwide

Nowadays, rare earth elements come from the mining industry, but the ongoing research throws a light into the possible production of REEs by its recycling from current applications [51, 52], particularly the permanent magnets with high neodymium content, and waste water treatment.

As this project deals with the processing of an ore from a mineral deposit, the core of this review will focus on the mineral resources and processing.

Rare earth elements are found in more than 200 minerals that contain a variety of REEs with a concentration of at least 0.01 wt.%, but they are found in deposits from which the extraction is very difficult [47, 53]. Despite that many minerals containing REEs, most of the world's rare earth are estimated to be found in three of them, bastnäsite, monazite and xenotime; making these three a preference for the rare earth extraction. Other minerals with potential for extraction of REEs are apatite, perovskite and gadolinite (Table 2. 1) [1, 19, 20, 42, 53].

Even if rare earths are found in many locations and types of mineral deposits, not all of them are viable for exploration and/or extraction due to their low REE grade that may cause technical, environmental or economical issues [19, 20]. Most of the viable rare earth reserves and resources

are located in China, United States, Canada, Australia, India, Russia and South Africa; nonetheless, deposits with lower rare earth concentration can be found worldwide [1, 49]. The current status on world rare earths reserves are published every year by the U.S. Geological Survey [38]. Figure 2. 2 represents the amount of rare earth element and its average grade in some of the deposits.

As it was mentioned in Section 2.2, China controlling most of the REEs market is not only due to the high technological advancement they have in the processing, but also because most of their deposits have a relatively high concentration of REEs, i.e. usually above 3 wt.% [19, 54-56]. Compared to China, most of the deposits worldwide contain more resources, but have less concentrated deposit, making their extraction more difficult (Figure 2. 2).

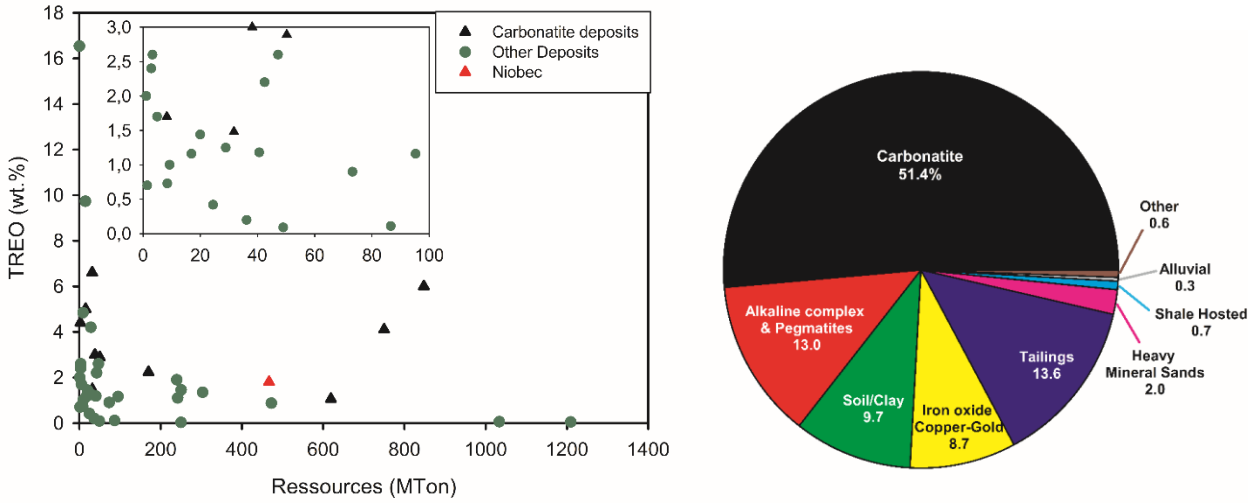

Figure 2. 2 REE deposits: left- Grade and tonnage of rare earth deposits; right- Deposit type distribution [19, 54-56]

Besides grade and resource, it is important to differentiate the deposits in groups based on the associated gangue minerals, and the majority of deposits are known to be associated to carbonatite minerals (50%), e.g. calcite or dolomite [57].

Every year, the United States Geological Survey provide a report regarding production and reserves of rare earth metals in the world [35-38].

2.3.2 Niobec Deposit

Canada is nowadays one of the countries holding main resources of REEs; and despite its potential to become a world leader in the rare earth production, it is still not a major producer (Table 2. 2) [1, 37, 49, 58]. So, driven by the RREs market price peak generated by China's quotas in 2010 [28], Canada rare earth companies, and more recently the government, invested in a new research and development plan for REE production, and by 2015, nineteen projects from the approximately fifty that started around the world were domestic. Four of them in the Province of Quebec [58, 59]. Most of these projects were presented by Hatch, G. P. in 2015 [59].

From those projects, Quest Rare Minerals Ltd.'s Strange Lake, Avalon's Nechalacho and IAMGOLD's Niobec deposit (see Section 2.3.2), may represent one of the major REE deposits after Bayan Obo in China [19, 54-56].

Niobec is one of the main Canadian rare earth deposits with 466.8 million tons of REEs, with an average grade of 1.64 wt.% TREO (Total Rare Earth Oxide). The mine is in Saguenay, Quebec, and drilling reconnaissance was launched by Iamgold Corporation back in 2012. Niobec is a carbonatite deposit type, containing mostly light REEs (98.1 wt.% of TREO) in the form of bastnäsite and monazite. These two REE minerals are found with a similar mass ratio, while most of the gangue is in the form of ankerite, calcite and dolomite [54]. More specifics regarding this deposit can be found in the report elaborated by Grenier and Tremblay in 2013 [54].

2.4 Rare Earth Processing

Processing rare earth elements from the mine to the final product is a process with a complicated array of unit operations that differ between deposits. First, the ore extracted from the mine is reduced in size by crushing and grinding to facilitate the transport and the downstream treatment. Then, the separation process can be divided in three main steps, physical beneficiation, REEs extraction and individual separation of REEs [1, 42]. Figure 2. 3 represents the main steps of the overall process.

Since this project deals with the thermal cracking of a raw rare earth bearing mineral, the literature review will focus on the physical beneficiation and extraction steps.

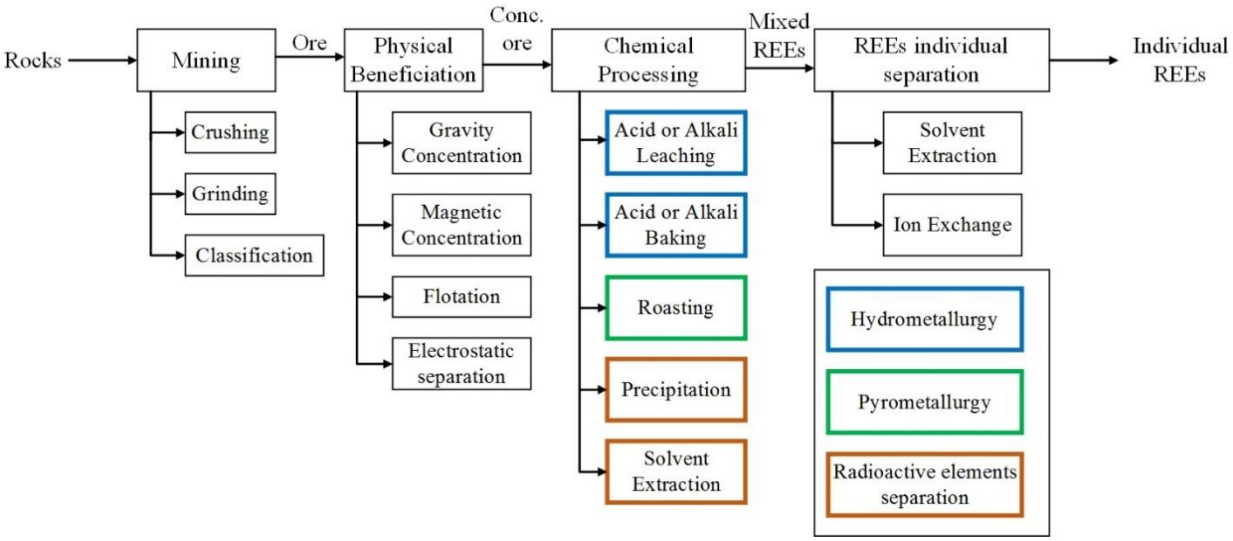

Figure 2. 3 General rare earth extraction process [1]

2.4.1 Physical Beneficiation

Physical beneficiation is a generic name describing the separation of minerals of interest from its gangue based on the physical properties, i.e. magnetic, gravity, electrostatic and flotation, of the minerals. The objective is thus to increase the grade of REEs by the liberation of the rare earth minerals from the host ore [1, 3, 23]. The process is affected among other factors by the geology, particle size and mineral composition of the ore, that define a challenge requiring a complicated array of multiple separation techniques in series [1, 3, 42, 60, 61]. The process may become even more difficult if the gangue minerals have close physical properties as the rare earth minerals, e.g. Bayan Obo in China [62, 63]. Gupta 2004 and Jordens et al 2013 presented some combinations of physical beneficiation techniques already implemented in REE industrial plants [1, 3].

2.4.1.1 Gravity separation

In rare earth extraction and mineral processing, gravity separation is one of the most used techniques. It is, as its name indicates, based on the specific gravity of the minerals and is performed in centrifugal concentrators. In a rare earth deposit, rare earth minerals are often heavier (specific gravity 4 to 7), e.g. bastnäsite 4-5.2 specific gravity, than gangue minerals (specific

gravity 2.5 to 4) [1, 3, 64]. In this kind of processes, the particle size is considered as design factor for the equipment, since bigger particles tend to have the mineral of interest encapsulated by gangue mineral and thus the efficiency is lowered [65].

2.4.1.2 Magnetic separation

Magnetic separation focuses on the gangue separation based the magneticity of the minerals. As a matter of fact, minerals can be divided into three categories, ferromagnetic, paramagnetic and diamagnetic, the two first being magnetic. On that regard, REE minerals tend to be paramagnetic, while some of the associated gangue may be ferromagnetic, e.g. magnetite, or diamagnetic, e.g. zircon [1, 3].

2.4.1.3 Electrostatic separation

The electrostatic separation is based on conductivity or electrostatic charge difference of minerals; e.g. xenotime (non-conductive) and ilmenite (conductive). This technique is an alternative to conventional techniques since it can separate minerals with similar gravity or magnetic properties [3, 66]. However, the amount of energy required by this technique to be effective, i.e. works on dried samples when most of operations are wet, hinders its use in industry [65].

2.4.1.4 Froth flotation

Froth flotation is one of the most conventional physical beneficiation techniques used in the rare earth industry. It exploits the hydrophilicity and hydrophobicity of minerals for their proper separation, and relative wettability of the minerals of interest. On this regard, REE minerals tend to be hydrophobic, while gangue minerals are hydrophilic. REE minerals' property makes them be entrained in a froth to the surface or top of the flotation cell by air bubbles while leaving the gangue in the liquid falls to the bottom of the cell. In order to enhance the separation, some chemical agents or surfactants are often added to the ore. Flotation conditions and surfactant depend on the properties of the minerals (REE and gangue) and works with small particle size. Its efficiency increases when minerals are liberated [1, 3, 23].

Froth flotation was installed in Mountain Pass (before closure) and is ongoing in Bayan Obo, two of the largest REE deposits, both with bastnäsite as characteristic mineral. Focusing on Bayan Obo, prior to flotation, most of the ore is grinded to the mineral liberation size (<74 μm). Flotation

takes place in two steps with few cells in cascade for each step. First iron and silicate gangues are eliminated, and then separation of REE at the top of the cell from the rest of gangue. By froth flotation, an average 45 wt.% rare earth oxide concentration is obtained, while 61 wt.% of REE is recovered. More specifics regarding this process may be found in literature [1, 3, 67].

On a similar trend as in Bayan Obo, it has been reported that bastnäsite recovery increased with temperature. Nonetheless, at ambient temperature, approximately 55% of bastnäsite was recovered when producing a 15 wt.% concentrate of REOs. Bastnäsite recovery was even lower (5-10%) when a higher REO concentration was reached (approximately 40 wt.%) [3].

2.4.2 Rare Earth Extraction – Hydrometallurgy

Rare earth elements require further purification to reach a marketable value. This step corresponds to the rare earth extraction step (Figure 2. 4) and separates impurities that could not be separated by the difference of physical properties of the minerals. The main impurities found with the concentrated ore are not only undesirable, e.g. iron, but can also be hazardous elements, e.g. thorium and uranium [1, 64, 65, 68-70].

The extraction is performed by pyro- or hydrometallurgy. The latter is often preferred due to a lower energy consumption. Hydrometallurgy involves the chemical modification of the rare earth concentrate mineral by attacking it with an aqueous acid or alkali conditions. The aqueous reagent is used to produce a soluble REE salt to rend them more treatable [1, 68].

Hydrometallurgy can be divided in two routes, acid or alkali. Independently of the reagent, the process initially requires severe conditions, i.e. high temperature (200 to 300 ºC) and high reagent dosage (1 to 4), to ensure the production of the cracking of the mineral and the production of the salt [1, 68, 69, 71-75]. Then, the washed aqueous solution may undergo neutralization to selectively precipitate the gangue or the rare earths, before it goes through a final purification. Figure 2. 4 summarizes the main alkali and acid extraction processes.

The acid route is made with strong acids that can dissolve the rare earth elements. On that regard, sulfuric acid is the most extensively used reagent and the oldest practiced technique on rare earth processing [1, 65, 76]. Compared to other acids, sulfuric acid proved to be more effective dissolving phosphate minerals, e.g. monazite [1, 23, 68, 69, 76-82] or xenotime [73, 75, 76, 79,

83-87]. When a similar acid baking process was applied on bastnäsite, the production of a hazardous gas (HF) was detected (Reaction 2.1) [74, 88, 89]. Some of the solutions were to do hydrochloric acid treatment instead of sulfuric or to go through roasting or calcination first as a solution to deactivate the fluorine [89]. Since some techniques exist to deal with the hydrofluoric acid, this method is already applied in industry, e.g. Bayan Obo.

$$2REFCO_3 + 3H_2SO_4 \rightarrow RE_2(SO_4)_3 + 2HF(\uparrow) + 2H_2O(\uparrow) + 2CO_2(\uparrow) \quad (2.1)$$

As presented in Table 2. 1, REE extraction is also performed from minerals other than bastnäsite, monazite and xenotime, where their concentration is lower. Depending on the mineral, the acid to ore ratio varies, but REE extraction are often performed at milder acid leaching condition going from ambient to 70 ºC. For instance, REE extraction from red mud (waste of the bauxite Bayer process) was achieved with hydrochloric and nitric acid [90-93]; while for other phosphate rocks, e.g. apatite, nitric acid proved to be effective [68, 94, 95].

Despite being less applied, some alkali treatment such as baking, or leaching can also extract REE through the production of an alkali cake containing the REE along with the impurities [1, 68, 69, 73, 80, 82, 83, 87, 88, 96-108]. The cake is then leached by an acid reagent, e.g. HCl, to produce a soluble REE compound, e.g. RECl3 [73, 83, 97]. Compared to acid techniques, alkali require more steps for the extraction, need longer reaction times and are less efficient [73]. They are nonetheless useful for fluorine deactivation as they may produce an inorganic compound such as CaF_2 [23, 108]. Therefore, fluorine deactivation could be used as a criterion for the selection of an appropriate treatment for the chemical processing of rare earth concentrate.

Independently of the hydrometallurgical technique used in rare earth extraction, most of studies have reported that in the hole step of REE extraction, a REE recovery of 90 wt.% can be achieved [73, 83, 106]. Nonetheless, hydrometallurgy's efficiency depends on the reactor type [68, 71, 109, 110], e.g. rotary kiln or fluidized bed, and the ore's morphology [1], i.e. particle size or porosity. These factors might ensure a good reagent and ore contact. In the case of alkali treatments, the reactor type is of extreme importance since the alkali cake is produced in the outer layer of the particles and needs to be broken to improve the reagent diffusion through the product layer and reduce the residence time [96, 97]. For instance, Abd El Rehim 2002 presented the ball mill autoclave reactor [96].

To help solve some of the issues of the hydrometallurgy step, some authors presented high temperature treatments as an alternative solution. On that regard, these treatments would avoid some of the environmental issues raised by acid baking technique, i.e. hazardous gases production (HF, sulfur dioxide, etc.).

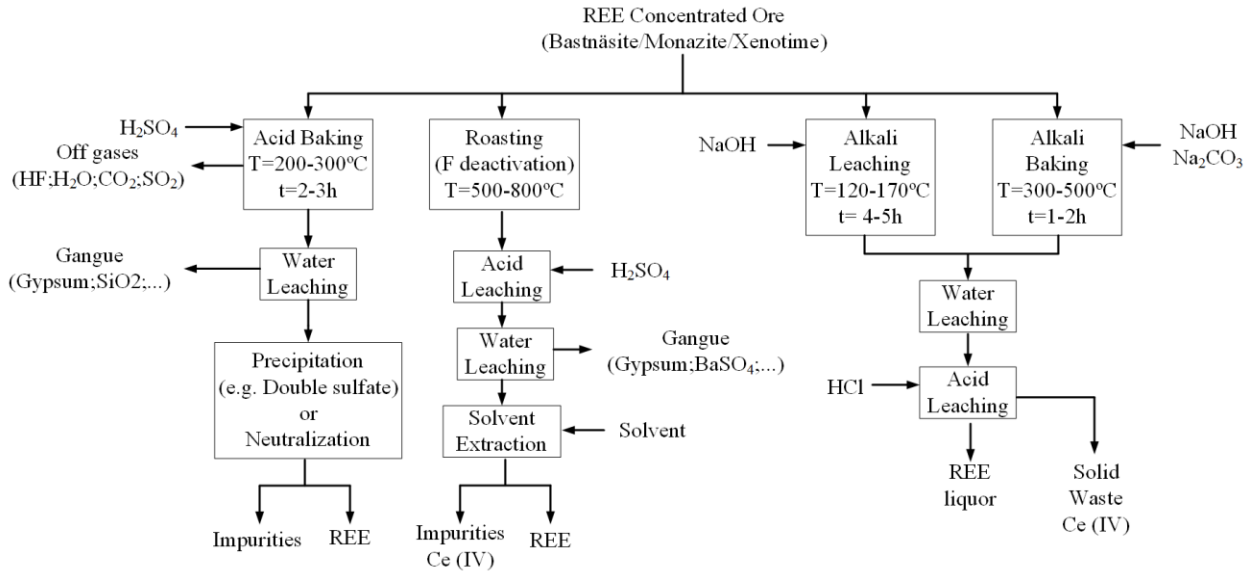

Figure 2. 4 Simplified hydrometallurgical extraction of rare earth: left- Acid [1, 73, 75] right- Alkali [73, 97]

2.5 High temperature processes in rare earth industry

High temperature processes, often described as pyrometallurgy, are an old-fashioned technique and known technology that has long been used in the mining industry to produce metal oxides, e.g. lime from calcium carbonate or calcite [11, 112-115]. Its application on the rare earth industry aims to produce a mixture or pure rare earth oxides. Yet, its ending target depends on the step of the process where it is applied. This state of the art of high temperature process in the rare earth industry will focus on its use on minerals.

Processes involving high temperature treatment have been used in rare earth industry and focus mainly on the concentrates of REE bearing minerals [10, 11, 116, 117]. As most of the rare earth industry these process have been developed for bastnäsite and monazite [1, 118]. High temperature processes can be divided in two main groups, calcination and chlorination [1].

2.5.1 Chlorination

Chlorination treatment is a high temperature direct chlorination of minerals, also known as Goldschmidt process, that aims for the extraction of rare earth elements in their chloride form [1, 119]. In it, REE minerals such as bastnäsite, monazite, xenotime or cerite react with coal and chlorine at a temperature between 1000 and 1200 ºC and form a melted metal chloride (Reaction 2.2) that is recovered at the bottom of the furnace [1, 119, 120]. Fluorine deactivation from bastnäsite can be achieved with silicon tetrachloride (Reaction 2.3) [23]. At such temperatures some gangue is recovered with the REE, e.g. calcium or barium chloride (e.g. Reaction 2.4), while other such as the iron chloride are recovered with the off-gases due to their lower boiling point (Reaction 2.5) [1, 23].

$$REPO_4 + 3C + 3Cl_2 \rightarrow RECl_3 + POCl_3 \uparrow + 3CO \uparrow \quad (2.2)$$

$$REOF + C + Cl_2 + \frac{1}{4}SiCl_4 \rightarrow RECl_3 + \frac{1}{4}SiF_4 \uparrow + CO \uparrow \quad (2.3)$$

$$BaSO_4 + C + Cl_2 \rightarrow BaCl_2 + CO_2 \uparrow + SO_2 \uparrow \quad (2.4)$$

$$\frac{1}{3}Fe_2O_3 + \frac{1}{2}C + Cl_2 \rightarrow \frac{2}{3}FeCl_3 + \frac{1}{2}CO_2 \uparrow \quad (2.5)$$

2.5.2 Calcination of rare earth minerals

Calcination studies of rare earth bearing minerals have focused on the three main REE minerals, i.e. bastnäsite, monazite and xenotime, and differed between the carbonatite and phosphate type minerals [1].

Several studies have been developed to thermally decompose (500-900 ºC) bastnäsite with the aim of producing a highly concentrated rare earth oxide and deactivating the fluorine of the mineral [1, 118]. In a calcination performed on a bastnäsite from Mianning in Siehuan, Xiang et al. 1994 described bastnäsites decomposition to take place in two steps with the formation of a rare earth oxyfluoride first and then the decomposition of this form to produce rare earth oxides and fluorides [12]. During the calcination under air, cerium oxidized from cerium (III) to cerium (IV), facilitating its dissolution in the subsequent acid leaching [1, 89, 121, 122].

As opposed to bastnäsite whose carbonate phase is easily decomposed at high temperature, phosphate minerals, i.e. monazite and xenotime, have a decomposition temperature above 2000ºC [11, 14]. In order to reduce the elevated decomposition temperature of monazite, the addition of an agent was tested [13, 117, 123-125]. At first, Hikichi et al 1980 proposed to reduce the calcination temperature by solid reaction state of rare earth phosphates with an oxide. While the addition of alumina was to reduce REE phosphate's melting temperature, the addition of calcium oxide was able, through solid-solid reaction, to decompose it at approximately 700 ºC to produce rare oxide and calcium phosphate (Reaction 2.6) [13]. Later, Merritt 1990 proposed to perform monazite's calcination under a reductive atmosphere [124, 125]. Since the first tests with gaseous and calcium halide reactants were performed [124, 125], many strategies and reductive agents have been tested. When mixed with charred coal, monazite's decomposition took place at around 1400 ºC achieving a 98% dephosphorization of the mineral [117].

$$2REPO_4 + 3CaO \rightarrow Ca_3(PO_4)_2 + RE_2O_3 \quad (2.6)$$

As monazite and bastnäsite are often found together in same deposits, e.g. Bayan Obo or Niobec, most of recent studies have focused on the calcination of a concentrate containing both REE minerals. To decompose such mixture, researchers used alkali agents to enhance fluorine deactivation and at the same time reduce monazite's temperature decomposition. Even though the

addition calcium oxide was able to solve both matters [10, 13, 126], the addition of alkali reagents or a reducing atmosphere was able to increase monazite's dephosphorization at same conditions as the calcium oxide[9, 10, 15, 17, 127]. Wu et al 2007 used CaO-NaCl-$NaCl_2$ to calcine a bastnäsite and monazite rare earth concentrate [9, 17]. It was reported that first the calcium oxide from the salt reacted between 425 and 540 ºC with the rare earth oxyfluoride formed during bastnäsite's decomposition to produce calcium fluoride (Reaction 2.7). In a second step, monazite, by reacting with calcium oxide and calcium fluoride at temperatures between 610 and 700 ºC, was decomposed into the rare earth oxide and a calcium phosphate complex (Reaction 2.8) [9, 17].

$$CaO + 2REOF \rightarrow RE_2O_3 + CaF_2 \quad (2.7)$$

$$9CaO + CaF_2 + 6REPO_4 \rightarrow 3RE_2O_3 + 2Ca_5F(PO_4)_3 \quad (2.8)$$

A limit to both high temperature techniques is that their application focused on the concentrated ore, while the treatment of the raw ore remains very limited. Only some calcination studies have been introduced during the low grade rare earth ore treatment, giving as a result a mixture of metal oxides that was further treated to remove the alkali earth metals from the mixture [128]. However, this type of use has not been generalized.

2.6 Modeling

2.6.1 Kinetic modeling

Kinetic deals with the measurement and parameterization of process rates with three variables related to experimental conditions, pressure or partial pressure of gases, temperature and conversion (Equation 2.1). With the experimental conditions, the kinetic parameters, i.e. reaction model, activation energy and pre-exponential factor, can be estimated. It is thus possible to predict the reaction rate and by extension of its definition, the reactant's consumption or products' formation. In gas-solid reactions at high temperature, as calcination, the pressure dependence of kinetics is often ignored since gas product is removed efficiently, simplifying the kinetics as in equation 2.2 [129].

$$\frac{d\alpha}{dt} = k(T)f(\alpha)h(P) \quad [2.1]$$

$$\frac{d\alpha}{dt} = k_0 exp\left(-\frac{E_a}{R\,T}\right) f(\alpha) \quad [2.2]$$

Where k(T), f(α) and h(P) are the temperature, conversion and pressure dependence parameter respectively. The first term, k(T) is dependent on the pre-exponential factor (k_0), the activation energy (E_a) (J/mol), the universal gas constant (R) (J/(mol K)) and the temperature (T) (K). The term f(α) denotes the reaction model, with α as the conversion defined as the reaction's mass loss.

Various methodologies are available to perform the kinetic study and they can be classified into two groups, free and fitting models [129-133]. The latter involves fitting the experimental data to pre-existing models to obtain the three kinetic parameters, i.e. pre-exponential factor, activation energy and reaction model, at the same time [134, 135]. In this case, the appropriate kinetics are obtained by minimizing the difference between the model and the experimental data by residual sum of squares. On the opposite hand, free model considers the activation energy to be independent of the reaction model, the reaction can thus be approximated to a single kinetic model or the reaction model can be coupled to the reaction rate after estimation of the other two kinetic parameters [129, 135-137]. Each model is related to a particular rate controlling process. To avoid repetitions regarding the existing models, they can be found in Table 5.2 [129, 134, 135].

2.6.2 Mineral calcination - Kinetic modeling

Kinetic studies on the calcination of minerals have previously been performed. Most of them focused on calcite and dolomite minerals. They often described a model in the form of contracting cylinder or sphere. Nonetheless, there is a discrepancy regarding the reaction order and the activation energy caused by the minerals' characteristics (purity, mass or particle size), the operating conditions (heating rate, atmosphere, …) or the modeling technique used in the kinetic study (isothermal vs non-isothermal) [113, 138-141].

An excess of mass in thermogravimetric analyzer increases the external mass transfer on the sample, while the average size of the sample increases the internal diffusion of the gas [132, 140-142]. The mineral's origin or purity is related to a variation in the elemental composition, which can also affect the kinetics of the calcination, e.g. a higher manganese content increases the

activation energy of carbonate's calcination [138]. On that regard, activation energies varying from 131 to 211 kJ/mol were found for calcite's calcination [133].

Therefore, it is important to take these parameters into consideration before performing a kinetic analysis on the calcination of minerals.

Focusing on rare earth minerals, there is still a lack of study on calcination of a rare earth bearing ore or minerals, since as described in Section 2.4, most of R&D focuses on physical beneficiation or hydrometallurgy of these minerals.

Calcination studies aimed mainly at bastnäsite and monazite, two of the main REE concentrated minerals found in most of the deposits. Bastnäsite's calcination was first studied by Xiang et al. 1994, and formed rare earth oxide and fluoride along with CO_2 [12, 143]. The calcination performed on a mineral from Mianning (China) took place at around 400 ºC [12, 143], and the decomposition kinetics followed a reaction order of 1.1, which could be considered as Mampel first order reaction, while the activation energy was approximately 49.3 kJ/mol [12].

On the other hand, monazite is a phosphate mineral that does not decompose at high temperature since its sintering temperature is at approximately 2000 ºC [11, 13, 14]. To reduce the calcination or thermal decomposition temperature (600-800 ºC) of monazite an additive, e.g. charcoal, CaO or a salt, was well mixed with the phosphate REE mineral prior to calcination [9, 13, 15, 17, 117]. Such reaction is known as solid-solid reaction, and as a result needs the contact between the mineral and the additive to take place. Kinetics of monazite decomposition by its reaction with calcium oxide or a mixture of calcium oxide, sodium chloride and calcium chloride described a Ginstling-Brundshtein decomposition model [17]. Xue et al. 2010 described two sets of kinetic parameters depending on the reaction temperature, by which the reaction was the main controlling step at low temperatures (below 700 ºC), whereas diffusion and reaction controlled the decomposition at high temperatures. The activation energy for the reaction of monazite with calcium oxide was 33.8 kJ/mol and was reduced to 19.9 kJ/mol when salts where used in the system [17]. Monazite's reaction with calcium oxide when both are found within a particle in an ore might be possible but has not been studied yet.

Although literature in English language regarding calcination of REE minerals seems to scarce, literature in Chinese language seems to be more developed.

CHAPTER 3 OBJECTIVES AND THESIS STRUCTURE

3.1 Objectives

The main objective of this work is to design a process for the calcination of a rare earth bearing ore for the production and extraction of rare earths oxide. Based on the presented literature review, the calcination study will focus on the fresh or raw rare earth bearing ore.

To accomplish the main objective, this work will be divided in two main parts:

- Investigate the calcination of a rare earth bearing ore:
    - Understand and propose a reaction mechanism for the decomposition of the ore and production of rare earth oxide.
    - Develop a kinetic model for the calcination of the pure minerals that intervene in the decomposition of the REE ore
    - Predict the calcination of the REE ore with a particle size lower than 20 µm by using a kinetic model. This model will be based on the models obtained for the calcination of the pure minerals. The selection of the size will be based on the liberation size of those minerals within the ore.
    - Formulate the effect of the physical properties of the ore for different ranges of particle size on the kinetic model of the decomposition of the rare earth ore.
- Evaluate the calcination of the rare earth bearing ore in a fluidized bed reactor:
    - Investigate the calcination of the rare earth bearing ore in a fluidized bed reactor in order to evaluate the effect of calcination and fluidization on the morphology of the particles.
    - Improve the production of rare earth oxide and the concentration of the rare earth oxide by leaching by assessing the effect of the ore's particle size on the performance of the fluidized bed reactor.
    - Validate the kinetic model from previous specific objectives in a fluidized bed reactor.

3.2 Thesis structure

The scientific findings of this work are presented from Chapter 5 to 8 and consist of three scientific articles (Chapters 5 to 7) and one chapter (Chapter 8).

Chapter 5 is the first paper “Kinetics of Calcination of Natural Carbonate Minerals” submitted to Minerals Engineering and presents the calcination study of carbonate minerals, which is a group of minerals that are easily found in the earth’s crust and especially in rare earth deposits. The main objective of this part is to study the kinetics of decomposition of these minerals that represent more than 70wt.% of the ore from Niobec. It focuses among other minerals in bastnäsite, a rare earth carbonate mineral whose thermal decomposition kinetics lacks studies and is one of the main rare earth bearing minerals with monazite and xenotime.

In Chapter 6, as the second paper “Kinetic Study of Calcination of a Rare Earth Ore” submitted to Journal of Rare Earths, the study of the thermal decomposition mechanism of Niobec’s rare earth bearing ore allows to determine the reaction steps and minerals involved during the calcination. In it, the presence of solid-solid reactions for the decomposition of monazite is discussed. A proper reaction mechanism allows the development of a global kinetic model describing the decomposition of the ore. This model uses the results found in Chapter 5 since it is based on the individual decomposition of the pure minerals composing the ore.

Chapter 7 presents the third article, “Production of Rare Earth Oxides from Raw Ore in Fluidized Bed Reactor” submitted to Journal of Industrial and Engineering Chemistry, is devoted to study the calcination of the rare earth bearing ore in a fluidized bed reactor to produce rare earth oxides. It also involves the study of the selection of an adequate particle size to increase the production of the rare earth oxides by calcination, and its concentration by leaching the gangue or impurities. The morphology evolution of the particles during calcination in the fluidized bed, e.g. porosity or particle size, is also treated in this chapter and will be useful in future works for the reactor modeling.

Chapters 6 and 7 are used in Chapter 8 that presents a simplified fluidized bed model that could represent the experimental results from the fluidized bed calcination presented in Chapter 7. Chapter 6 is used as the kinetics of the ore decomposition is necessary for the reactor modeling in

order to estimate gas production in the reactor. The validation of the model with the results from Chapter 7 could allow in the future the modeling of an industrial scale reactor in which the effects of the fluidization hydrodynamics on the calcination can be studied.

Finally, Chapters 8 and 9 are respectively the general discussion of the results presented in previous chapters and the conclusion and recommendations of this work.

CHAPTER 4 METHODOLOGY AND MATERIALS

4.1 Methodology

4.1.1 Equipment

Calcination of the ore was performed in several reactors, mainly fluidized bed reactors; while the kinetic studies were performed in a thermogravimetric analyzer.

4.1.1.1 Thermogravimetric analyzer (TGA)

TGA is used to study the calcination of minerals and ores. It provides the total mass loss evolution at different heating rates and allows the kinetic study of the pure minerals calcination to be performed. This equipment can be combined with some analytical equipment, e.g. gas chromatography, to analyze the evolved gas.

4.1.1.2 Fluidized bed thermogravimetric analyzer (FBTGA)

As for the TGA, this equipment is used to analyze the thermal treatment of solids, but in this case in a fluidized bed. It can also be combined with other equipment for evolved gas analysis. Compared to TGA, this equipment is a microreactor and treats a few grams instead of a few milligrams. It can solve mass transfer issues that are found in TGA [144].

4.1.1.3 Gas analysis

Gas analysis techniques were coupled to the thermal treatment equipment, i.e. TGA or fluidized bed reactors, to analyze the evolved gases produced during calcination of the pure minerals and the ore. On that regard, two equipment were used, Fourier Transform Infrared Spectroscopy (FTIR) and Gas Chromatography (GC). The FTIR was a MultiGasTM 2030 Series FTIR from MKS, while the GC was a CP-4900 Varian GC. FTIR was used to measure CO_2, CO, SO_2, SO_3 and H_2O gases, while GC was used for N_2, O_2 and CO_2 measurements.

4.1.2 Characterization

The selection of an adequate characterization technique in REE processing is important, since these elements are difficult to detect at low concentration as it is the case in the REE ore from Niobec.

This difficulty lays on the heterogeneity of the ore. Most of the characterization techniques used in this work were for solid samples.

4.1.2.1 X-Ray Diffraction (XRD)

X-Ray diffraction analysis (XRD) was used in this work to qualitatively analyze the mineral composition of the ore before, during and after calcination. The XRD equipment was a Panalytical (X'Pert Pro MP) with a Copper anode and a PIXcel1D detector found at Polytechnique Montreal (CM^2 facilities).

4.1.2.2 XRK

XRK is the same technique as XRD, but the sample is inside a heating chamber. In it, diffractograms can be taken at a certain temperature allowing the study of the decomposition of a sample. Although it is mainly for qualitative analysis, as in XRD, some quantification of the composition analysis can be performed by Rietveld method. In this work, an XRK900 from Anton Paar was used.

4.1.2.3 QEMSCAN

QEMSCAN (Quantitative Evaluation of Materials by Scanning Electron Microscopy) is an imagery technique that uses a combination of SEM-EDS (Scanning Electron Microscopy-Energy Dispersive X-ray Spectroscopy) and software to analyze the mineral composition of a sample. It also allows for heterogeneous samples to understand the mineral grain and liberation size, and the mineral association within a particle. QEMSCAN was performed at XPS Expert Solutions.

4.1.2.4 LECO

LECO is a technique that measures carbon and sulfur content in solid samples. It was used to measure both elements in the ore before and after calcination to track the conversion of the calcination along the reaction and to ensure the complete conversion of the sample by the elimination of CO_2.

4.1.2.5 Neutron Activation Analysis (NAA)

NAA is a nuclear reactor found at Polytechnique Montreal that by irradiating the sample can quantitatively determine elemental concentration. The quantification is done by measuring the gamma rays emitted by the irradiated elements.

4.1.2.6 Ion Coupled Plasma Mass Spectroscopy (ICP-MS)

ICP-MS was performed at University of Montreal (UdeM) with a Perkin-Elmer NexION 300 equipment. This technique was used for elemental analysis in aqueous samples obtained during leaching.

4.2 Material

In this work two kind of materials were used a feed, the ore given by the industrial partner, Niobec, and pure minerals collected from a private collector.

4.2.1 Niobec ore

The ore used in this project is a mixture of minerals and came from a deposit at Saguenay, East of Quebec, Canada. It was given by Niobec. Most of the ore was composed of carbonate minerals (78.9 wt.%), e.g. calcite, dolomite and bastnäsite.

Regarding the calcination of the ore in a fluidized bed, the ore belongs to Group B Geldart classification (average density of 3110 $kg \cdot m^{-3}$) and its minimum fluidization velocity is 0.82 cm/s. The characteristics of these particles are presented in next chapters.

4.2.2 Minerals

Minerals used in this work came from different locations. They were grinded from hard stones to powder with a particle size below 300 μm and were tested with XRD to evaluate their purity. More information regarding these materials can be found in Chapters 5 and 6.

CHAPTER 5 ARTICLE 1: KINETICS OF CALCINATION OF NATURAL CARBONATE MINERALS

Adrián Carrillo García, Mohammad Latifi and Jamal Chaouki*

Process Development Advanced Research Lab (PEARL), Chemical Engineering Department, Polytechnique de Montreal, QC H3T 1J4, Canada

*Corresponding author: jamal.chaouki@polymtl.ca; C.P. 6079, Succ. Centre-ville, Montreal, Québec, Canada, H3C 3A7

(Minerals Engineering, submission date: July 12th 2019)

ABSTRACT

The authors have developed a process for the direct production of the rare earth elements oxides (REO) through the calcination of a raw ore that contains carbonate minerals, such as bastnaesite (a known REE bearing carbonatite) and gangues (e.g., calcite, dolomite, siderite, and ankerite). Due to the complexity of the ore, an elaborated kinetic study was required to gain an insightful understanding of the contribution of each mineral to the overall reaction kinetics. Thus, calcination kinetics of individual carbonates was investigated by thermogravimetric analysis, and subsequently new as well as modified kinetic models were developed.

The comparison of kinetic parameters and decomposition conditions of bastnaesite and gangue minerals revealed that the calcination of bastnaesite happens at much lower temperatures than the gangues. Bastnaesite decomposition starts at 400 ºC while gangue minerals decompose above 500ºC. So, the selectivity of REO production should be enhanced by adjusting the reactor residence time so that the majority of the gangue remains unreacted, thus reducing the complexity of the downstream hydrometallurgical process.

KEYWORDS:

Rare earth elements, bastnaesite, carbonate minerals, calcination, kinetic modeling

5.1 Introduction

Rare earth elements (REE) are strategic metals used in a wide range of applications among which are the green technologies and electronic devices. Some applications are phosphors for energy efficient lightning, permanent magnets in wind turbines and electric vehicles, catalysts, smartphones, and computers [1, 2].

These elements are naturally found on earth in the form of minerals that are mainly in the form of carbonates or phosphates [2]. The three rare earth elements bearing minerals from which REE extraction is viable are bastnaesite, monazite and xenotime. Bastnaesite is a rare earth fluorocarbonate mineral ($(REE)FCO_3$) while monazite and xenotime are phosphate minerals ($(REE)ThPO_4$). Monazite and bastnaesite bear mainly light REE while xenotime does heavy REE. Phosphate REE bearing minerals contain some inclusions of radioactive elements, such as thorium and uranium [2].

In most of the rare earth deposits, REE bearing minerals are adjacent to carbonatite or alkaline gangues [2-5]. The carbonatite-based gangues are igneous minerals that, when adjacent to rare earth bearing minerals, usually represent more than 50 wt% mineral concentration of a rare earth deposit. The most outstanding ones are calcite ($CaCO_3$), magnesite ($MgCO_3$), dolomite ($CaMg(CO_3)_2$), and ankerite ($CaFe^{2+}(CO_3)_2$) [6, 7].

The presence of gangue minerals associated with rare earth bearing minerals renders the extraction of rare earth elements from deposits a complex process that frequently includes a thermal decomposition process, such as baking and calcination, i.e., thermal cracking under air [2, 8].

A high-grade REO production process usually includes an upstream physical beneficiation step where a rare earth concentrate is produced from a raw ore. Downstream of the physical beneficiation, the concentrate would undergo a complex thermochemical process where there is a calcination stage either at an intermediary step or the end of the process (Figure 5.1) [2, 9-12].

Therefore, the study of the thermal behavior of REE bearing minerals and associated gangues in a calcination reactor is necessary to discern the operating conditions and to develop kinetic models for scaleup purposes.

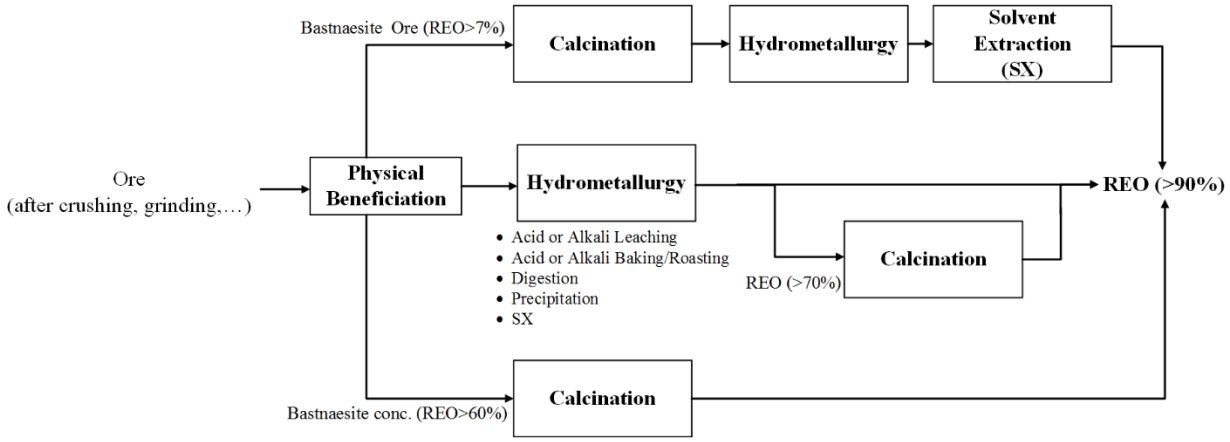

Figure 5.1 Simplified REE ore processing flowsheet. (Adapted from [2])

The authors have developed a new process where REO is directly produced from raw ore in a calcination reactor. REE bearing minerals of the ore are bastnaesite and monazite, each with a mass fraction less than 2 wt% that are associated with gangues of more than 77 wt% of which there are carbonatites, such as dolomite, calcite, ankerite, and siderite.

Thus, as part of the overall calcination reactions, calcination kinetics of carbonate minerals with non-isothermal computational methods, such as isoconversional, free model, and model fitting were investigated. This research was particularly important for ankerite and bastnäsite due to scarcity that exists in literature regarding the calcination kinetic parameters of these minerals [13-16].

Due to the complexity of the ore, the kinetics of calcination of each mineral was individually investigated by thermogravimetric analysis (TGA), and consequently, a kinetic model verified by experimental data was proposed for each mineral.

5.2 Experimental and Kinetic Computational Methods

5.2.1 Material/Minerals

The minerals used in this research came from various private collectors, making their country of origin different for each of them (Table 5.1). All minerals were received in the form of hard stones,

except for the bastnaesite, which was received as a powder. The hard stones were crushed in a shatterbox from Baldor for approximately 4 to 5 min. Their particle size was then analyzed with the Malvern Master Sizer MS3000. The variability in the particle size could be caused by the physical properties of each mineral.

Table 5.1 Carbonate mineral characteristics

Mineral	**Composition from NAA (wt.%)**						d_p **range (μm)**	$d_{p,32}$ **(μm)**	**Source**
	Ca	**Mg**	**Mn**	**Fe**	**TRE[b]**	**C**			
Calcite $CaCO_3$	41.8	<0.2	<0.1	-	-	12.0	200-500	349.6	Morocco
Dolomite $(Mg,Ca)CO_3$	21.2	10.6	0.3	4.6	-	12.6	105-354	168.6	Teruel, Spain (Ojos Negros)
Siderite $FeCO_3$	5.9	1.3	3.6	36.2	-	9.6	53-210	130.4	Vizcaya, Spain
Ankerite $Ca(Mg,Fe)(CO_3)_2$	20.6	3.9	0.5	16.5	-	11.5	200-500	401.2	Vizcaya, Spain
Bastnaesite $REFCO_3$[a]	2.8	2.4	<0.1	-	61.2	5.5	125-354	249.9	California, USA (Mountain Pass)

[a] RE=Rare earth elements; [b] TRE= Total rare earth elements

5.2.2 Experimental and characterization equipment

The kinetic evaluation of the calcination of each mineral was carried out with a thermogravimetric analyzer (TGA) under an air atmosphere. The TGA used for such experiments was a TGA Q5000 of TA Instruments.

To study diverse methods of kinetic modeling, several attempts at different heating rates were performed. To avoid the effect of external mass transfer on the analysis, a sample mass between 10 and 15 mg was used. The balance chamber was purged with a 40 ml/min nitrogen flow while a similar flow of air was maintained in the reaction chamber for each experiment. The high flow rate and low sample mass of the experiments was necessary for a fast purge of the produced gases and to limit the reverse reaction of CO_2 produced during the calcination of carbonates [17-20].

In some cases, due to the particularity of some minerals (e.g., Ankerite and Bastnaesite) with a multi-step decomposition reaction, an X-Ray Diffraction (XRD) analysis with a reactor chamber (XRK) was performed at Sherbrooke University to distinguish the reaction steps of each mineral. The XRD was from the Panalytical company (X'Pert Pro MP) with a Copper anode and a PIXcel1D detector. The XRK (XRK900 from Anton Paar) was a reaction chamber installed in the XRD to study the change of the crystalline structure of a product as a function of temperature.

With the thermogravimetric analysis performed on the minerals of study, it was possible to establish the kinetic triplet of each mineral using diverse kinetic methods.

5.2.3 Kinetic computation methodology

Kinetic study was employed to estimate the rate of calcination reactions which is a function of temperature, activation energy, pre-exponential factor, and reaction model with a general presentation in Eq. 5.1 [16].

$$\frac{d\alpha}{dt} = k_0^* \, exp\left(-\frac{E_a}{R}\left(\frac{1}{T}-\frac{1}{T_r}\right)\right) f(\alpha) \qquad [5.1]$$

Where $k_0^* = k_0 \, exp(-E_a/(RT_r))$, in which k_0 is the pre-exponential factor (s^{-1}), E_a is the activation energy (J/mol), R is the universal gas constant (J/mol K), T is the actual temperature of the sample (K), T_r is a reference temperature (K), and f(α) is the reaction model. The α is a representative of the conversion of the reaction and can be defined as the mass loss from the calcination reaction (Eq. 5.2).

$$\alpha = \frac{m_0 - m_i}{m_0 - m_\infty} \qquad [5.2]$$

Non-isothermal TGA tests, i.e., with heating rates from 2 to 20 ºC/min, were applied to each mineral followed by kinetic computational techniques, such as a model fitting, free-model or isoconversional technique. Prior to performing the computational technique, a heat transfer model was applied on the TGA results to correct the temperature measured by the thermocouple, as per Section Appendix A. These techniques have been discussed in the literature, so their development background is not the focus of this research [13, 14, 16, 21, 22].

5.2.3.1 Model Fitting Technique

Model fitting is a well-known technique in heterogenous kinetic studies to relate the reaction rate to a particular model (f(α) in Eq. 5.1) that describes the mechanism of the overall rate, i.e., the dependence of conversion on the reaction rate and the rate of gas diffusion (internal or external). Several models were developed to evaluate heterogenous systems; the main ones, used in this research, are represented in Table 5.2. Khawam and Flanagan have discussed their fundamental backgrounds[23].

The model fitting was employed for each of the applied heating rates to evaluate the consistency of the activation energy and see if the heating rate might influence the reaction mechanism.

For a given heating rate, Eq. 5.1 was linearized. The non-linear statistical analysis was then taken. This analysis is based on the least squares method, which consists of the calculation of the residual sum of squares (RSS) of the reaction model as presented in Eq. 5.3.

$$RSS = \min of \ \sum \left(\left(\frac{d\alpha}{dt} \right)_{exp} - \left(\frac{d\alpha}{dt} \right)_{calc} \right)^2 \quad [5.3]$$

Where $(d\alpha/dt)_{exp}$and $(d\alpha/dt)_{calc}$ represent the reaction rate obtained from the experimental data and the reaction model, respectively.

The model that yielded the lowest error between experimental and calculated data was considered as the model candidate. As supplemental validation, an overview of additional valid kinetic parameters of the activation energy and pre-exponential factor were presented in the form of a contour map (see Section Appendix C)[24].

Subsequently, the pre-exponential factor and the activation energy were estimated.

Model fitting was taken using two approaches, integral and differential. The integral model fitting approach (IMF) employs g(α) as in Eq. 5.4.

$$g(\alpha) = \int \frac{1}{f(\alpha)} \cdot d\alpha = \frac{k_0^*}{\beta} \cdot \int exp\left(-\frac{E_a}{R}\left(\frac{1}{T} - \frac{1}{T_r} \right) \right) \cdot dT \quad [5.4]$$

Where β is the heating rate in (ºC/min or s).

The differential model fitting approach (DMF) employed Eq. 5.5 to estimate the kinetic parameters associated with the selected reaction model.

$$ln\left(\frac{d\alpha/dt}{f(\alpha)}\right) = \ln(k_0^*) - \frac{E_a}{R}\left(\frac{1}{T} - \frac{1}{T_r}\right) \quad [5.5]$$

Table 5.2 Reaction models used to describe solid state reactions [16, 23].

Reaction Model	f(α)	g(α)
Power Law	$2\alpha^{1/2}$	$\alpha^{1/2}$
	$3\alpha^{2/3}$	$\alpha^{1/3}$
	$4\alpha^{3/4}$	$\alpha^{1/4}$
	$2/3\alpha^{-1/2}$	$\alpha^{3/2}$
One Dimensional Diffusion	$1/2\alpha^{-1}$	α^2
Two Dimensional Diffusion	$[-ln(1-\alpha)]^{-1}$	$(1-\alpha)ln(1-\alpha)+\alpha$
Three Dimensional Diffusion	$3/2(1-\alpha)^{2/3}\left[1-(1-\alpha)^{1/3}\right]^{-1}$	$\left[1-(1-\alpha)^{1/3}\right]^2$
Mampel (first order)	$1-\alpha$	$-ln(1-\alpha)$
Contracting Cylinder	$2(1-\alpha)^{1/2}$	$1-(1-\alpha)^{1/2}$
Contracting Sphere	$3(1-\alpha)^{2/3}$	$1-(1-\alpha)^{1/3}$
Avrami-Erofeev	$2(1-\alpha)[-ln(1-\alpha)]^{1/2}$	$[-ln(1-\alpha)]^{1/2}$
	$3(1-\alpha)[-ln(1-\alpha)]^{2/3}$	$[-ln(1-\alpha)]^{1/3}$
	$4(1-\alpha)[-ln(1-\alpha)]^{3/4}$	$[-ln(1-\alpha)]^{1/4}$

5.2.3.2 Model-Free Technique

The model-free (FM) technique studies the apparent activation energy without having any knowledge about the reaction model and the pre-exponential factor. The evaluation is done by the linearization of Eq. 5.1, which would result in Eq. 5.6. Thus, the apparent activation energy would be estimated from the slope of the plot of $ln(d\alpha/dt)$ versus $(1/T - 1/T_r)$ [16].

$$ln\left(\frac{d\alpha}{dt}\right) = ln(k_0^* \cdot f(\alpha)) - \frac{E_a}{R}\left(\frac{1}{T} - \frac{1}{T_r}\right) \quad [5.6]$$

This technique assumes that the rate of reaction is independent of the reaction mechanism. In other words, the activation energy is the only parameter that is obtained from the free-model technique.

Therefore, to obtain the two other kinetic parameters, i.e., A and n, it has to be coupled with a reaction model from Table 5.2. The pre-exponential factor also can be estimated by the "compensation effect"[16].

5.2.3.3 Friedman Differential Isoconversional technique

The isoconversional technique can also be described as a model-free method. It assumes that the reaction rate is a function of the heating rate at a given conversion. So, by taking the heating rate as $\beta = dT/dt$, Eq. 5.6 can be re-written as Eq. 5.7 for an arbitrary conversion of α_i associated with a heating rate of β_i. This methodology is called Friedman's isoconversional method (ICF) [16].

$$ln\left(\beta_i \cdot \left(\frac{d\alpha}{dT}\right)_{\alpha,i}\right) = ln(f(\alpha_i) \cdot k_0) - \frac{E_{a,\alpha}}{R \cdot T_{\alpha,i}} \quad [5.7]$$

Since it must be independent of the heating rate, the activation energy ($E_{a,\alpha}$) corresponding to the arbitrary conversion can be obtained from the slope of the plot of $ln(\beta_i \cdot (d\alpha/dT)_{\alpha,i})$ vs $1/T_{\alpha,i}$ where $T_{\alpha,i}$ is the temperature and $(d\alpha/dT)_{\alpha,i}$is the reaction rate based on the heating rate β_i. In this research, four heating rates of 2, 5, 10 and 20 ºC/min were applied.

Compared to other techniques, Friedman's isoconversional method can be a tool to identify a change in a reaction system. That is, a change of the apparent activation energy at a given conversion can indicate that the decomposition reaction comprises a multistep reaction system with the presence of parallel reactions at a certain temperature or time of the reaction.

5.3 Results and discussion

5.3.1 Calcination of Calcite, Dolomite and Siderite

Calcite, dolomite and siderite are carbonate minerals characterized by having a higher concentration of calcium for calcite, calcium and magnesium for dolomite and iron for siderite. The decomposition of calcite and dolomite produces a metal oxide and carbon dioxide (Reactions 5.2 & 5.3).

$$CaCO_3 \rightarrow CaO + CO_2 \quad (5.2)$$

$$CaMg(CO_3)_2 \rightarrow CaO + MgO + 2CO_2 \quad (5.3)$$

Whereas siderite's calcination seems to simply produce wüstite (Reaction 5.4), in reality it undergoes a complex decomposition that highly depends on the ambient atmosphere [25, 26]. Wüstite is rapidly oxidized to hematite (Fe_2O_3) in the presence of air. Therefore, the calcination of siderite under an air atmosphere can be considered as the direct production of hematite from siderite (Reaction 5.5).

$$FeCO_3 \rightarrow FeO + CO_2 \quad (5.4)$$

$$2FeCO_3 + 1/2O_2 \rightarrow Fe_2O_3 + 2CO_2 \quad (5.5)$$

These minerals are often associated with impurities that might affect the calcination process. Those impurities are usually manganese or iron for calcite and dolomite; while natural siderite samples are associated with calcium, magnesium and manganese (Table 5.1). In the latter case, impurities can be found with the iron carbonate by direct substitution of iron in the lattice of the mineral, or as a different mineral, i.e., calcite or dolomite [27-29].

Thermal behavior of these carbonate minerals, in particular, calcite and dolomite, have been widely investigated over time. Those investigations showed the similarity in the decomposition between calcite and dolomite; whose order of reaction was mostly between 0 and 1 with more frequent values ranging from 0.2 to 0.6, due to the asymmetry of the surface reaction of such minerals, with varied activation energy and pre-exponential factor [13, 30]. Table 5.3 summarizes previous kinetic studies performed on calcite, dolomite and siderite.

Table 5.3 Comparison of kinetic triplets of calcination of calcite and dolomite with the literature

Mineral	$T_{reaction}$ (ºC)	d_p (µm)	Mass (mg)	Ea (kJ/mol)	ln (k_0)	n [b]	Ref.
Calcite ($CaCO_3$)	500-700	100-125	- [a]	157.0	9.79	0.30	Blecic [13]
	800-950	< 150	400	179.5	12.31	0.32	Kissinger [22]
	700-800	1.7-2.0 (mm)	60-100	174.0	10.61	0.74	Britton et al [18]
Magnesite ($MgCO_3$) or Dolomite ($CaMg(CO_3)_2$)	500-700	100-125	-[a]	133.0	12.09	0.56	Blecic [13]
	800-950	< 150	400	135.5	12.58	0.56	Kissinger [22]
	700-800	1.7-2.0 (mm)	60-100	149	12.44	0.58	Britton et al [18]
Siderite	450-650	< 74	20	18.7 (Spathic)	-[a]	3.5	Dhupe et al. [25]
	350-550			40.0 (Indian)	- [a]	3.0	
	320-500	[c]	20	77	- [a]	1.5	Jagtap et al. [31]
	400-550	[a]	14	192 (natural)	21.65	1	Gotor et al. [32]
	220-300			106 (synthetic)	15.88	2	

[a] Data not mentioned in the reference
[b] The model for calcite & dolomite $n(1-\alpha)^{1-1/n}$, in literature: $(1-\alpha)^n$; for siderite: Model Avrami-Erofeev: $(n(1-\alpha)[-ln(1-\alpha)]^{1-1/n})$
[c] Multiple sizes were studied: 162 µm; 420 µm; 998 µm; 2375 µm [31]

Previous studies in the literature reported that the Avrami Erofeev model accurately described the calcination of calcite. Nonetheless, there is a discrepancy in terms of reaction order, which varies from 1 to 3.5, and activation energy (Table 5.3).

The diversity between the kinetic parameters for the same mineral is mainly caused by experimental conditions and the mineral, in addition to the procedure employed for the determination of kinetic parameters.

Experimental conditions, such as heating rate, isotherm or non-isotherm investigation, the gas concentration (e.g., air vs pure oxygen) or its flow rate, and the mass or size of the feed are usually a source of discrepancy in a comparison between kinetic studies [33-35].

Dhupe and Gorkan 1990 and Jagpat et al. 1992 proved that the selection of the analysis technique, i.e., isotherm or non-isotherm, influences the kinetic study [25, 31]. Nonetheless, any clear conclusion could be extracted by comparing their studies.

The mass and size of the sample can lead to external mass transfer limitations when an excessive mass of the sample is used for the test, or to internal diffusion limitations when the size of the sample is excessively large. Both can cause a noticeable difference between the surface and the center of the particle, thus impacting the temperature range at which the calcination of the carbonate takes place. This is the case for the studies carried out by Britton et al. 1952, whose particle size was a few mm and used a 0.4 g mass, and by Kissinger 1957, whose sample mass was between 60 and 100 mg (Table 5.3) [18, 22, 33].

Blecic 1983 [13] seems to have overcome these limitations for his studies regarding the calcination of calcite and dolomite. However, the accuracy of the results cannot be confirmed due to the lack of data on the sample mass used during his studies.

The mineral can affect the kinetic parameters as a function of its origin, shape, size, purity, elemental composition and/or crystallography. In this regard, siderite studies were more consistent, since none of the aforementioned studies regarding calcite and dolomite calcination commented on the purity of the sample used for their studies. One of the main aspects could be the mineral's origin and purity since the concentration of calcium, magnesium or manganese in natural siderite can influence the kinetic analysis. In fact, Dhupe and Gorkan 1990 proved the effect of the mineral origin by comparing the kinetic analysis on two siderites from different origins (Table 5.3) [25].

In this work, the kinetic study on the calcination of calcite, dolomite and siderite was developed taking into consideration the parameters mentioned above that might affect the study. Our theoretical study showed there must be no mass transfer limitation in the calcination of these minerals with the selected size distribution (Table 5.1); while the use of a low sample mass, i.e., approximately 10 mg, and high gas flowrates avoided external diffusion limitations and CO_2 accumulation within the sample.

The calcite and dolomite samples of this research were pure, as discerned from the XRD data (Figure 5.2) and the elemental analysis performed (Table 5.1). Even though calcium magnesium and manganese were detected within the siderite sample (Table 5.1), these elements belonged to

the presence of ankerite within the sample (Figure 5.2). Ankerite (11 wt.%) and quartz (30 wt.%) were identified as the main impurities in siderite by XRD.

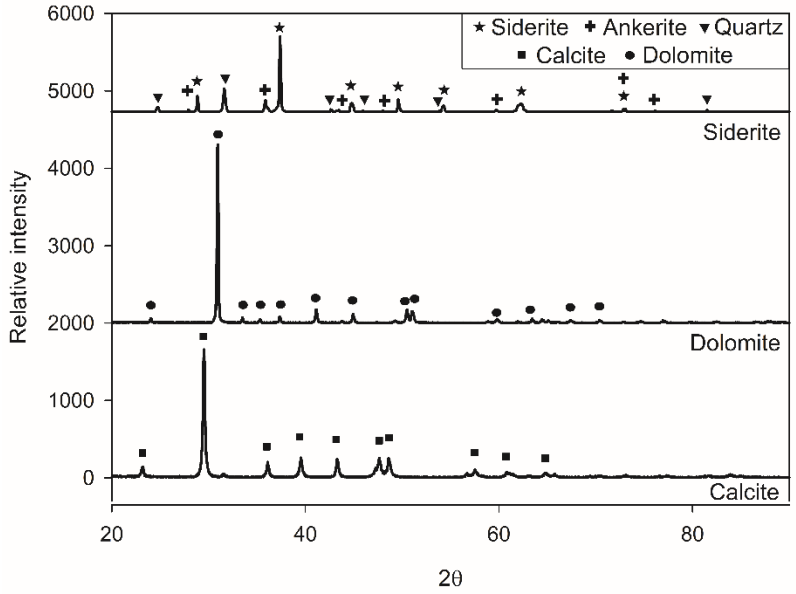

Figure 5.2 XRD analysis of the calcite, dolomite and siderite minerals

The calcination study of the highly pure calcite and dolomite showed that their decomposition, depending on the heating rate, starts at a temperature between 540 and 650 ºC, and is quite similar (Figure 5.3). Such high temperature behavior resemblance is not surprising due to the physical similarities between these two minerals, such as structure, hardness or crystallography [15].

During calcination, both minerals show a one step decomposition with a final mass of approximately 55.8 wt.% for the calcite and 54.5 wt.% for dolomite; the difference in this case should be related to the presence of magnesium in dolomite (Figure 5.3) [15]. The production of CO_2 and its partial pressure might affect the process by a reversible reaction of the solid-state decomposition process [16-20, 36]. Nevertheless, in this research, the reversibility was minimized by using a high flow rate of gas to ensure the purge of gas from the sample and the furnace was satisfied (Appendix B) [19, 20]. Under our experimental condition, the partial pressure of CO_2 would be at least 10 times lower than the pressure of the system [16].

For calcite, the mass loss occurring during calcination follows a similar trend as in pure calcium carbonate calcination (mass remaining 56 wt.%). The 0.2 wt.% difference is caused by the moisture content of the mineral that evaporates at temperatures between 100 and 180 ºC. Moisture does not show up in the analysis used to evaluate the purity of the mineral and must be considered upon calcination.

The calcination of natural siderite at a heating rate of 5 ºC/min started at approximately 480 ºC and ended at 750 ºC (Figure 5.3). The presence of impurities in the mineral powder affected the decomposition. In fact, due to the presence of ankerite in the sample, the decomposition of the mineral occurs in two steps, which are detectable from TGA plots of Figure 5.3. In other words, following the calcination of iron carbonate in a temperature range of 480 to 610 ºC, there is a secondary decomposition trend above 610 ºC that corresponds to the calcination of ankerite impurity. It must be noted that the presence of quartz (30 wt.%) in the sample affected the final mass loss represented in the thermogram.

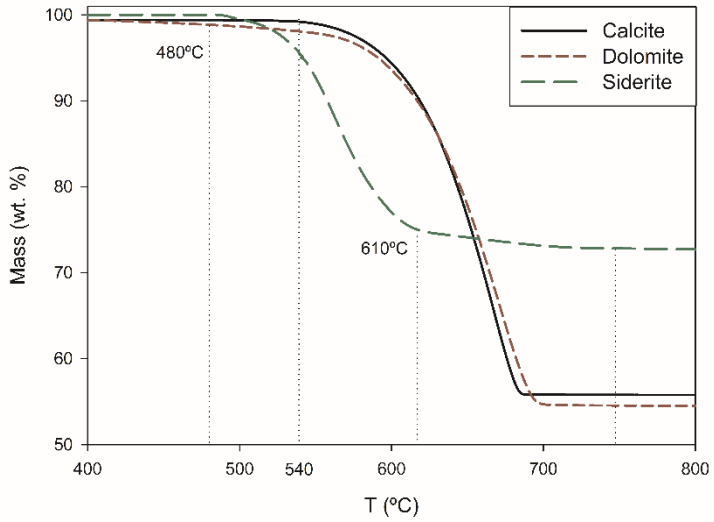

Figure 5.3 TGA curve of the decomposition under air atmosphere of Calcite, Dolomite & Siderite

Taking the correction of the sample temperature into account at multiple heating rates (see Section Appendix A), the computational techniques were followed to estimate kinetic parameters corresponding to the calcination of calcite, dolomite and siderite. Concerning the ICF technique, activation energies were estimated for various conversions (every 0.05).

Table 5.4 presents kinetic parameters estimated by the computational techniques. The apparent activation energy of calcite estimated by ICF and FM was 188.0 kJ/mol and 163.4 kJ/mol, respectively. It was noted that the deviation in the estimated activation energy was quite negligible due to the correction of the sample temperature, i.e., less than ± 5 kJ/mol.

Subsequently, the DMF and IMF techniques were applied for each reaction model presented in Table 5.2 to find the one that results in an activation energy that is closest to those of ICF and FM techniques. Consequently, the contracting cylinder model that follows a shrinking core approach was found to be the most appropriate one to describe the kinetic of calcite calcination, i.e., a reaction model in the form of $n(1-\alpha)^{1-1/n}$ while reaction order (n) is 2. Taking this model, the activation energy is estimated to be between 217.3 kJ/mol and 209.4 kJ/mol, respectively, by the IMF and DMF techniques, whereas the estimated $\ln k_0$ value was similar from both techniques, i.e., 23.9 versus 23.5 (Table 5.4).

Correspondingly, the calcination of dolomite follows a contacting cylinder model with a reaction order of 2. Its activation energy estimated by IMF and DMF techniques was between 223.1 kJ/mol and 209.1 kJ/mol, respectively, with $\ln k_0$ of 24.8 and 23.1.

The contracting cylinder model defines a reaction that rapidly occurs on the surface of the particle and progresses through the center of the particle. The reaction is thus controlled by the reaction at the interface between the product layer formed and the reactive surface. Therefore, the nucleation of the product, e.g., calcium oxide, rapidly occurs at the surface of the crystal.

In comparing activation energy estimates by ICF and FM techniques, there is an appreciable difference. In fact, the contribution of the heating rate in the ICF technique on conversion (Eq. 5.7) helps correct the estimation of the activation energy, which the FM technique lacks.

The proximity of the apparent activation energy of calcite and dolomite calcination confirms the analogy in thermal behavior of the alkaline metal carbonates. The difference observed between the activation energy of calcite calcination and that of dolomite by ICF and DMF approaches should be due to the variation in the composition of the minerals. Manganese was quite negligible in both minerals (<0.31 wt.%). Nonetheless, magnesium concentration was below 0.2 wt% in calcite whereas it was 10.6 wt% in dolomite.

Table 5.4 Kinetic parameters of calcite, dolomite and siderite estimated by ICM, FM, IMF and DMF techniques

	Ea (kJ/mol)[a]				ln k_0		n[b]	
Mineral	**ICF**	**FM**	**IMF**	**DMF**	**IMF**	**DMF**	**IMF**	**DMF**
Calcite	188.0 (±4.1)	163.4 (±4.2)	217.3 (±2.8)	209.4 (±1.8)	23.9	23.5	2	2
Dolomite	181.4 (±4.2)	161.5 (±3.8)	223.1 (±2.0)	209.1 (±4.0)	24.8	23.1	2	2
Siderite	247.1 (±2.1)	160.9 (±2.8)	246.3 (±7.4)	203.9 (±1.8)	34.2	27.0	1	1

[a] Reported errors are the standard deviation of data obtained from different conversions (in ICF technique) or heating rates

[b] Reaction models: calcite & dolomite: $n(1-\alpha)^{1-1/n}$; siderite: $n(1-\alpha)[-ln(1-\alpha)]^{1-1/n}$

The use of the ICF technique on siderite confirmed that calcination took place in two distinguishable calcination steps. At 580 ºC, a change in the activation energy was noticeable. Below this temperature, the activation energy was 247.1 kJ/mol, whose respective conversion was 70%. This section corresponded to the sole decomposition of siderite. Above that temperature, the mean activation energy was 314.9 kJ/mol; this value is higher than the estimated activation energy of calcite and dolomite (Table 5.4) due to the mixture of impurities and the higher manganese content.

After the evaluation of various kinetic models (Table 5.2), the Avrami Erofeev model, in the form of $n(1-\alpha)[-ln(1-\alpha)]^{1-1/n}$, best described the calcination of siderite. This model carries the conception of nucleation and nuclei growth; the former is possibly related to an increase in mass due to the oxidation of wüstite (FeO) to hematite (Fe_2O_3).

The reaction order of the Avrami Erofeev model was found to be between 1 and 1.2. Subsequently, estimating the ration order to be unity, Table 5.4 presents the kinetic parameters of siderite calcination employing IMF, DMF, ICF and FM techniques. The apparent activation energy for fitting techniques was found to be above 200 kJ/mol, which differs from the 160.9 kJ/mol found by the free model (Table 5.4).

It is discernible from Table 5.4 that there was a considerable difference between activation energy estimates from free model techniques (ICF and FM) and model fitting techniques (IMF and DMF). In fact, a free model approach considers the activation energy independent of the reaction mechanism; while fitting techniques are dependent on the reaction model assumed. In the latter case, the activation energy is dependent on the reaction model assumed and can thus differ from one model to another.

Experimental data of conversion of calcite, dolomite and siderite versus temperature was compared with the conversion based on estimated kinetic parameters from each computational technique. Consequently, the plots associated with DMF, being the methodology with the lowest residual sum of squares, displayed the best decomposition kinetics for the three minerals (Figure 5.4 a, b & c). The validation of the kinetics was done by evaluating the deviation between the calculated results by DMF and the experimental data at different values of activation energy and its corresponding pre-exponential factor, presented in the form of contour maps in Appendix C.

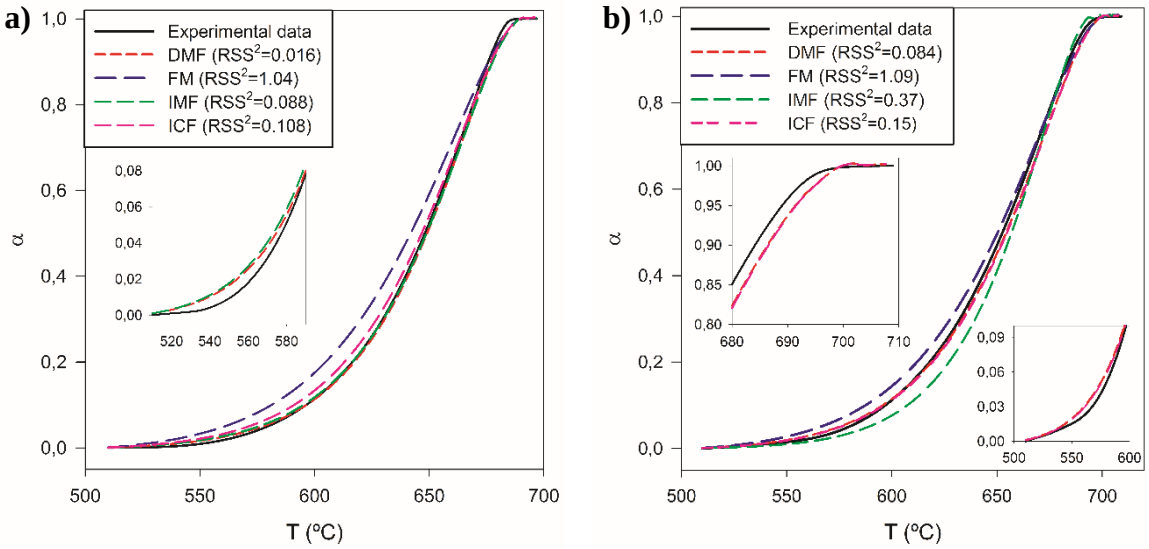

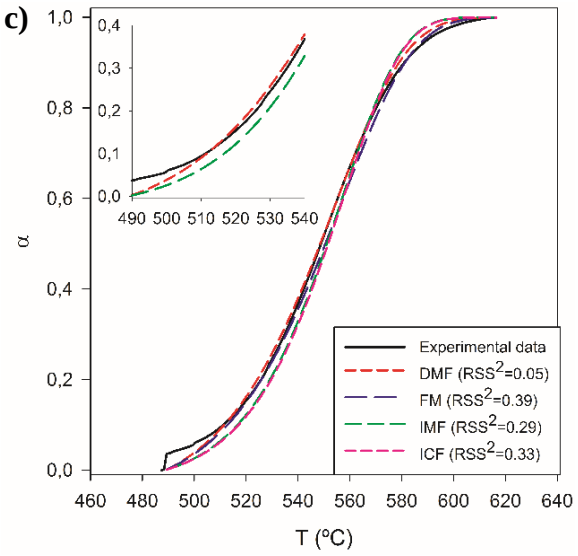

Figure 5.4 Kinetic validation of: a) Calcite, b) Dolomite, c) Siderite

5.3.2 Ankerite

Ankerite is an iron calcium carbonate mineral whose pure form can be described as $CaFe(CO_3)_2$. Nonetheless, this mineral is often associated with magnesium and manganese making its real formulation to be $Ca(Mg_{1-x}\ Fe_x)(CO_3)_2$. From the composition of the ankerite (Table 5.1), it was determined that the ankerite used in this study was in the form of $Ca(Mg_{0.35}\ Fe_{0.65})(CO_3)_2$.

Like the other carbonates, the calcination of ankerite is characterized by the production of carbon dioxide, but the presence of the calcium-magnesium-iron bonding influences the thermal decomposition trend compared to simple carbonate minerals, e.g., calcite or siderite.

Figure 5.5 depicts that calcination started at 500 ºC and three decomposition steps could be detected from mass variation upon applying calcination at a heating rate of 20 °C/min to the ankerite powder of this research. The steps were distinctive in the DTGA graph and started to occur at approximately 500 ºC, 620 ºC and 680 ºC. Similar ankerite decomposition temperatures have been reported in literature [27]; it is worth mentioning though that the concentration of magnesium and manganese in the ankerite can change the decomposition temperature and kinetics.

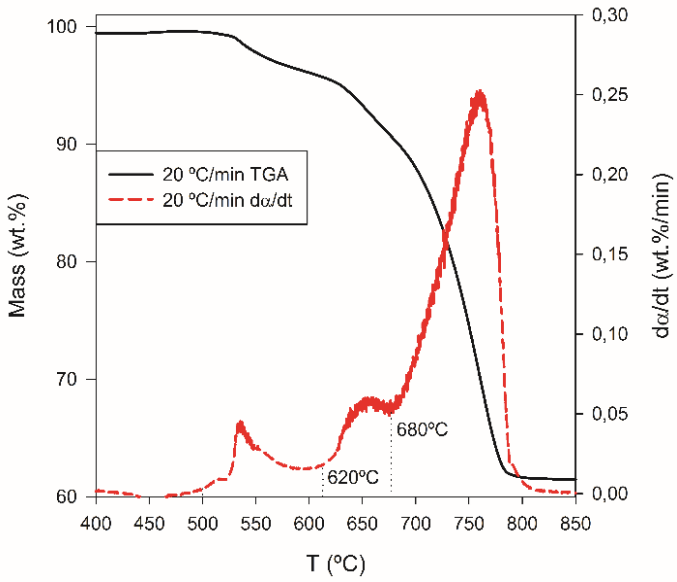

Figure 5.5 Decomposition of ankerite under air atmosphere

XRK analysis at multiple temperatures was carried out to validate and elaborate the observed reaction steps (Figure 5.6a).

The diffractogram of the raw ankerite revealed the presence of siderite (Figure 5.6a), which contributes to the 1st reaction step that was observed between 500 and 600 ºC from the thermogravimetric analysis (Figure 5.5). In fact, the presence of iron oxide after a thermal treatment at 620 ºC indicates that siderite calcination took place according to reaction 5; however, ankerite was still present in its raw form at this temperature (Figure 5.6a (b)).

The decomposition of ankerite started at 620 ºC and continued until 680 ºC. According to the diffractogram in Figure 5.6a (c), the first reaction was the calcination of the iron-magnesium complex ($(Mg_{0.24}\ Fe_{0.76})CO_3$) (Reaction 5.6) followed by the formation of iron oxide carbonate ($Fe_2O_2CO_3$) (Reaction 5.7). These reactions can be combined as Reaction 5.8.

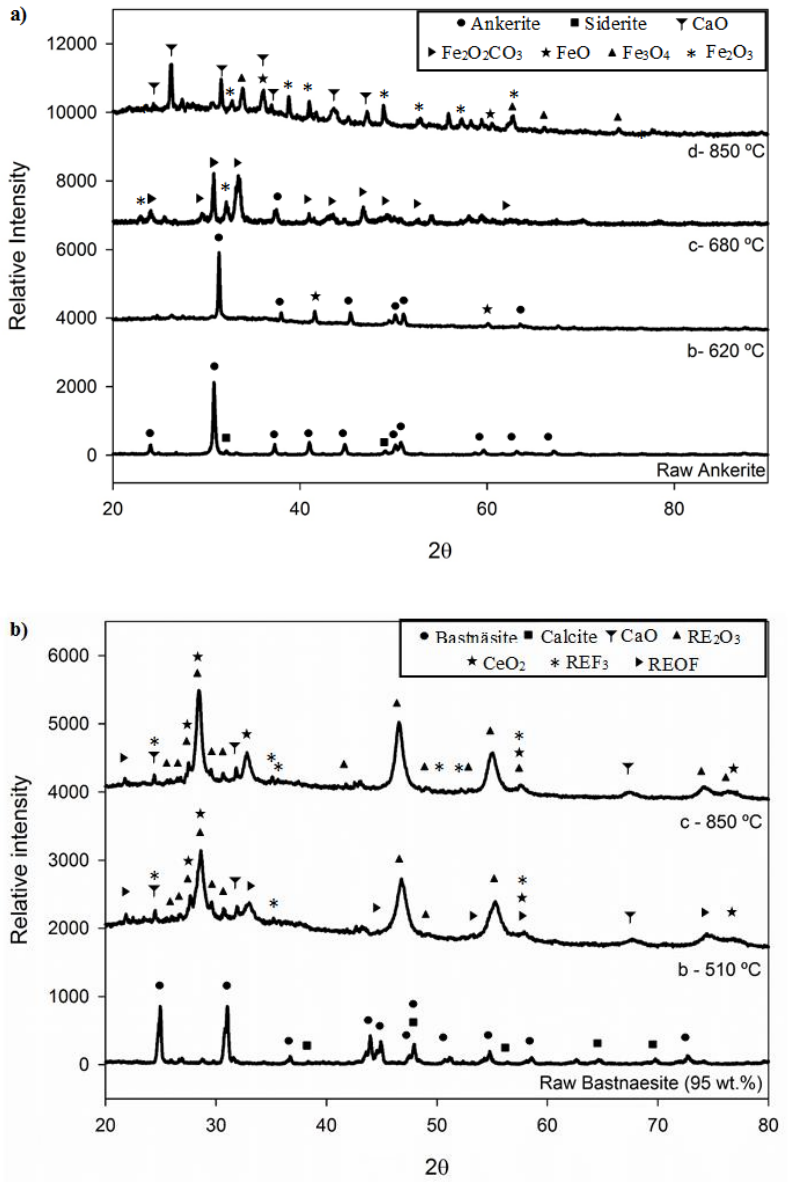

Figure 5.6 Diffractograms of decomposition of: a) Ankerite; b) Bastnaesite (RE = Rare Earth Elements) at various temperatures

The third decomposition step corresponds to the calcination of the iron oxide-calcium carbonate complex where, actually, calcium carbonate is decomposed (Reaction 5.9). Due to the presence of iron oxide, the kinetics diverges slightly from the thermal behavior of calcite. Nonetheless, this last reaction could not be proved by XRD since it only considered the individual oxides, e.g., CaO or

Fe_2O_3 (Figure 5.6a (d)), and not the iron calcium oxide complex. Similar reaction mechanisms were developed by DTA and DSC analyses by Kulp et al. 1951 and Dubrawski et al. 1988 [28, 37].

$$Ca\left(Mg_{(1-x)}Fe_x\right)(CO_3)_2 \rightarrow xFeO + (1-x)MgO + CaCO_3 + CO_2 \quad (5.6)$$

$$2FeO + CO_2 \rightarrow Fe_2O_3 + CO \quad (5.7)$$

$$\frac{2}{x}Ca\left(Mg_{(1-x)}Fe_x\right)(CO_3)_2 \rightarrow (1-x)MgO + Fe_2O_3 \cdot (CaCO_3)_{2/x} + \frac{2}{x}CO_2 \quad (5.8)$$

$$Fe_2O_3 \cdot (CaCO_3)_{2/x} \rightarrow Fe_2O_3 \cdot (CaO)_{2/x} + \frac{2}{x}CO_2 \quad (5.9)$$

The description of these steps can thus be transposed into a kinetic model by studying a two-step reaction for the ankerite mineral. To develop the kinetic study, it is imperative to state the temperature range for the reaction for each step.

Based on the DTGA of Figure 5.5, it can be assumed that at some point both reactions overlap since before the first reaction of ankerite ends, there is a small plateau and an increase in the reaction rate indicating that the calcium carbonate calcination has already started. This assumption of a reaction overlap seems to occur between a 25 ºC temperature range, from 665 to 690 ºC when a heating rate of 20 ºC/min is used. The analysis with ICF confirmed the above reaction steps and overlapping region occurred, as illustrated in Figure 5.7.

To develop the kinetic model of ankerite's calcination, first ICF was used to determine the starting and ending point of each reaction step. Then each step was analyzed individually with the DMF that proved to be more effective from previous sections.

The presence of two distinct plateaus of activation energy confirmed a two-step reaction. The first plateau corresponded to the decomposition of magnesium iron carbonate, which occurred between the beginning of calcination and approximately 665 ºC corresponding to an overall conversion of 0.14. The second plateau, related to the decomposition of the iron oxide-calcium carbonate complex, occurred between 690 ºC and 770 ºC, which in terms of overall conversion was between 0.26 and the final conversion of the reaction. Consequently, the presence of a changing activation energy between the conversions of 0.14 and 0.26 represented a transition in the reaction kinetics, which can be assigned to the overlap of Reactions 8 and 9 occurring between 665 and 690 ºC (Figure 5.7).

Applying ICF, the activation energy associated with each distinct reaction step was 265.1 kJ/mol and 251.9 kJ/mol, respectively.

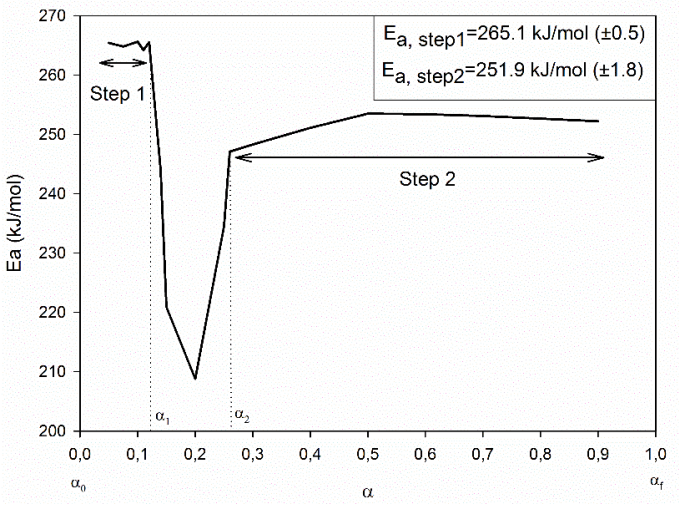

Figure 5.7 Activation energy evolution during ankerite's calcination by the isoconversional method (Temperature range: 550ºC to 770ºC)

Then the DMF technique was employed to determine the kinetic model and related kinetic parameters for each step, which are summarized in Table 5.5.

Table 5.5 Kinetic parameters of the two reaction steps of ankerite decomposition, obtained by derivative model fitting method

Reaction	Activation Energy (kJ/mol)	Ln(A)	Model
$(Mg_{0.35}\ Fe_{0.65})CO_3$	270.1	28.7	$(1-\alpha)$
$CaCO_3 \cdot (Fe_2O_3)_{0.33}$	236.6	21.8	$2 \cdot (1-\alpha)^{0.5}$

Compared to the pure mineral forms, i.e., siderite for the first reaction step and calcite for the second reaction step, ankerites' apparent activation energy for the two steps of reaction was higher. The presence of magnesium-iron and iron-calcium carbonate complexes caused this increase in the activation energy.

With respect to the activation energy analysis presented in Figure 5.7, it was attempted to develop a kinetic model to describe the overall calcination of ankerite, i.e., the two distinct stages and

intermediate overlap stage. To do so, a fractional conversion was defined for each stage as part of the overall conversion of ankerite's calcination (Eq. 5.8 & 5.9).

$$\alpha_1^* = \alpha_2 - \alpha_0 \quad [5.8]$$

$$\alpha_2^* = \alpha_f - \alpha_1 \quad [5.9]$$

Where α_0 and α_f are the initial and final overall conversion of ankerite (0 and 1, respectively). The α_1 and α_2 correspond to initial and final overall conversion within the overlap section, respectively (Figure 5.7). The α_1^* and α_2^* are the fractional conversions, delimiting where each reaction step starts and ends compared to the overall calcination of ankerite. Consequently, Eq. 5.10 described the overall reaction rate of ankerite.

$$\left(\frac{d\alpha}{dt}\right)_{Ank.} = \alpha_1^* \left(\frac{d\alpha}{dt}\right)_{step1} + \alpha_2^* \left(\frac{d\alpha}{dt}\right)_{step2} \quad [5.10]$$

Figure 5.8 illustrates that Eq. 5.10 resulted in a model that was in very promising agreement with the experimental data.

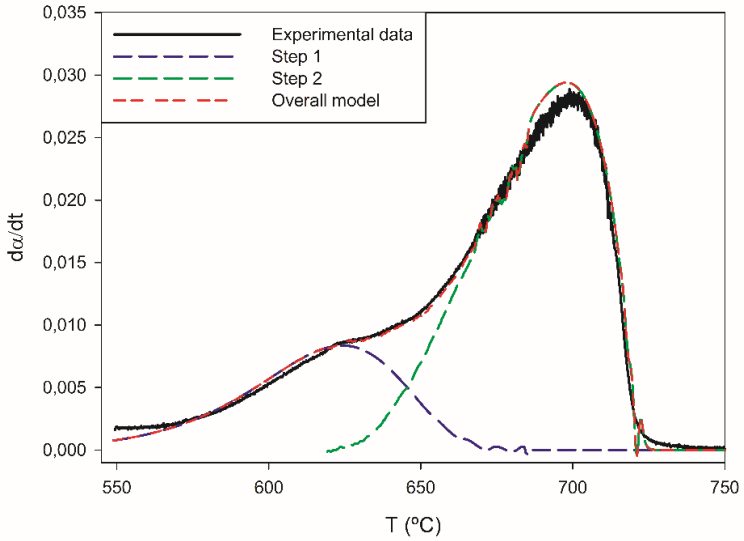

Figure 5.8 Kinetic model validation of ankerite decomposition as a function of the reaction rate

5.3.3 Bastnaesite

Despite the description of bastnaesite as a carbonate mineral, it is in fact a rare earth fluoro-carbonate, whose formula is usually simplified as REE.F.CO_3. In this study cerium bastnaesite was used (($Ce_{0.55}La_{0.34}Nd_{0.11}$).F.$CO_3$).

Bastnaesite decomposition occurs in two steps between 400 and 500 ºC, depending on the heating rate. Firstly, a gas-solid reaction producing a rare earth oxy-fluoride and carbon dioxide (Reaction 5.10) takes place at around 400 ºC. Then, a solid transformation seems to occur in parallel to the gas-solid reaction and produces rare earth oxide (RE_2O_3) and rare earth fluoride (REF_3) (Reaction 5.11) [38]. In other words, the mass loss is associated with Reaction 5.10. Therefore, the kinetic analysis was developed considering the overall Reaction 5.12, and assuming that the effect of the type and composition of the rare earth elements in bastnaesite was negligible. This assumption was made because it was impossible to discern between each rare earth fluoro-carbonate and the similar physicochemical characteristic of the rare earth elements.

Production of rare earth fluoride could be advantageous to avoid the emission of fluorine in the atmosphere, especially in the form of hydrofluoric acid (HF). If the rare earth and fluorine are recovered separately, the rare earth fluoride can then be reacted with another solid matrix, e.g., CaO, to form a less hazardous compound, e.g., CaF_2 [39].

$$REFCO_3 \rightarrow REOF + CO_2 \tag{5.10}$$

$$3REOF \rightarrow RE_2O_3 + REF_3 \tag{5.11}$$

$$3REFCO_3 \rightarrow RE_2O_3 + REF_3 + 3CO_2 \tag{5.12}$$

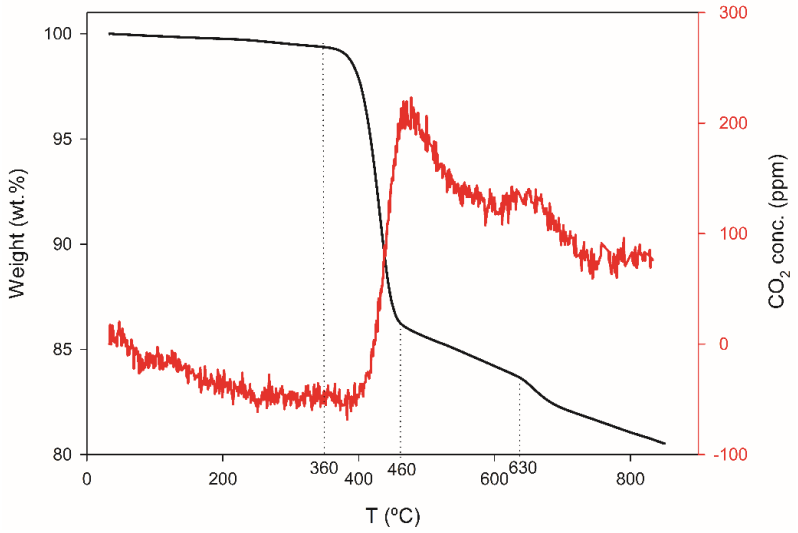

Figure 5.9 Bastnaesite decomposition under air atmosphere at 5 ºC/min (CO2 detected with multigases MKS FTIR)

Figure 5.9 illustrates the calcination of bastnaesite for a heating rate of 5 ºC/min. It is noteworthy that three slopes are observed with the thermal decomposition of bastnaesite powder. In fact, according to the evolution of CO_2 depicted in Figure 5.9, the second slope, starting at approximately 460ºC, is due to CO_2 not quickly diffusing out of the rare earth oxide lattice as Reaction 10 progresses.

Besides the two-step decomposition observed (i.e., the first two slopes in Figure 5.9), the third slope that starts at around 630 ºC corresponds to the decomposition of the carbonate impurities present within the powder in the form of calcite and dolomite (Figure 5.6b). The presence of magnesium confirms the presence of dolomite in the powder (Table 5.1).

To analyze the decomposition trends mentioned above, XRD analysis at different temperatures (XRK) was used with a 20 ºC/min heating rate (Figure 5.6b). At 510ºC, the diffractogram shows the presence of rare earth oxyfluoride, rare earth oxides and rare earth fluoride meaning that the structure change was not yet fulfilled (Figure 5.6b (b)). Also, in the same diffractogram, the presence of cerium oxide (IV) (CeO_2), which is formed from the oxidation of the cerium oxide (III) (Ce_2O_3), is discernable.

The absence of bastnaesite at 510 ºC indicates that the gas-solid reaction (Reaction 5.10) producing carbon dioxide and rare earth oxy-fluoride has ended; therefore, it confirmed that the mass loss occurring after that temperature was related to the outlet gas.

Also, the presence of rare earth oxy-fluoride, rare earth fluoride and rare earth oxide in the diffractogram at 510 ºC indicates that reactions 5.10 and 5.11 took place simultaneously and not in series as described in the literature [38]. However, the presence of rare earth oxy-fluoride at 510ºC could indicate that Reaction 5.11 started at a higher temperature than the initial decomposition of bastnaesite, or that Reaction 5.11 occurred simultaneously with Reaction 5.10 but with a slower reaction rate.

When comparing the diffractograms at 510 and 850 ºC, it was observed that only a few peaks had changed. Those peaks were the ones corresponding to the rare earth oxy-fluoride that reacts to form rare earth oxide and rare earth fluoride (Reaction 5.11), and to the calcination of impurities (Figure 5.6b).

ICF proved the reaction of bastnaesite occurred in a single reaction step, and the apparent activation energy of the mineral decomposition was 221.9 kJ/mol (Table 5.6). Although the effect of outgas CO_2 diffusion started at approximately 460 ºC (or at a 0.89 conversion), the kinetic analysis was not influenced by diffusion since the analysis was applied to the range of conversions between 0.1 and 0.9.

Utilizing the DMF technique, the first order reaction mechanism of Mampel was described the best, and an apparent activation energy of 203.3 kJ/mol was obtained (Table 5.6). This mechanism of reaction is characterized by the proportionality between the reaction rate and the amount of reactant remaining. It also introduces a crystallization or crystallographic transition, which could be from a solid transformation through an intermediate state. This was described for bastnaesite during the formation of rare earth oxide and fluoride from the rare earth oxy-fluoride that is produced as an intermediate state (Reactions 5.10 & 5.11).

Table 5.6 Kinetic parameters of bastnaesite estimated by ICF and DMF techniques

Ea (kJ/mol)[a]		**ln k_0**	**n[b]**
ICF	**DMF**	**DMF**	**DMF**
221.9 (±2.2)	203.3 (±1.9)	35.3	1
[a] Reported errors are standard deviation [b] Mampel first order model: $(1-\alpha)$			

Mampel first order reaction considers the reaction is occurring inside the entire particle at the same time. Thus, the decomposition of bastnaesite is different from other carbonates since the reaction does not evolve as a function of an interface created from the surface of the particle through its center. The reaction mechanism based on an evolving interface is thus more affected by heating rate, since it can lead to a temperature gradient throughout the particle. Bastnaesite's reaction mechanism, whose reaction takes place in the entire particle at the same time, leads to the hypothesis that the particle has the same temperature everywhere.

The use of ICF and DMF techniques has proven to be beneficial in determining the kinetic parameters of bastnaesite calcination. As represented in Figure 5.10, DMF was in good agreement with the experimental data, i.e., RSS was 0.016. The contour map developed to study the deviation between the calculated reaction rate based on the Mampel First Order kinetic model and the data also validated the kinetic parameters obtained by the DMF technique. The deviation between the model and the experimental data with the kinetic parameters was below 10% (see Section Appendix C).

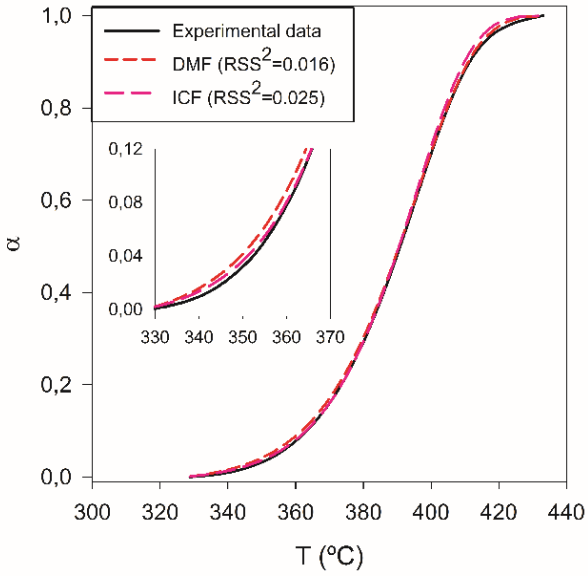

Figure 5.10 Validation of the kinetic model methodologies for bastnaesite decomposition.

Comparing the kinetic parameters of the thermal decomposition of bastnaesite to those in literature obtained by Xiang et al. 1994, there was a difference in the activation energy (49.3 kJ/mol) and a slight one for the order of reaction (1.12) [38]. Nonetheless, the same reaction mechanism (order model based) was obtained. It should be noted that a change in the kinetic parameters could be caused by the experimental conditions and the origin of the mineral (deposit and country), whose elemental mineral composition could change, thus affecting the thermal decomposition.

5.3.4 Thermal reactivity of carbonate minerals under air

The thermal behavior of carbonate minerals differs depending on their metal content, e.g., alkaline metals, such as Ca and Mg in calcite and dolomite, and other metals, such as transition metals and lanthanides in ankerite, siderite and bastnaesite.

The calcination of alkaline earth carbonate minerals directly produces the corresponding oxide of the metal, i.e., CaO or MgO in this study. Therefore, the activation energy of the reaction is representative of the decomposition reaction.

The presence of a transitional state (crystal change) affects the activation energy of the decomposition reaction. For instance, the production of the rare earth oxy-fluoride complex from

bastnaesite and the production of iron oxide II from siderite occurred with the production of REE_2O_3 and Fe_2O_3, respectively. In the case of siderite and ankerite, the reaction conditions, such as the oxygen stoichiometry, can also affect their thermal reactivity and kinetics[15].

Regardless of the reaction mechanism of each carbonate, the calcination of calcite, dolomite, siderite and bastnaesite presented similar activation energies (Table 5.7). The authors employed the Lewis structure of minerals and their bonding dissociation energy [40], and explained the observed resemblance. In fact, the breakage of a carbon-oxygen (C-O) and a metal-oxygen (M-O) occurs during calcination. Therefore, the elemental concentrations from Table 5.1 were taken to estimate the breaking bond dissociation energies (Table 5.7).

The difference observed between the dissociation bonding energy and the activation energy (Table 5.7) is caused by the effect of the temperature. Since the bond dissociation energy is often described as the enthalpy change at 298K, at higher temperatures the dissociation bonding energy decreases [41].

Table 5.7 Summary of the kinetic parameters for carbonate decomposition

Mineral		**Total bond dissociation energy $\sum \Delta H_{f,298K}$ (kJ/mol)**	**Ea (kJ/mol)**	**Ln (A)**	**model**
Calcite		822	209.4	23.5	$2 \cdot (1-\alpha)^{0.5}$
Dolomite		808	209.1	23.1	$2 \cdot (1-\alpha)^{0.5}$
Siderite		767	203.9	27.0	$(1-\alpha)$
Ankerite	**Step 1**	[a]	270.1	32.8	$(1-\alpha)$
	Step 2	[a]	236.6	25.9	$2 \cdot (1-\alpha)^{0.5}$
Bastnaesite		754	203.3	35.3	$(1-\alpha)$
[a] For ankerite the total bond dissociation energy is unknown and will be affected by the complexes formed during the calcination reaction of the mineral					

In the case of bastnaesite, some considerations were made based on the transitional step for the formation of rare earth oxy-fluoride (Reaction 5.10). This reaction was characterized in more detail by Xiang et al. [38], who described a change in the oxidation state of cerium, from 3+ to 4+, inducing the capture of extra oxygen during the production of the oxy-fluoride complex. Therefore, the bond dissociation energy necessary for bastnaesite calcination involves the dissociation of the metal-oxygen bond for the rare earth elements, the oxygen capture by cerium to change its oxidative state, and the concentration of each element in bastnaesite, i.e., the cerium concentration

in bastnaesite was 0.48 wt.%. Thus, the estimated bastnaesite bond dissociation energy was 754 kJ/mol. This energy is close to the bond dissociation energy of siderite (767 kJ/mol) and could explain why the activation energy for the calcination of both minerals is close.

5.4 Conclusions

Calcination of some carbonate minerals, such as calcite and dolomite, proved to be a unique reaction to produce calcium and magnesium oxide. It was characterized by a reaction mechanism that described the reaction evolution from an interface to the core of the particle. Whereas for more complex reactions with transitional or intermediate states, like bastnaesite, the mechanism of decomposition described a reaction that took place in the entire particle followed by nuclei growth. Such models have been seen in other minerals, e.g., siderite, in which once the gas-solid reaction was characterized by the production of carbon dioxide, it was followed by a change in crystallinity or transition state of the oxide (Table 5.7).

Focusing on a more particular matter as it is the calcination reaction of a rare earth mineral, bastnaesite decomposition proved to be of a singular case, which gas-solid reaction produced a solid in a transitory or intermediate state that further reacted to form rare earth oxide and fluoride.

Despite the validation of the kinetic model, this article proved that kinetic modeling is a biased form for obtaining kinetic parameters, since even if the activation energy is taken into consideration to define a reaction, the reaction mechanism and pre-exponential factor have a significant influence on the reaction. This article proved that kinetic parameters are not only influenced by the reaction conditions and the nature of the sample, such as temperature, reactant gas, sample characteristics (purity, size, etc.), but it is also affected by the calculation method. This study demonstrated that the use of model fitting methods (DMF or IMF) with multiple heating rate experiments can accurately describe the reaction of a solid material. Nonetheless, there is not only one answer for selecting the kinetic model methodology, since each one will influence the apparent activation energy, reaction mechanism or pre-exponential factor.

The development of a kinetic study on minerals that are often found in the same deposit could be of interest to better understand the calcination of an ore. This investigation would help to discern

which decomposition will take place at a faster rate and could thus determine the selection of a reactor residence time to achieve the desired selectivity for a specific product, e.g., the production of REO from a rare earth deposit.

5.5 Acknowledgements

The authors would like to thank the Natural Science and Engineering Research Council of Canada (NSERC/CRD) and Niobec, located in the Province of Quebec, for their financial support.

5.6 Nomenclature

α	Reaction conversion
α_i^*	Fractional conversion
C_p	Heat capacity (J/(kg K))
E_a	Activation energy (J/mol)
e	Thickness (m)
F_{air}	Air flowrate (kg/s)
$H_{r,i}$	Heat of reaction for a given carbonate decomposition reaction i (J/kg)
k	Thermal conductivity (W/(m K))
k_0	Pre-exponential factor (s^{-1})
k_0^*	$k_0^* = k_0 \exp(-E_a/(RT_r))$
m	Sample mass (kg)
m_0	Initial sample mass (kg)
m_i	Sample mass at a given time t (kg)
m_∞	Final sample mass at the end of the reaction (kg)
RSS	Residual sum of squares

S TGA's pan bottom surface (m^2)

T Temperature (K)

T_r Reference temperatura (K)

T_{in} Inlet gas temperature (K)

T_{out} Outlet gas temperature (K)

T_F Furnace temperature (K)

T_S Sample temperature (K)

R Ideal gas constant coefficient

U Global heat coefficient ($W/(m^2\ K)$)

For the kinetic model methodologies:

IMF= Integral Model Fitting method

DMF= Differential Model Fitting method

FM= Free Model method

ICF= Friedman's Isoconversional method

5.7 References

1. Giacalone, J.A., *The Market For The "Not-So-Rare" Rare Earth Elements* Journal of International Energy Policy, 2012. **1**: p. 11-18.
2. Gupta, C.K. and N. Krishnamurthy, *Extractive Metallurgy of Rare Earths*. 2004: CRC Press.
3. Mariano, A.N. *Nature of economic mineralization in carbonatites and related rocks*. in *Carbonatites: Genesis and Evolution*. 1989. London.
4. Mariano, A.N. *Economic geology of rare earth elements*. in *Reviews in Mineralogy*. 1989. Washington DC: Mineralogical Society of America.
5. Wall, F. and A.N. Mariano, *Rare earth minerals in carbonatites: A discussion centred on the Kangankunde carbonatite, Malawi*, in *Rare Earth Minerals: Chemistry, Origin, and*

Ore Deposits, A.P. Jones, F. Wall, and C.T. Williams, Editors. 1996, Chapman & Hall: London. p. 193-225.

6. Orris, G.J. and R.I. Grauch, *Rare Earth Element Mines, Deposits, and Occurrences*, U.S.G.S. USGS and U.S.D.o.t. Interior, Editors. 2002: Reston, VA, USA.
7. Verplanck, P.L., A.N. Mariano, and A.J. Mariano, *Rare Earth Element Ore Geology of Carbonatites*, in *Rare Earth and Critical Elements in Ore Deposits*, P.L. Verplanck and M.W. Hitzman, Editors. 2016, Society of Economic Geologists, Inc.: Littleton, CO, USA.
8. Habashi, F., *Extractive metallurgy of rare earths.* Canadian Metallurgical Quarterly, 2013. **52**(3): p. 224-233.
9. Grabas, K., et al., *Hydrometallurgical processing of mongolian lanthanide ore*, in *51st Annual Conference of Metallurgists, COM*, J.R. Goode, G.A. Moldoveanu, and M.S. Rayat, Editors. 2012: Niagara Falls.
10. Hadley, T. and E. Catovic, *Beneficiation and extraction of REE from northern mineral's browns range heavy rare earth project*, in *Conference of Metallurgists Proceedings* 2014, Canadian Institute of Mining, Metallurgy and Petroleum: Vancouver.
11. Kumari, A., et al., *Process development to recover rare earth metals from monazite mineral: A review.* Minerals Engineering, 2015. **79**: p. 102-115.
12. Kumari, A., et al., *Thermal treatment for the separation of phosphate and recovery of rare earth metals (REMs) from Korean monazite.* Journal of Industrial and Engineering Chemistry, 2015. **21**: p. 696-703.
13. Blecic, D. and Z.D. Zivkovic, *A new method for the determination of reaction kinetics from DTA and TG curves. Part II. Application of the method of the thermal decomposition of carbonates.* Thermochimica Acta, 1983. **60**: p. 69-76.
14. Maciejewski, M., *Computational aspects of kinetic analysis. Part B: The ICTAC Kinetics Project — the decomposition kinetics of calcium carbonate revisited, or some tips on survival in the kinetic minefield.* Thermochimica Acta, 2000. **355**: p. 145-154.
15. Reller, A., et al., *Thermochemical Reactivity of Metal Carbonates.* Chimia, 1991. **45**: p. 262-266.
16. Vyazovkin, S., et al., *ICTAC Kinetics Committee recommendations for performing kinetic computations on thermal analysis data.* Thermochimica Acta, 2011. **520**(1-2): p. 1-19.
17. Beruto, D., L. Barco, and A.W. Searcy, *CO2-Catalyzed Surface Area and Porosity Changes in High-Surface-Area CaO Aggregates.* Journal of the American Ceramic Society, 1984. **67**(7): p. 512-516.
18. Britton, H.T.S., S.J. Gregg, and G.W. Winsor, *The calcination of dolomite. Part I.—The kinetics of the thermal decomposition of calcite and of magnesite.* Trans. Faraday Soc., 1952.
19. Vyazovkin, S., et al., *ICTAC Kinetics Committee recommendations for collecting experimental thermal analysis data for kinetic computations.* Thermochimica Acta, 2014. **590**: p. 1-23.

20. Wilburn, F.W. and J.H. Sharp, *The bed depth effect in the thermal decomposition of carbonates.* Journal of Thermal Analysis, 1993. **40**: p. 133-140.

21. Brown, M.E., et al., *Computational aspects of kinetic analysis. Part A: The ICTAC kinetics project-data, methods and results.* Thermochimica Acta, 2000. **355**: p. 125-143.

22. Kissinger, H.E., *Reaction Kinetics in Differential Thermal Analysis.* Analytical Chemistry, 1957. **29**(11): p. 1702-1706.

23. Khawam, A. and D.R. Flanagan, *Solid-state kinetic models: Basics and mathematical fundamentals.* Journal of Physical Chemistry B, 2006. **110**(35): p. 17315-17328.

24. Farag, S., L. Kouisni, and J. Chaouki, *Lumped Approach in Kinetic Modeling of Microwave Pyrolysis of Kraft Lignin.* Energy & Fuels, 2014. **28**(2): p. 1406-1417.

25. Dhupe, A.P. and A.N. Gokarn, *Studies in the thermal decomposition of natural siderites in the presence of air.* International Journal of Mineral Processing, 1990. **28**: p. 209-220.

26. Gallagher, P.K. and S.S.J. Warne, *Application of thermomagnetometry to the study of siderite.* Mat. Res. BuH., 1981. **16**: p. 141-144.

27. Bailey, C.W., et al., *Investigation of the High-Temperature Behavior of Excluded Siderite Grains during Pulverized Fuel Combustion.* Energy & Fuels, 1998. **12**: p. 464-469.

28. Dubrawski, J.V. and S.S.J. Warne, *Differential scanning calorimetry of minerals of the dolomite-ferroan-dolomite-ankerite series in flowing carbon dioxide.* Mineralogical Magazine, 1988. **52**: p. 627-635.

29. Hurst, H.J., J.H. Levy, and J.H. Patterson, *Siderite decomposition in retorting atmospheres.* Fuel, 1993. **72**(6): p. 885-890.

30. Norris, A.C., M.I. Pope, and M. Selwood, *The determination of kinetic parameters for reactions involving solids.* Thermochimica Acta, 1980. **41**(3): p. 357-360.

31. Jagtap, S.B., A.R. Pande, and A.N. Gokarn, *Kinetics of thermal decomposition of siderite: effect of particle size.* International Journal of Mineral Processing, 1992. **36**: p. 113-124.

32. Gotor, F.J., et al., *Comparative study of the kinetics of the thermal decomposition of synthetic and natural siderite samples.* Phys Chem Minerals, 2000. **27**: p. 495-503.

33. Britton, H.T.S., S.J. Gregg, and G.W. Winsor, *The calcination of dolomite. Part II.- The thermal decomposition of dolomite.* Trans. Faraday Soc., 1952. **48**: p. 63-69.

34. Criado, J.M. and A. Ortega, *A study of the influence of particle size on the thermal decomposition of CaCO3 by means of constant rate thermal analysis.* Thermochimica Acta, 1992. **195**: p. 163-167.

35. Escardino, A., J. Garcia-Ten, and C. Feliu, *Kinetic study of calcite particle (powder) thermal decomposition: Part I.* Journal of the European Ceramic Society, 2008. **28**(16): p. 3011-3020.

36. Maciejewski, M. and A. Reller, *How (un)reliable are kinetic data of reversible solid-state decomposition processes?* Thermochimica Acta, 1987. **110**: p. 145-152.

37. Kulp, J.L., P. Kent, and P.F. Kerr, *Thermal study of the Ca-Mg-Fe carbonate minerals.* Journal of the Mineralogical Society of America, 1951. **36**: p. 643-670.

38. Xiang, J., et al., *Thermal decomposition behaviour of natural bastnasite crystal in calcination.* Transaction of NFsoc, 1994. **4**(4): p. 34-38.

39. Xue, B., et al., *Kinetics of Mixed Rare Earths Minerals Decomposed by CaO with NaCl-CaCl2 Melting Salt.* Journal of Rare Earths, 2010. **28**(Spec. Issue): p. 86.

40. Dean, J.A. and N.A. Lange, *Properties of atoms, radicals and bonds*, in *Lange's handbook of chemistry*, J.A. Dean and N.A. Lange, Editors. 1992, McGraw-Hill. p. 1466.

41. Durango-García, C.J., et al., *Back to basics: identification of reaction intermediates in the mechanism of a classic ligand substitution reaction on Vaska's complex†.* RSC Adv., 2016. **6**: p. 3386-3392.

42. Vekemans, O., J.-P. Laviolette, and J. Chaouki, *Thermal behavior of an engineered fuel and its constituents for a large range of heating rates with emphasis on heat transfer limitations.* Thermochimica Acta, 2015. **61**: p. 54-62.

43. Brigaud, F. and G. Vasseur, *Mineralogy, porosity and fluid control on thermal conductivity of sedimentary rocks.* Geophysical Journal, 1989. **98**: p. 525-542.

44. Cermak, V. and L. Rybach, *4.1. Thermal Conductivity and Specific Heat of Minerals and Rocks*, in *Geophysics - Physical Properties of Rocks*. 1982. p. 305-343.

45. Eppelbaum, L., I. Kutasov, and A. Pilchin, *Thermal Properties of Rocks and Density of Fluids*. 2014. p. 99-149.

46. Horai, K., *Thermal Conductivity of Rock-Forming Minerals.* Journal of Geophisical Research, 1971. **76**(5): p. 1278-1308.

47. Jacobs, G.K., D.M. Kerrick, and K.M. Krupka, *The High-Temperature Heat Capacity of Natural Calcite ($CaC0_3$).* Phys Chem Minerals, 1981. **7**: p. 55-59.

48. Chai, L. and A. Navrotsky, *Enthalpy of formation of sideriteand its applicationin phase equilibrium calculation.* American Mineralogist, 1994. **79**: p. 921-929.

49. Gysi, A.P. and A.E. Williams-Jones, *The thermodynamic properties of bastnäsite-(Ce) and parisite-(Ce).* Chemical Geology, 2015. **392**: p. 87-101.

50. Shivaramaiah, R., et al., *Thermodynamics of bastnaesite: A major rare earth ore mineral.* American Mineralogist, 2016. **101**(5-6): p. 1129-1134.

51. Lide, D.R., *CRC Handbook of Chemistry and Physics*, ed. D.R. Lide. 2005, Boca Raton, FL: CRC Press.

52. Fornarini, L., et al., *Experimental determination of La2O3 thermal conductivity and its application to the thermal analysis of a-Ge/La2O3/c-Si laser annealing.* Thin Solid Films, 2008. **516**(21): p. 7400-7405.

53. Khafizov, M., et al., *Thermal Conductivity in Nanocrystalline Ceria Thin Films.* Journal of the American Ceramic Society, 2014. **97**(2): p. 562-569.

54. Navrotsky, A., et al., *Thermodynamics of solid phases containing rare earth oxides.* The Journal of Chemical Thermodynamics, 2015. **88**: p. 126-141.

55. Zhang, Y. and I.-H. Jung, *Critical evaluation of thermodynamic properties of rare earth sesquioxides (RE = La, Ce, Pr, Nd, Pm, Sm, Eu, Gd, Tb, Dy, Ho, Er, Tm, Yb, Lu, Sc and Y).* Calphad, 2017. **58**: p. 169-203.

56. Westrum, E.F. and A.F. Beale, *Heat Capacities and Chemical Thermodynamics of Cerium(Iii) Fluoride and of Cerium(Iv) Oxide from 5 to 300°K.1.* The Journal of Physical Chemistry, 1961. **65**(2): p. 353-355.

CHAPTER 6 ARTICLE 2: KINETIC STUDY OF CALCINATION OF A RARE EARTH ORE

Adrián Carrillo García, Mohammad Latifi and Jamal Chaouki

Process Development Advanced Research Lab (PEARL), Chemical Engineering Department, Polytechnique Montreal

C.P. 6079, Succ. Centre-ville, Montreal, Quebec, Canada, H3C 3A7

(Journal of Rare Earths, submission date: October 9th 2019)

ABSTRACT

Herein, the calcination of a rare earth carbonatite ore from Quebec, Canada, was investigated. The established mechanism of the ore showed the calcination of rare earth bearing minerals occur very differently: bastnäsite decomposes at relatively low temperatures, around 400 ºC, while monazite only decomposes through the interaction with associated minerals by solid-solid reaction at high temperatures, above 700 ºC.

Based on the individual calcination kinetics of the minerals found in the ore, a comprehensive kinetic model was developed that represents the calcination kinetics of the whole ore. The interaction of monazite with calcium oxide based on its association within the ore was introduced to estimate the rare earth oxide production during the calcination. The model was firstly developed for smaller particle sizes which, when increased, had a negative effect on the reaction rate. Accordingly, the model was adapted to the change of particle size by including a coefficient based on the physical particle size cuts parameters such as superficial area, density and particle diameter.

KEYWORDS

Rare Earth Elements; Bastnäsite; Monazite; Carbonatite; Kinetic Modeling; Calcination

6.1 Introduction

Rare earth elements (REE) are metals represented as the lanthanides, yttrium and scandium that are easily found worldwide since they are found in hundreds of minerals [1, 2]. Despite their low-grade presence in many minerals, they are found with a significant grade in bastnaesite (fluoro-carbonate), monazite (phosphate) and xenotime (phosphate) [1-3].

The market of are earth elements is vast, and their application spectrum covers from energy to high technological fields [1, 4-6], increasing the interest in the development of separation processes [3, 6, 7]. A complex network of units, which could be simplified as a four-stage process, characterizes a REE extraction process. At first, the ore is recovered from the deposit and its size is reduced to a transportable and treatable size. Then, the process requires an increase in the grade, taking place during physical beneficiation [8]. From the concentrated sample, the extraction of other metal impurities, e.g. iron, is necessary. This step is usually done by the hydrometallurgical treatment. Nonetheless, pyrometallurgical units followed by milder leaching processes could be used to produce a highly REE concentrated liquor [1, 3, 6]. Finally, to produce pure rare earth elements and to increase their value, a final purification and an individual separation of the lanthanides is necessary [9].

The pyrometallurgy is a type of operation, also called calcination, that has mainly been historically used for the production of metal oxides such as iron and calcium oxide [10-14]. Its use in the rare earth industry points to the same goal of oxide production. Yet, depending on the step of the process where it is used, the ending target varies. For instance, when used at the end of the process, calcination is about to produce oxides as final product.

Thermal decomposition of the concentrate of rare earth bearing ores has been reported as a way for less consumption of chemical reagents in the downstream hydrometallurgical steps [13, 15-18]. However, they lack a detail study of the reaction kinetics. Nonetheless, we developed a process where we produce rare earth oxide directly from the calcination of the ore; it is to minimize the process complexity by bypassing the physical beneficiation of the ore. Since the calcination reactor is the core part of the process, a realistic understanding of the calcination reactions was necessary for process scale-up. The establishment of a reaction mechanism and a kinetic expression relating the decomposition rate of a rare earth containing ore to its mineral composition and the operating

conditions would be of interest to predict the most appropriate conditions to achieve a complete calcination of the ore and a full conversion to produce rare earth oxides.

Since a rare earth bearing ore contains several minerals (rare earth bearing minerals and the gangues), our strategy was to study the kinetics of calcination of the minerals individually, and eventually, develop a model that integrates all the individual kinetics. It is noteworthy that calcination of some mineral has been already reported, e.g. calcite or dolomite [14, 15, 19-23], but we have noticed a discrepancy between the reported models. This could be due to different applied calcination conditions such as temperature or heating rate as well as particle size and purity of the minerals.

This study aimed to develop a mathematical model, that by taking into consideration the heterogeneity of the sample, can predict the decomposition of the whole ore of a rare earth elements bearing ore. The model was adapted to take into account a change in the particle size of the ore. The production of rare earth oxides was also evaluated by the calcination of bastnäsite and the decomposition of monazite by solid-solid reaction. The latter reaction took place due to the association of monazite with calcite within a particle.

6.2 Experimental and Kinetic modeling

6.2.1 Material/Minerals

6.2.1.1 Niobec rare earth's ore

The ore containing rare earth elements used in this research was provided by Niobec Inc. from a deposit in Saguenay region, in the East of Quebec, Canada. The mineral and elemental composition of the ore were obtained by QEMSCAN and Neutron Activation analysis respectively and represented in Table 6.1. Due to the heterogeneous mineral composition of the sample, only minerals with a concentration above 0.9 wt.% were represented. Carbonate minerals, i.e. calcite, dolomite and ankerite, are the main component and represent the 76.9 wt.% of the ore. The rest are mainly mineral groups such as iron oxides, micas/clays and chlorites, whose more specific forms, e.g. Clinochlore ($(Mg_5Al)(AlSi_3)O_{10}(OH)_8$) and Chamosite ($(Fe_5Al)(AlSi_3)O_{10}(OH)_8$) as chlorite

minerals, could not be differentiated by QEMSCAN analysis. QEMSCAN was performed at XPS, Expert Process Solutions, with an automated system comprising a scanning electron microscope (FEI Quanta 650F) with energy dispersive X-ray spectrometer (SEM-EDS) and the software iMeasure 5.3 for the data collection and image processing.

REEs in the ore represented approximately 2.3 wt.%, mainly light rare earths such as lanthanum, cerium and neodymium. In this sample, the REEs are found in bastnaesite ($REFCO_3$) and monazite ($REPO_4$) minerals and represent the 3.39 wt.% of the ore (Table 6.1).

Table 6.1 Mineral composition in wt.% of the samples. Composition by QEMSCAN (mineral) and NAA (elemental composition).

Mineral	**Bastnäsite**	**Monazite**	**Dolomite**	**Calcite**	**Ankerite**	**Siderite**	**Pyrite**
Niobec Ore	1.96	1.43	50.0	13.2	13.7	0.21	2.86
Certif. Material	0.10	0.60	35.4	3.10	22.6	13.0	1.30
Mineral	**Chlorite**	**Barite**	**Micas/Clays**	**Quartz**	**Apatite-REE**	**FeOs & Other**	**Other**
Niobec Ore	4.43	1.99	1.15	0.92	-	5.85	2.53
Certif. Material	5.00	8.60	0.20	0.20	3.1	0.40	6.40

6.2.1.2 Minerals

Pure minerals were received from multiple locations in the form of hard stones and were crushed and sieved to an average particle size below 300 μm. The carbonate minerals, i.e. calcite ($CaCO_3$) from Morocco, dolomite ($(Mg,Ca)CO_3$) from Ojos Negros (Teruel, Spain), ankerite ($CaFe^{2+}(CO3)_2$) from Vizcaya (Spain), bastnäsite ($REFCO_3$) from Mountain Pass (United States) were studied in a previous work.

The other minerals studied in this research and necessary to evaluate the calcination mechanism and kinetics of the ore are presented in Table 6.2. It must be noted that in the case of lumped groups of minerals, a mineral was used as a representative of the group, e.g. clinochlore as chlorite group. The selection of the mineral was based on its availability in the location studied, Quebec.

X-Ray diffraction analysis (XRD) using Panalytical (X'Pert Pro MP) with a Copper anode and a PIXcel1D detector equipment was used on the minerals to evaluate their purity qualitatively.

Table 6.2 Particle size and source of minerals

Mineral	**Monazite** ($REPO_4$)	**Pyrite** FeS_2	**Mica***	**Chlinoclore** $(Mg,Fe)_5Al_2Si_3O_{10}(OH)_8$	**Quartz** (SiO_2)	**Barite** ($BaSO_4$)
$\overline{d_p}$ **(µm)**	41.2	129.9	120.8	27.2	23.3	46.2
$d_{p,32}$ **(µm)**	10.3	13.7	33.0	8.0	4.2	2.0
Source	Eureka Farm 99, Namibia	Navajún, La Rioja, Spain	Assuçao Portugal	Quebec, Canada	Gandullas, Madrid, Spain	Mazarambroz, Guadalajara, Spain
* Mica is a mixture of minerals from the same group, e.g. muscovite $KAl_2(AlSi_3O_{10})(F,OH)_2$						

6.2.2 Procedure

The study of the calcination of a natural occurring rare earth bearing ore was developed based on its mineral content. Therefore, pure minerals were first studied individually; then their studies were lumped to have a more comprehensive overview of the ore reaction mechanism and kinetics.

Thermal study of each mineral and of the rare earth bearing ore was done in a thermogravimetric analyzer (TGA) from TA Instruments, TGA Q5000. The TGA was connected to a multi-gas FTIR for the analysis of the evolved gas produced during the high temperature test. All materials were treated with various heating rates to a maximal temperature of 900 ºC to ensure a complete calcination. Only a few milligrams of sample (9 to 13 mg) were used for calcining the samples under air with a 40 ml/min flow. To avoid the reversible reaction effect of the evolved gases, CO_2 in the case of carbonate samples and SO_2 for pyrite, the furnace was purged with a 40 ml/min flow of nitrogen.

To evaluate the decomposition mechanisms of the samples, some minerals with a complex decomposition, e.g. pyrite, were also analyzed by XRD in a heating chamber. This equipment, known as XRK (XRK900 from Anton Paar), allows the study of composition (qualitative analysis) at different temperatures.

The presence of reactions between minerals and/or products (solid-solid) was evaluated by heating a mixture of bastnäsite, calcite and monazite, previously mixed with a mortar, up to 800ºC.

Then, by comparing the results from the calcination of the mineral with the one of the ore sample from Niobec, it was possible to map the ore's reaction mechanism and know when each mineral decomposed. XRD was then used to confirm a such path of reaction, and QEMSCAN was used to characterize the concentration of species in the final product.

By knowing the reaction mechanism and the calcination kinetics of the individual minerals composing the ore, a comprehensive kinetic study describing the ore's calcination and the rare earth oxide production was developed.

6.2.3 Kinetic modeling computational analysis

6.2.3.1 Minerals

Kinetics of pure minerals was developed by following a previous study on the calcination kinetics of carbonate minerals. Based on that work, Friedman isoconversional method was used to evaluate the presence of multi-step reactions, and model fitting method was used to develop the kinetic study.

The kinetic models are based on the equation defining the reaction rate (Equation 6.1), but since the focus of this article is not the kinetic model of individual minerals, their kinetic study is presented in Appendix D.1.

$$\frac{d\alpha}{dt} = k_0^* \, e^{\left(-\frac{E_a}{R}\left(\frac{1}{T}-\frac{1}{T_r}\right)\right)} f(\alpha) \qquad [6.1]$$

Where α is defined as the conversion of the reaction, expressed as a function of the decomposition mass loss; $\frac{d\alpha}{dt}$ is the reaction rate; $f(\alpha)$ is the reaction mechanism; E_a is the activation energy (J/mol), R is the universal gas constant (J/mol K), T is the actual temperature of the sample (K), T_r is a reference temperature (K); and k_0^* is a representative of the pre-exponential (s^{-1}).

6.2.3.2 Niobec rare earth's ore

As the main objective of this work, the development of a unique rate decomposition model describing the calcination of the rare earth bearing ore was performed based on lumping the kinetic studies of its pure minerals' composition. This regrouping also considered the grade of the mineral in the ore and their decomposition.

The use of the smallest particle size range, below 20 μm, was necessary to have a size range where almost all minerals were liberated or at least partially liberated (Table 6.3). Thus, ensuring the availability of the minerals to the reactive atmosphere (air) and hence minimizing the effect of the ore particle diameter and mineral encapsulation on calcination.

Table 6.3 Mean size grain for minerals affected by thermal decomposition

Mineral	**Bastnaesite**	**Calcite**	**Dolomite**	**Ankerite**	**Pyrite**	**Chlorite**
Liberation size (μm)	14	20	27	22	25	18

Nonetheless, in order to be accurate, the overall ore model needed to account for wider particle size. Accordingly, four size cuts of Niobec's ore, i.e. below 20 μm, 37 μm, 63 μm and 125 μm, were studied by TGA, and used to develop a coefficient to improve the accuracy of the overall model.

To prove the efficiency of the coefficient, all cut sizes needed to be characterized with a pycnometer (AccuPyc II 1340) from Micromeritics and a BET micro-porosimeter (AX1C-MP-LP) from Quantachrome Instruments to respectively obtain the density and the specific surface area of each cut size prior to initializing the reaction.

6.2.3.3 Validation of the kinetic methodology

In this work, a kinetic method based on lumping studies performed on pure minerals was developed to predict the gas-solid and solid-solid reactions occurring during the calcination of a natural carbonatite deposit containing rare earth elements.

Further validation of the gas-solid kinetic methodology was done by studying the calcination of a certified reference material containing carbonatite minerals purchased from Natural Resources Canada (REE-2 Certified Reference Material for a Carbonatite with Rare Earth Elements). This sample is mainly composed of carbonatite minerals (61.1 wt.%), and its mineral composition is presented in Table 6.1. The calcination of the reference sample was performed, as for the rare earth ore, by TGA at 2 ºC/min until 800ºC.

6.3 Results and discussions

6.3.1 Reaction mechanism for the calcination of a rare earth ore

6.3.1.1 Gas-solid reactions

The decomposition study of an ore shows to be a complex mechanism due to the variability and diversity of minerals it contains. Such is the case of the ore from this study whose content was mainly characterized by carbonatite minerals but had the presence of unrecognized minerals where only their main form was known, e.g. iron oxides, chlorite, mica or clays (Table 6.1). These groups can represent a variety of minerals, e.g. chlorite could be clinochlore, chamosite, or any other mineral from the group characterized by a general formula in the form of $X_{5\text{-}6}Y_4Z_{18}$, where X could be Al, Fe^{2+}, Fe^{3+}, Li, Mg, Mn, or Ni, Y is Al, Fe^{3+}, Si, or a combination of them, and Z represents O and/or OH. These minerals altogether define the mechanism of decomposition of an ore.

The calcination of the rare earth bearing ore with a particle size below 20 μm was studied by thermogravimetric analysis represented in Figure 6.1a. After the dehydration of the ore (free and bonded water) occurring below 300 ºC with approximative 0.3 wt.% mass loss, the thermogram (Figure 6.1a) showed a multi-step reaction for the ore calcination.

The first characteristic mass loss related to the decomposition of the bearing minerals occurred at around 360 ºC with a 0.75 wt.% mass loss. The decomposition of minor grade minerals caused the low mass loss. Then, at around 475 ºC, the second calcination stage started. However, the slope of the mass loss of this step was not as sudden, and it seemed to overlap with the last reaction step

that starts at around 600 ºC. This final stage was marked by a change in the slope of the mass loss (Figure 6.1a).

Since the calcination is associated with the decomposition of pure minerals, the first objective of this study was to determine the decomposition mechanism of the ore by analyzing and comparing the pure minerals' thermal behaviour to the ore calcination. So, all samples (minerals and ore) were subjected to a thermogravimetric evolved gas analysis by connecting TGA to a multi-gas FTIR. This setup enabled to compare the produced gases and the calcination temperatures of minerals, which in some cases could be very characteristic, e.g. sulphur gases produced from pyrite's roasting, with the ones of the Niobec's ore. The mentioned thermograms and FTIR results were presented in Figure 6.1.

The decomposition of the rare earth bearing ore, represented by Figure 6.1a, produced three main gases, CO_2, CO and SO_2, and in a low amount, non-appreciable in the thermogram, steam. The production of these gases took place at different temperature ranges characterizing the previously mentioned three-step reaction.

At first, the production of SO_2 (60 ppm) and CO_2 (below 10ppm), took place in a temperature range between 350 and 475 ºC (Figure 6.1a). In a similar range of temperatures, the sulphur dioxide was characteristic of the pyrite calcination (Figure 6.1e), while the CO_2 was produced by the calcination of bastnaesite (Figure 6.1c). The decomposition of these minerals was respectively characterized to occur in the form of Reactions 6.8 and 6.1.

Successively, the second reaction step started at 475 ºC and was characterized by the production of CO_2 (40 ppm), and in a lower amount but inappreciable in the thermogram some sulphur dioxide and steam (Figure 6.1a). Compared to pure minerals' thermograms, the production of carbon dioxide, related to carbonate minerals decomposition, could be assigned to a partial calcination of ankerite (Reaction 6.2) (Figure 6.1d); while the production of sulphur dioxide and steam could respectively be associated to the decomposition of pyrite (Reactions 6.8-6.12) (Figure 6.1e) and chlorite (dehydroxylation reaction) (Figure 6.1f). The decomposition of these minerals took place in a similar temperature range interval (450-575 ºC).

The final calcination step, starting at approximately 580 ºC, was characterized by the production of CO and CO_2 (Figure 6.1a). The calcined carbonate minerals were calcite and dolomite

(Reactions 6.4 & 6.5) (Figure 6.1b), and the calcium carbonate from ankerite (Reaction 6.3). The CO was produced by ankerite's calcination (Figure 6.1d).

It must be noted that the absence of SO_3, produced during pyrite's roasting, and the almost negligible presence of steam during Niobec's ore calcination was due to the low grade of the mineral in question in the ore, and to the small amount of sample used in TGA (approximately 10 mg). Therefore, these gases were below the limits of the multi-gases FTIR.

$$3REFCO_3 \rightarrow RE_2O_3 + REF_3 + 3CO_2 \quad (6.1)$$

$$\frac{2}{x}Ca\left(Mg_{(1-x)}Fe_x\right)(CO_3)_2 \rightarrow (1-x)MgO + Fe_2O_3 \cdot (CaCO_3)_{2/x} + \frac{2}{x}CO_2 \quad (6.2)$$

$$Fe_2O_3 \cdot CaCO_3 \rightarrow CaO \cdot Fe_2O_3 + CO_2 \quad (6.3)$$

$$CaCO_3 \rightarrow CaO + CO_2 \quad (6.4)$$

$$CaMg(CO_3)_2 \rightarrow CaO + MgO + 2CO_2 \quad (6.5)$$

The association of the mineral decomposition to the steps of calcination of Niobec's ore was summarized in Table 6.4.

Table 6.4 Minerals involved in the decomposition of a rare earth ore

Reaction Step	**Step 1**	**Step 2**	**Step 3**
Temperature interval (ºC)	350-410	480-590	590-700
Mineral decomposing	Bastnaesite Pyrite (step 1)	Ankerite (Step 1) Chlorite Pyrite (Step 2)	Ankerite (Step 2) Calcite Dolomite

Other individual minerals, e.g. monazite, barite or quartz, composing Niobec's ore did not decompose at temperatures lower than 800 ºC (Figure 6.2) and thus did not intervene in the thermogravimetric analysis of the Niobec's ore.

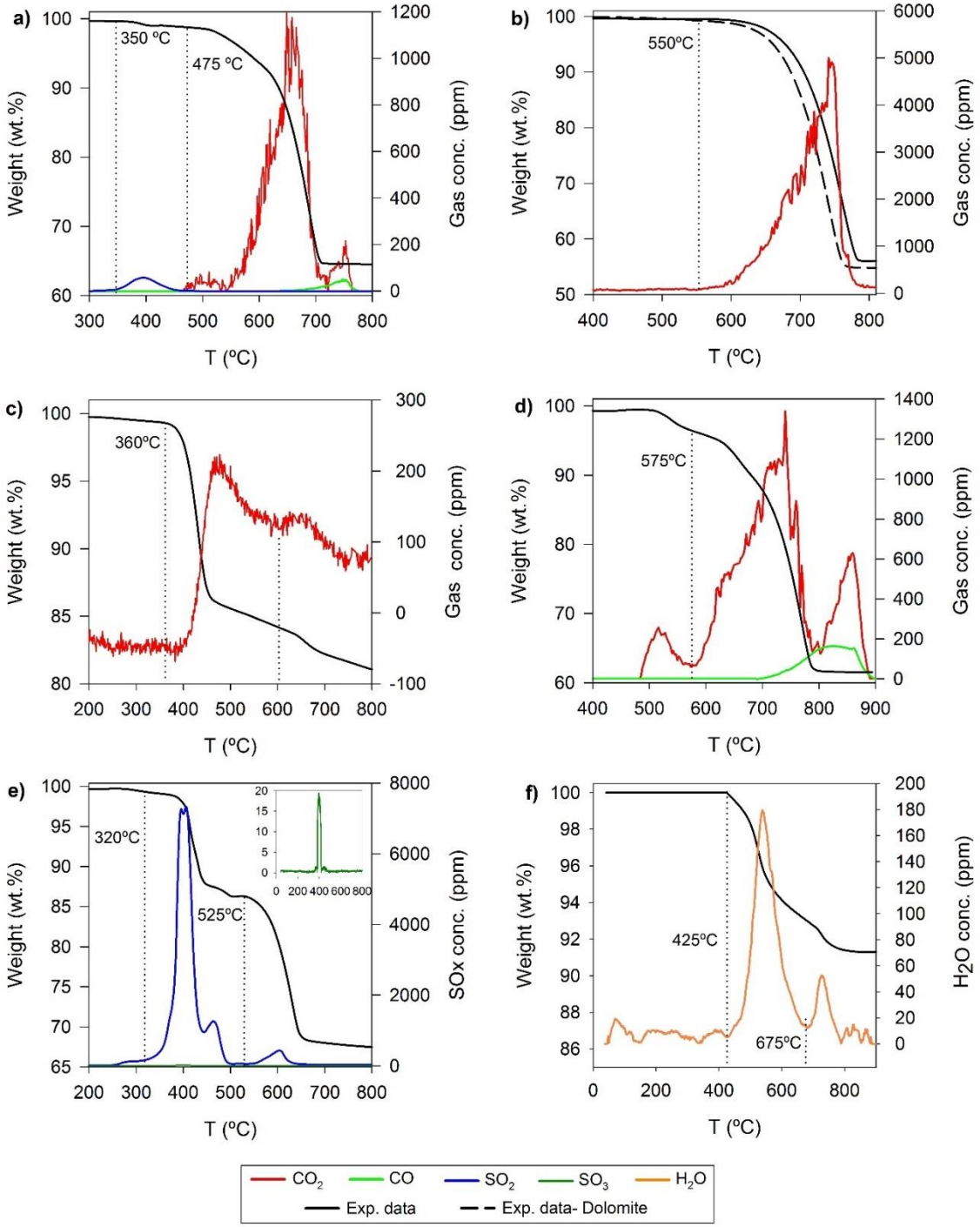

Figure 6.1 Calcination of a rare earth bearing ore and minerals with FTIR gas composition: a) Natural ore (d_p < 20 μm); b) Calcite & Dolomite; c) Bastnaesite; d) Ankerite; e) Pyrite; f) Chlorite

From those minerals, mica is a mineral group composed of a mixture of biotite, that does not have any thermal reaction below 1000 ºC, and muscovite whose decomposition usually starts at around 700 ºC [12]. Nonetheless, muscovite is sensitive to mechanical activation that forces a rearrangement of Al-OH bonds inside the mineral and, thus, the formation on the surface of the mineral of molecular bounded water [12]. In this work, muscovite stone was ground to a particle size below 300 μm, which might have allowed the slow decomposition of the mica mineral (Figure 6.2).

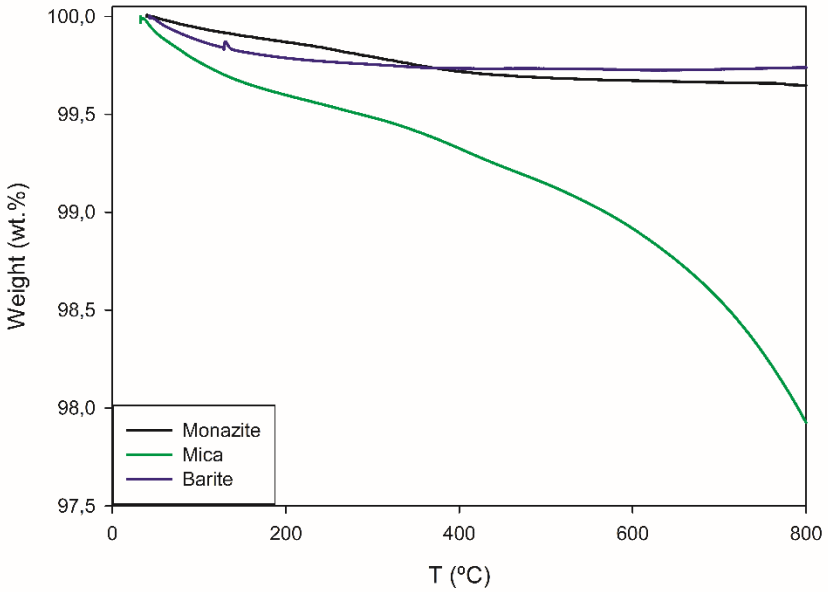

Figure 6.2 Thermal treatment of minerals: barite, mica and monazite

Despite not being decomposed at high temperature, some minerals can react together if they are in contact. A drawback of using TGA in the calcination study of an ore is the detection of solid-solid reactions since some of these reactions do not produce any gas and by extension, do not appear in the thermogravimetric analysis.

6.3.1.2 Solid-Solid reactions – Monazite decomposition

Some minerals, even though they do not decompose at high temperature (Figure 6.2), e.g. monazite [24], might undergo reactions with other minerals. For instance, some researchers have reported solid-solid reactions involving monazite, a rare earth mineral of interest to produce rare earth oxide

at high temperatures (above 600 ºC) [18, 25-27]. For such a reaction to happen, some specific conditions might occur, such as the contact between reactants and high temperature [18, 27]. Most authors used salts to accelerate the reaction, but as reported by Hikichi et al. 1980 and Xue et al. 2010, monazite can react with calcium oxide in a slower manner [25, 27].

In this research, a mixture of monazite, bastnäsite and calcite was heated to 800 ºC in a furnace, and the resulting solid mixture was analyzed by XRD (Figure 6.3). In the diffractogram of the resulting solid, the presence of fluorapatite and calcium fluoride indicated that a reaction between these three minerals occurred in the form of Reaction 6.6. Although it has not been proven, some authors report the production of calcium fluoride from the rare earth oxyfluoride as an intermediary reaction (Reaction 6.7) [18].

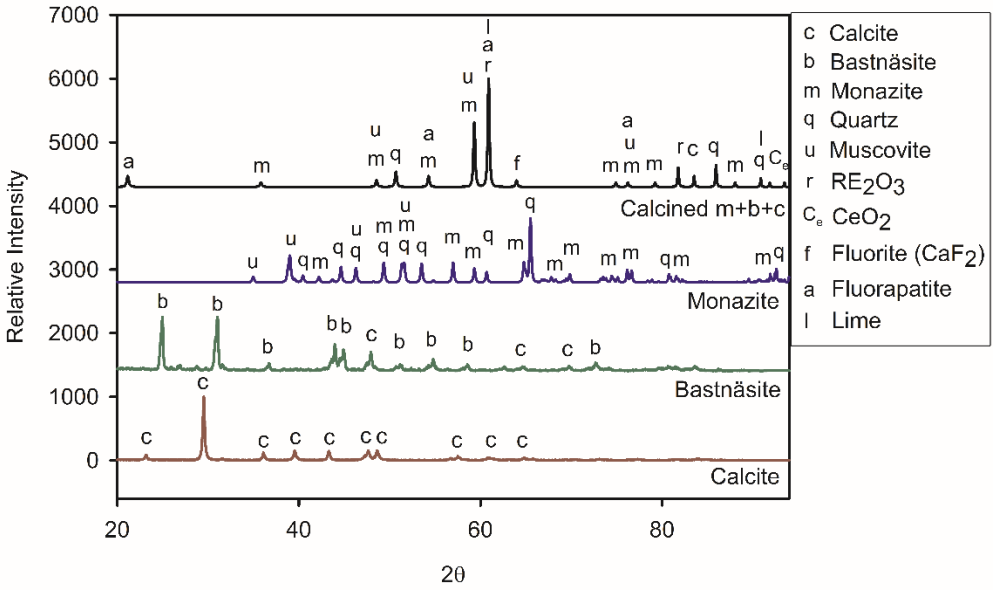

Figure 6.3 XRD of the calcination of a mixture of monazite, bastnäsite and calcite

$$3REPO_4 + REF_3 + 6CaO \rightarrow Ca_5(PO_4)_3F + 2RE_2O_3 + CaF_2 \quad (6.6)$$

$$2REOF + CaO \leftrightarrow RE_2O_3 + CaF_2 \quad (6.7)$$

The presence of a solid-solid interaction involving monazite in the form of Reaction 6.6 was validated for the calcination of the rare earth ore by comparing the QEMSCAN analysis performed on the fresh and the calcined ores. Figure 6.4 represents the modal mineralogy and monazites'

association of the calcined Niobec ore obtained by QEMSCAN analysis. As main observation by comparing the composition of the samples, oxide forms of calcium, magnesium, iron confirmed the calcination of carbonate minerals and pyrite. The detection of rare earth oxides in the calcined ore, mainly in the form of cerium oxide, also confirmed the decomposition of bastnäsite (Reaction 6.1); while the presence of fluorapatite in the treated product (0.21 wt.%) indicated that Reaction 6.6 took place. The reaction of monazite with calcium oxide was reported to be slow and to start at high temperatures [25, 27]. Compared to other studies, in this research, the calcium oxide was within the ore produced during calcination allowing the decomposition of monazite. Yet, due to the association or contact between calcium oxide and monazite within the ore, which for lower particle sizes, it is quite limited, monazite did not fully convert to rare earth oxide (Figure 6.4).

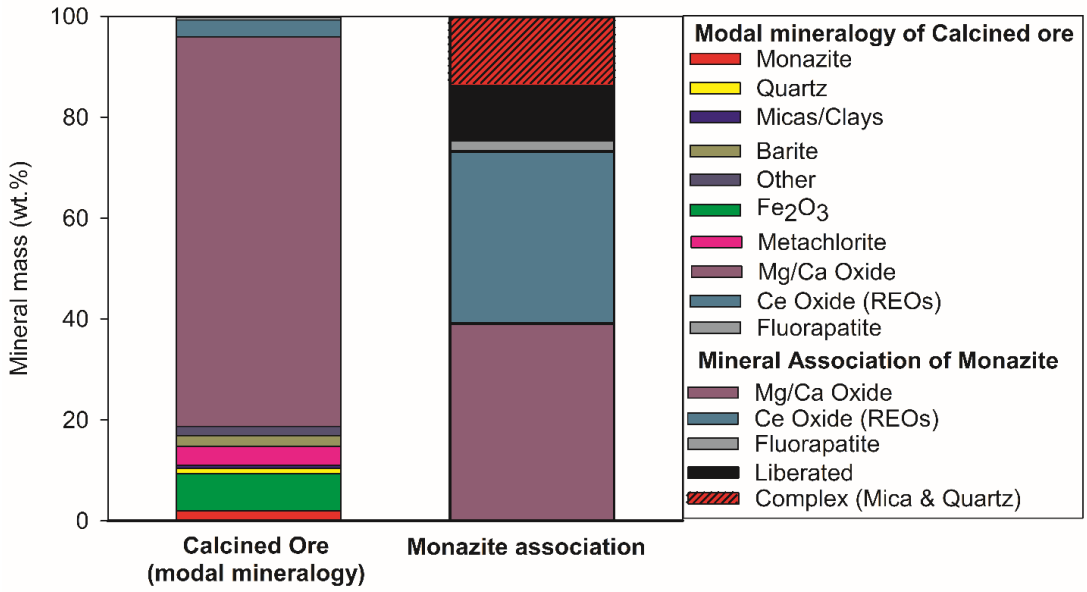

Figure 6.4 Modal mineralogy and monazite's association of the calcined Niobec ore (measured with QEMSCAN)

6.3.2 Kinetics of pure minerals

Developing a kinetic model for the decomposition of an ore, in this case, a rare earth bearing ore, is difficult due to the heterogeneous composition of the ore. In order to simplify such kinetic model, it could be done by modeling each step individually; but such model could then only be used as a

representative of that ore and would not have any physical meaning. To avoid such a lump model, the study of the reaction mechanism done in this research will be useful to develop a kinetic model based on the pure minerals' decomposition with the objective of it being able to be reused for other carbonatite ores.

6.3.2.1 Carbonate minerals

Decomposition of the carbonate minerals, i.e. ankerite, bastnaesite, calcite, dolomite and siderite, were part of a previous study, in which the kinetic model was validated with the TGA results. Their kinetic parameters are described in Table 6.5.

Table 6.5 Kinetic parameters for the calcination reaction of carbonate minerals

Mineral	Ea (kJ/mol)	Ln (A)	Reaction mechanism
Bastnaesite	203.3	33.9	$(\mathbf{1-\alpha})$
Calcite	209.4	23.3	$\mathbf{2(1-\alpha)^{0.5}}$
Dolomite	209.1	23.0	$\mathbf{2(1-\alpha)^{0.5}}$
Siderite	203.9	27.0	$(\mathbf{1-\alpha})$
Ankerite	270.1	32.84	$(\mathbf{1-\alpha})$
	236.6	25.91	$\mathbf{2 \cdot (1-\alpha)^{0.5}}$

6.3.2.2 Pyrite

Pyrite's calcination occurred in a two-step reaction (Figure 6.1e). The first reaction started at 390ºC and produced pyrrhotite and iron sulfide II (FeS) (Reactions 6.8 & 6.9); while the second step, starting at 500ºC, produced iron oxide III (Fe_2O_3) from the iron sulfides resulting of the first step (Reaction 6.11 & 6.12). Both decomposition steps followed a Mampel first order mechanism of reaction, and their respective activation energies were 240.9 kJ/mol and 280.8 kJ/mol. A more detailed description of the reaction mechanism and kinetics of pyrite can be found in Appendix D.2.1.

$$\text{Oxidation: } FeS_2 + O_2 \rightarrow FeS + SO_2 \tag{6.8}$$

$$\text{Thermal decomposition: } (1-x)FeS_2 \rightarrow Fe_{(1-x)}S + (1-2x)S \tag{6.9}$$

$$S + O_2 \rightarrow SO_2 \quad (6.10)$$

$$2Fe_{(1-x)}S + (3.5 - 1.5x)O_2 \rightarrow (1-x)Fe_2O_3 + 2SO_2 \quad (6.11)$$

$$2FeS + 7/2O_2 \rightarrow Fe_2O_3 + 2SO_2 \quad (12)$$

6.3.2.3 Chlorite

In this research, clinochlore was chosen as a representative of the chlorite group. At high temperature, chlorite undergoes a dehydroxylation reaction to produce metachlorite or other forms of chlorite [12,33,34]. Calcination of clinochlore takes place between 425 and 800ºC and can be simplified as a two-step decomposition (Figure 6.1f). The first step dehydroxylation described a second order reaction ($(1-\alpha)^2$) with an activation energy of approximately 231.7 kJ/mol; while the second reaction step was represented by a Mampel first order reaction model with an activation energy of 358.9 kJ/mol. A description of the reaction mechanism and kinetic analysis for clinochlore's calcination can be found in Appendix D.2.2.

6.3.2.4 Other pure minerals & Solid-Solid reactions

As presented in Figure 6.2, some minerals from the ore, i.e. monazite, barite and micas/clays, were not affected by temperature when treated individually. Nonetheless, the decomposition of monazite with calcium oxide and rare earth fluoride occurred at high temperature. Kinetics of this reaction was developed by Xue et al 2010, who reported it to take place in the form of Ginstling-Brundshtein model [27]. Xue et al.2010 describe two sets of kinetic parameters depending on the reaction conditions. At low temperatures (below 700ºC) the reaction was controlling the calcination; whereas, at high temperature, both diffusion and reaction controlled the calcination. For the latter, they found an activation energy of 33.8 kJ/mol [27].

6.3.3 Kinetics of the rare earth natural ore

Due to the mineralogical composition of the rare earth bearing ore, its calcination was simplified as a three-step decomposition, and the reaction mechanism was developed based on the thermograms Figure 6.1. However, despite the mechanism, a problem arises when talking about the ore, the encapsulation of minerals.

There is a clear difference between calcining a particle of a pure mineral or a bulk of minerals that might only be associated or in a worst-case scenario encapsulated. In the latter case scenario, the calcination of the encapsulated mineral is affected by the grain size since a temperature, or a reactive gas diffusion gradient might be generated inside the particle or its pores. Moreover, the decomposition of an encapsulated mineral might not appear in a thermogram at the real temperature of decomposition since it might create a pocket of gas inside the grain and diffuses slowly through the ash layer.

As a result, the model must be developed for a particle size at which minerals are liberated or at which it can at least be assumed that all minerals are exposed at the same reactive atmosphere. QEMSCAN microscopy technique was used to verify the liberation particle size of each mineral (Table 6.3), and the average grain size to ensure the liberation of the mineral was in a range between 14 and 27 µm. Accordingly, a particle size below 20 µm was selected to study the kinetics of calcination of the ore.

At each stage of the calcination, some minerals decomposed in parallel, so, the kinetic model was done considering the grade of the mineral in the ore and the calcination extent of each pure mineral individually. These considerations allowed to evaluate the contribution of each mineral to the global mass loss at each reaction step.

In the first stage, bastnaesite and pyrite (partially, only Reaction 6.8) were the only minerals to be calcined, and their respective concentration in the ore was 1.96 wt.% and 2.86 wt.%. During the individual thermal treatment of these minerals, bastnaesites mass loss was 19.76 wt.%, while the representative mass loss of pyrite's Reaction 8, i.e. production of iron sulfide (FeS), was 7.51 wt.% (the mass loss of the first stage of the pyrite represents 22.9% of the total mass loss) (Figure 6.1c & Figure 6.1e respectively). Therefore, considering the concentration in the ore and the individual

calcination of each mineral, bastnaesite and pyrite represented respectively the 64.3 % and the 35.7 % of the mass loss from the first stage of the rare earth bearing ore calcination (whose mass loss was 2.3 wt.% from the overall calcination of the ore).

Following these guidelines, it was possible to estimate the contribution of each mineral to the mass loss of each stage of the calcination; all values were illustrated in Table 6.6.

Table 6.6 Representative effect of each mineral in a reaction step of the ore calcination

Ore calcination	Step 1		Step 2			Step 3		
Mineral	Bastnaesite	Pyrite	Ankerite	Chlorite	Pyrite	Ankerite	Calcite	Dolomite
% of the reaction step	64.3	35.7	59.3	13.4	27.3	9.5	18.9	71.6
Reaction	1	8	2	-	9	3	4	5

To represent the reaction rate of each step of the ore calcination, a general equation, Equation 6.2.

$$\frac{dX}{dt}_i = \sum_{n=1}^{n=m} \sum_{j=1}^{j=\infty} x_{n,j} K(T)_{n,j} f(X)_{n,j} \quad [6.2]$$

Where, i is the reaction step during the calcination of the ore; n represents a mineral, e.g. basnaesite or calcite; j indicates for a pure mineral its reaction step; and K(T) and f(X) are the Arrhenius equation and the reaction mechanism for a mineral n in its step j.

As a result, the reaction rate equation for each step of the calcination of a rare earth bearing ore was defined in Equations 6.3 to 6.5.

Reaction Step 1:

$$\frac{dX}{dt}_1 = 0.643K(T)_{bast}(1 - X_1) + 0.357K(T)_{pyr,1}(1 - X_1) \quad [6.3]$$

Reaction Step 2:

$$\frac{dX}{dt}_2 = 0.593K(T)_{ank.1}(1 - X_2) + 0.273K(T)_{pyr,2}2(1 - X_2)\left(-\ln(1 - X_2)\right)^{0.5} + 0.134K(T)_{chlor.}(1 - X_2)^2 \quad [6.4]$$

Reaction Step 3:

$$\frac{dX}{dt}_3 = 0.095K(T)_{ank.2}2(1-X_3)^{0.5} + 0.189K(T)_{calc.}2(1-X_3)^{0.5} + 0.716K(T)_{dolo.}2(1-X_3)^{0.5} \quad [6.5]$$

In addition to the gas-solid reactions, based on Section 6.3.1.2, the solid-solid reactions can be included in this model. In this case, the decomposition of minerals is not only estimated based on kinetics but also based on the population analysis of contacts between minerals that can be obtained through QEMSCAN analysis. Consequently, the equation to estimate the decomposition of monazite will be in the form of Equation 6.6.

$$\frac{dX}{dt}_{mon.} = \overline{g_{mon}}\left(1 - L_{1,mon} - L_{2,mon}\right)K(T)_{mon.}\frac{3}{2((1-X_3)^{-1/3}-1)} \quad [6.6]$$

Where $\overline{g_{mon}}$ is the average grade of monazite in the ore in a particular particle size range, $L_{1,\,mon}$ is the mass fraction of monazite that is free or liberated, and $L_{2,mon}$ is the mass fraction of monazite associated with non-carbonatite minerals. The factor $\left(1 - L_{1,mon} - L_{2,mon}\right)$ represents the fraction of monazite associated to carbonate minerals, and thus able to react in the form of Reaction 6.6, for particles this cut size (below 20 µm) the factor is of 0.265.

All kinetic parameters related to Equations 6.3 to 6.6 can be found in Section 6.3.2 of this article.

Using the studied reaction rate equations and mechanism, the model for the calcination of rare earth bearing ore was developed. Figure 6.5 illustrated the agreement between the model and the experimental calcination of the ore. A slight deviation can be observed between 550 and 600 ºC corresponding to the transition between the reaction steps 2 and 3, which overlap. This model is able to accurately predict the mass loss of the sample at any given temperature and could also be used to predict the production of rare earth oxides (Figure 6.5c). For particles smaller than 20µm, rare earth oxides were mainly produced by the decomposition of bastnäsite, whereas monazite remained mostly unchanged due to its liberation and lack of contact with carbonate minerals that would produce calcium oxide allowing Reaction 6.6 to take place. Accordingly, the production of rare earth oxide was limited.

An advantage of developing this type of model is that it could be reused and adapted to study the calcination of an ore with different composition just by knowing the concentration of each mineral (Section 6.3.5).

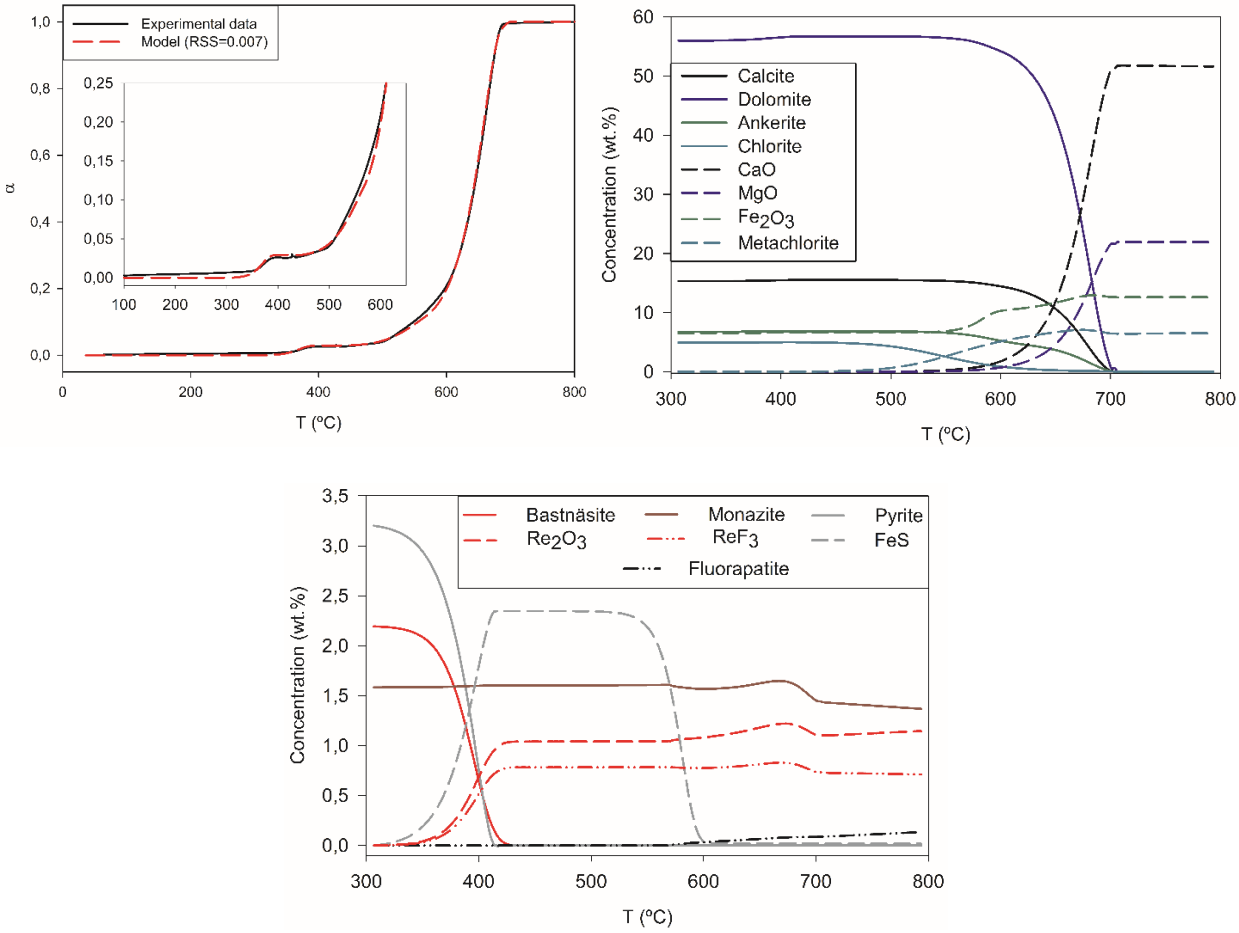

Figure 6.5 Reaction model for the calcination of a rare earth bearing ore with a grain size below 20µm

6.3.4 Particle size effect

The study of an ore extracted from a deposit is usually affected by factors as the mineral concentration or purity of the material, the operating conditions of the process and the particle size. The factors related to the deposit can be influenced by the grain of the ore and by the extraction location in the deposit itself.

The rate equation developed in this article takes into consideration possible changes in the mineral concentration of the ore, nonetheless, a change in the particle size could change the thermal behaviour. For this reason, a study of multiple fractions of particle size was developed in this

research. Figure 6.6 illustrates the effect of the particle size on the calcination of the ore. At relatively low temperatures (300-400 ºC), where bastnäsite and pyrite are decomposed, the particle size has any or minimal effect on the calcination. Yet, for the next steps of the calcination, the increasing on the particle size reduces the rate of calcination, and as a consequence, the decomposition of the ore occurs at a higher temperature (Figure 6.6).

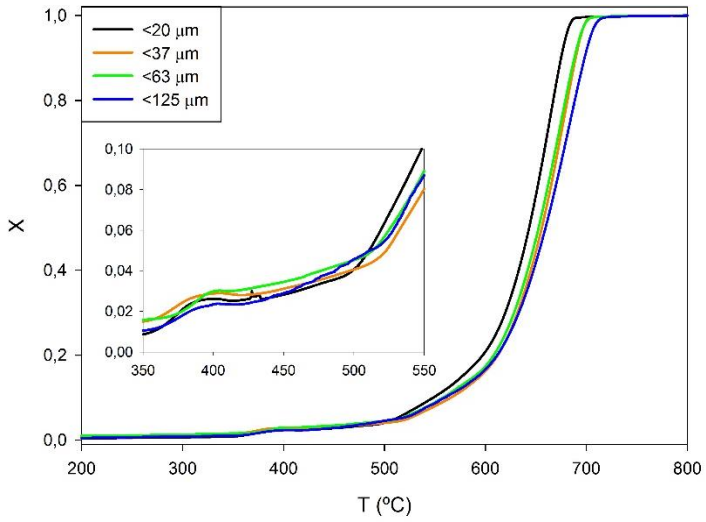

Figure 6.6 Calcination of rare earth bearing ore with different particle size (Hr=2ºC/min)

The model developed in Section 6.3.3 for particles below 20 µm was no longer applicable and needed correction in order to be adapted to bigger particles. The increasing of the particle size is often believed to affect the kinetic parameters of the decomposition, i.e. activation energy, pre-exponential factor and reaction mechanism [28-30]. In this regard, several studies were presented, and even an equation based on the surface energy of the components, and the particle's molar volume and diameter were developed [29, 30]. This coefficient has proven effective for nanoparticles and particles whose grain size was changed. In this research, despite increasing the particle size, the mineral's size forming the grain can be considered constant, and the particle size is increased by the combination of these minerals within the particle. Subsequently, the effect of the particle size on the global kinetic model can be estimated as a coefficient based on the decomposition mechanism and particle size characteristics, e.g. surface area. Similar coefficients were previously studied in the literature [31-33]. A similar procedure as the one developed by Escardino et al. 2008 has been adopted in this study [33].

When bigger particles were studied, i.e. particles below 37, 63 and 125 μm, their density and surface area decreased with the size. Table 6.7 presents the change of density and surface with the particle size. Such effect was particularly noticeable when the particles below 63 μm and below 125 μm were compared.

Table 6.7 Surface area measurement by BET of the different particle sizes

Sample	<20 (μm)	<37 (μm)	<63 (μm)	<125 (μm)	Certif. Material
$\overline{\boldsymbol{d_p}}$ (μm)	11.5	22.6	25.3	38.6	18.5
Surface area (m^2/g)	3.313	2.682	2.459	2.071	2.613
Density (g/cm^3)	3.325	3.193	3.180	3.162	3.030

To correct the rate model developed in Section 6.3.3, a coefficient, still assuming reaction control, was introduced into the rate decomposition model. Due to the complex rate decomposition equation obtained from the kinetic model study of the ore with a particle size below 20μm, some assumptions and simplifications were used to develop the coefficient. The latter was based on the main components of the ore, by extension on the main reaction mechanism as representative of the global kinetic model of Section 6.3.3, i.e. the contracting cylinder model, and on the decomposition of particles below 20 μm taken as the base case scenario, i.e. global kinetic model and particle size coefficient. The use of this mechanism led to a mathematical expression for the reaction rate (Equation 6.7).

$$r = k(T) \cdot 2 \cdot C_A^{\frac{1}{2}} - k' C_G^S = k(T) \cdot 2 \cdot [C_A^0(1-X)]^{\frac{1}{2}} - k' C_G^S \qquad [6.7]$$

Where r is the rate of decomposition of the mineral, in $mol/(m^2 \cdot min)$; C_G^S is the molar concentration of gas at the reaction interface, in mol/m^3; C_A^0 is the initial molar concentration of mineral in the particle mol/m^3; and k and k' are the constant rate of the calcination and reverse reaction respectively.

Herein, the gas reversibility was negligible due to the fast sweeping of CO_2 improved by the low amount of sample and the high inlet gas flowrate with which the test was operated.

Following the assumptions and procedure from Appendix E, Equation 6.8 was developed and represented the final decomposition rate.

$$\frac{dX}{dt}_{dpi} = \frac{\left(\sqrt{\rho_{dpi} M_{dpi}} S_{p,dpi} \overline{d_{p,i}}\right)}{\left(\sqrt{\rho M} S_p \bar{d}_p\right)_{20\mu m}} k_0(T) f(X) \quad [6.8]$$

Where d_{pi} is used to indicate a cut size, e.g. below 63μm; $\overline{d_{p,i}}$ is the average particle size of a cut size in m; ρ is the density of the cut size in g/m^3; M is the average molar mass of the ore, 197.7 g/mol; S_p is the surface area of the particle in m^2/g; and K(T) and f(X) represent respectively the Arrhenius equation in s^{-1} and the reaction mechanism.

The equation developed to describe the effect of the particle size on the decomposition of the ore appeared to fit the multiple rate decomposition of the ore (Figure 6.7). However, compared to the model used to describe particles with a size below 20μm, the error of the developed equation was higher. Multiple factors caused the increase in the error of the modeling, i.e. the coefficient developed assuming a general reaction mechanism as a simplification of the model based on individual minerals, the mineral association and possible encapsulation of some minerals, which might introduce a temperature gradient in bigger particles. Despite the possibility of estimating the mineral association by techniques such as QEMSCAN, its introduction into a model would not improve it since the mineral association for each test changes due to heterogeneity of the sample.

Finally, the rate production of rare earth oxides increases with the particle size. As was pointed out in Section 6.3.3, the production of rare earth oxides depended on the contact between rare earth minerals with carbonate minerals, especially calcite. The associated fraction of these minerals increased with the particle size, and 57.1 wt.% of monazite was associated with carbonate minerals for a particle size below 125 μm, compared to the 26.5 wt.% of particles below 20 μm.

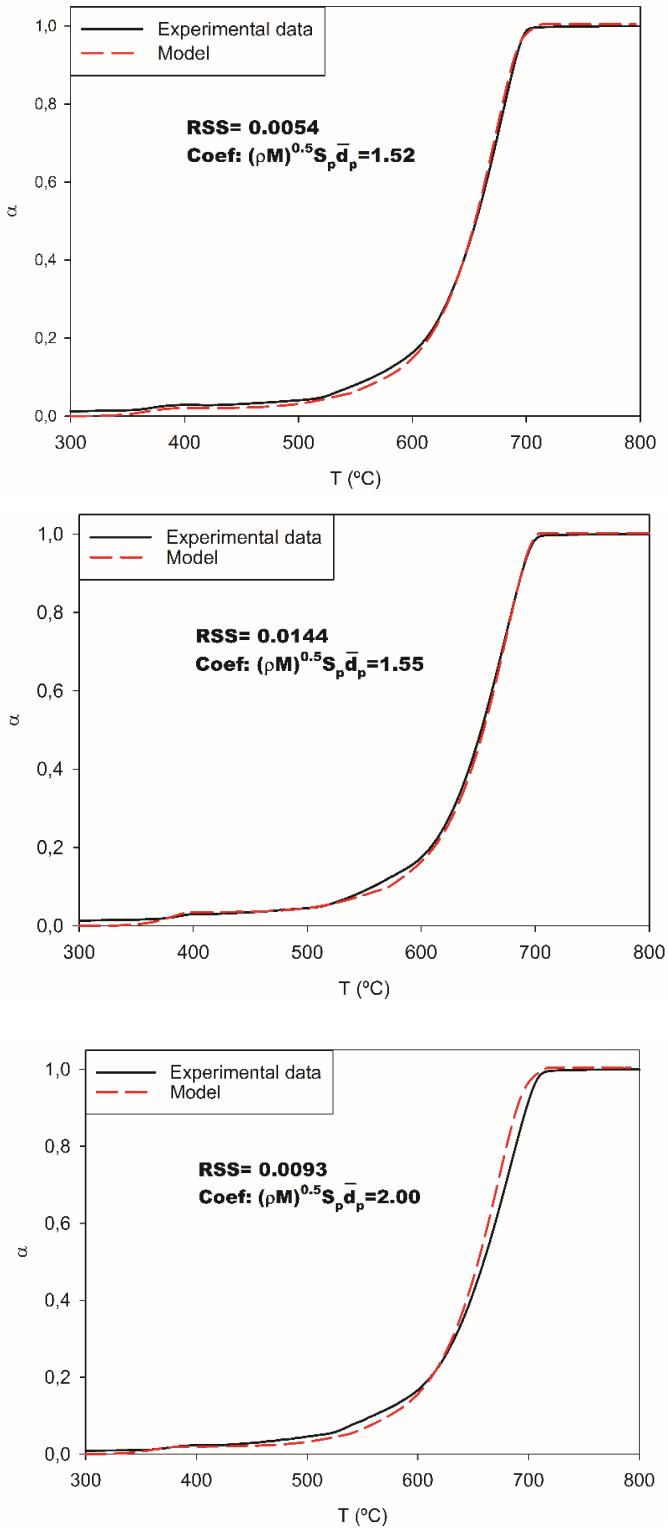

Figure 6.7 Validation of the reaction model for the different particle sizes: from left to right: <37 µm; <63 µm; <125 µm

6.3.5 Validation of the kinetic method

The model herein developed has proven to be effective in estimating the calcination of a carbonatite ore and estimate the production of rare earth oxides based on the decomposition of its bearing minerals, rather by gas-solid or by solid-solid reactions.

In order to approve the methodology and the modeling in this article, the model should also be consistent when applied to other ores, in particular containing the mineral studied, i.e. mainly carbonatite. Rare earth carbonatite deposits are distributed around the world and represent approximately half of the world's deposits, comprising Bayan Obo, one of the main rare earth deposit [1, 2, 34, 35].

Accordingly, the model was adapted and tested on a certified rare earth carbonatite ore with different concentrations from the one of Niobec (Table 6.1).The calcination of the certified material, represented in Figure 6.8a, showed similar shape as the one of Niobec ore with the decomposition of minor minerals, e.g. bastnäsite and pyrite, decomposed at relatively low temperature (400 ºC). Then, the presence of siderite (13 wt.%) that decomposes at around 500 ºC, involved that the second reaction step of this ore was more extended than for Niobec. The last step corresponded to the calcination of other carbonates, e.g. calcite and dolomite.

Despite a higher error compared to the model applied on the Niobec ore, the application of the kinetic model for the calcination of the ore was consistent with the experimental data (Figure 6.8b). The error could be reduced if more minerals kinetics, in accordance with the modal mineralogy of the ore, were introduced to the model

Unfortunately, the lack of data regarding the mineral associated with the rare earth bearing mineral of this ore, e.g. bastnäsite, monazite and apatite-REE, prevented the estimation of the rare earth oxide production as presented for the Niobec ore in Figure 6.5b.

a) b)

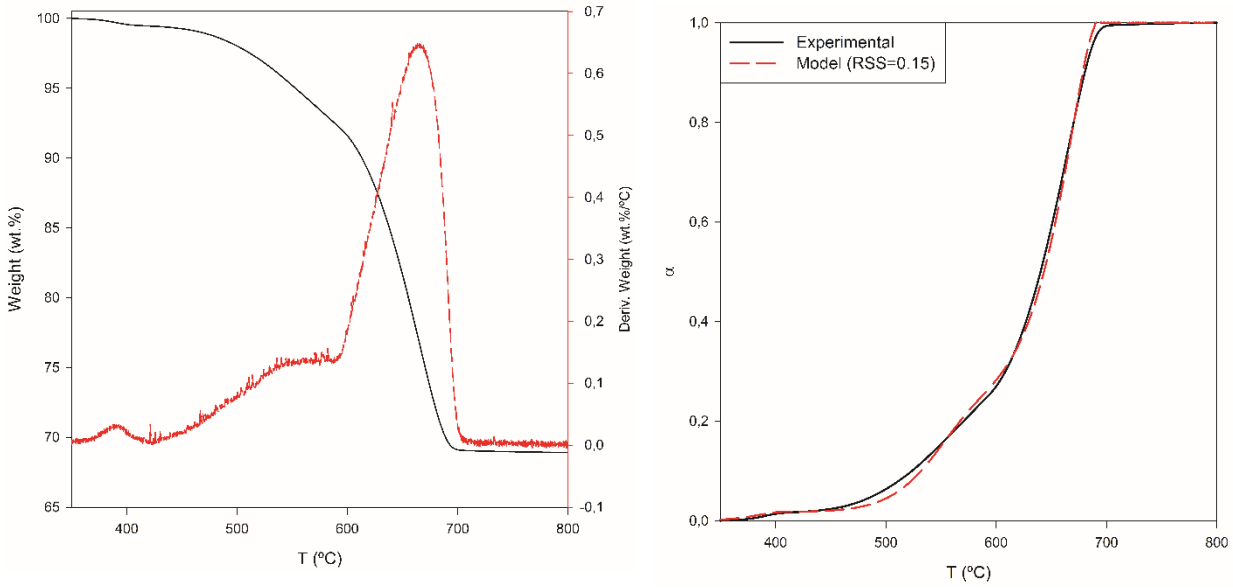

Figure 6.8 Reference rare earth sample: a- Thermogram; b- Validation of the kinetic model

6.4 Conclusions

The calcination of a rare earth carbonatite bearing ore led to a decomposition comprised of three steps, where the last step related to carbonatite gangue minerals (ankerite, calcite and dolomite) was predominant. During the calcination, rare earth oxides were produced by the decomposition of bastnäsite at around 400 ºC and the decomposition of monazite by its interaction with calcium oxide at higher temperatures (700 ºC). The latter is susceptible to its association with the appropriate mineral. QEMSCAN analysis was an important tool to evaluate the mineral association parameters.

Based on the decomposition mechanism of the ore and the calcination kinetics of its minerals, a global kinetic model was developed to describe the gas-solid and the solid-solid reactions in the course of the calcination. The model was first developed to evaluate the decomposition of a fine ore (20 μm), where minerals are mainly liberated or free. It was then adapted to bigger particles based on a coefficient supported by the physical properties of each cut size, e.g. surface area and

density. Along with the estimation of the mass loss or calcination, the model can be used to predict the production of rare earth oxides within an ore. The model's consistency was validated a different rare earth carbonatite deposit from Canada.

There is field to improve the methodology and modeling herein developed, since many minerals kinetics can be studied and implemented into a global model.

6.5 Acknowledgements

This work is part of a grant by Natural Science and Engineering Research Council of Canada (NSERC/CRD) and Niobec, a company in Province of Quebec of Canada. Authors would like to sincerely acknowledge the private mineral collector Eloy Joaquín Carrillo García for supplying hard rock stones of most of the minerals.

6.6 References

1. Gupta, C.K. and N. Krishnamurthy, *Extractive Metallurgy of Rare Earths*. 2004: CRC Press.
2. Simandl, G.J., *Geology and economic sifnificance of current and future rare earth element sources*, in *51st Annual Conference of Metallurgists* J.R. Goode, G.A. Moldoveanu, and M.S. Rayat, Editors. 2012: Niagara Falls.
3. Zhang, J. and C. Edwards, *A Review of Rare Earth Mineral Processing Technology*, in *44th Annual Canadian Mineral Processors Operators Conference*. 2012: Ottawa, Ontario, Canada.
4. Chen, L., et al., *Rare earth containing catalysts for selective catalytic reduction of NOx with ammonia: A Review.* Journal of Rare Earths, 2014. **32**(10): p. 907-917.
5. Gupta, C.K. and N. Krishnamurthy, *Extractive Metallurgy of Rare-Earths.* International Materials Reviews, 1992. **37**(5): p. 197-248.
6. Habashi, F., *Extractive metallurgy of rare earths.* Canadian Metallurgical Quarterly, 2013. **52**(3): p. 224-233.
7. Brumme, A., *Market analysis of rare earth elements*, in *Wind Energy Deployment and the Relevance of the Rare Earths: An Economic Analysis*, S. Gabler, Editor. 2014. p. 17-48.

8. Jordens, A., Y.P. Cheng, and K.E. Waters, *A review of the beneficiation of rare earth element bearing minerals.* Minerals Engineering, 2013. **41**: p. 97-114.

9. Feng, X.L., et al., *Kinetics of rare earth leaching from roasted ore of bastnaesite with sulfuric acid.* Transactions of Nonferrous Metals Society of China, 2013. **23**(3): p. 849-854.

10. Clarke, F.W. and H.S. Washington, *The composition of the earth's crust*. 1924, United States Geological Survey (USGS): Washington.

11. Criado, J.M. and A. Ortega, *A study of the influence of particle size on the thermal decomposition of CaCO3 by means of constant rate thermal analysis.* Thermochimica Acta, 1992. **195**: p. 163-167.

12. Földvári, M., *Handbook of thermogravimetric system of minerals and its use in geological practice*, ed. G.I.o. Hungary. Vol. 213. 2011, Budapest.

13. Hikichi, Y., T. Ota, and T. Hattori, *Thermal mechanical and chemical properties of sintered monazite (La, Ce, Nd or Sm).* Mineralogical Journal, 1997. **19**(3): p. 123-130.

14. Reller, A., et al., *Thermochemical Reactivity of Metal Carbonates.* Chimia, 1991. **45**: p. 262-266.

15. Guentner, J., et al., *Recovery of rare earth elements from complex raw materials by Outotec's Solutions*, in *IMPC 2016: XXVIII International Mineral Processing Congress Proceedings*. 2016: Quebec City.

16. Hajiani, P., *Significant reduction in hydrochloric acid consumption in rare earth extraction from ferrocarbonatite (Montviel Project)*, in *IMPC 2016: XXVIII International Mineral Processing Congress Proceedings*. 2016: Quebec City.

17. Xing, P.F., et al., *High temperature dephosphorization behavior of monazite concentrate with charred coal.* Transactions of Nonferrous Metals Society of China, 2010. **20**(12): p. 2392-2396.

18. Yuan, S., et al., *Roasting decomposition of mixed rare earth tailings by CaO in reducing atmosphere.* Rare Metals, 2014.

19. Britton, H.T.S., S.J. Gregg, and G.W. Winsor, *The calcination of dolomite. Part II.- The thermal decomposition of dolomite.* Trans. Faraday Soc., 1952. **48**: p. 63-69.

20. Britton, H.T.S., S.J. Gregg, and G.W. Winsor, *The calcination of dolomite. Part I.—The kinetics of the thermal decomposition of calcite and of magnesite.* Trans. Faraday Soc., 1952.

21. Kulp, J.L., P. Kent, and P.F. Kerr, *Thermal study of the Ca-Mg-Fe carbonate minerals.* Journal of the Mineralogical Society of America, 1951. **36**: p. 643-670.

22. Maciejewski, M., *Computational aspects of kinetic analysis. Part B: The ICTAC Kinetics Project — the decomposition kinetics of calcium carbonate revisited, or some tips on survival in the kinetic minefield.* Thermochimica Acta, 2000. **355**: p. 145-154.

23. Xiang, J., et al., *Thermal decomposition behaviour of natural bastnasite crystal in calcination.* Transaction of NFsoc, 1994. **4**(4): p. 34-38.

24. Hikichi, Y. and T. Nomura, *Melting Temperatures of Monazite and Xenotime.* Journal of the American Ceramic Society, 1987. **70**(10): p. C-252-C-253.

25. Hikichi, Y., K.-i. Hukuo, and J. Shiokawa, *Solid State Reactions between Rare Earth Orthophosphate and Oxide.* Bulletin of the Chemical Society of Japan, 1980. **53**(5): p. 1455-1456.

26. Kumari, A., et al., *Thermal treatment for the separation of phosphate and recovery of rare earth metals (REMs) from Korean monazite.* Journal of Industrial and Engineering Chemistry, 2015. **21**: p. 696-703.

27. Xue, B., et al., *Kinetics of Mixed Rare Earths Minerals Decomposed by CaO with NaCl-CaCl2 Melting Salt.* Journal of Rare Earths, 2010. **28**(Spec. Issue): p. 86.

28. Abdul Mujeeb, V.M., et al., *The effect of particle size on the thermal decomposition kinetics of potassium bromate.* Journal of Thermal Analysis and Calorimetry, 2011. **108**(3): p. 1171-1182.

29. Fu, Q.-S., et al., *Study on the Size-Dependent Oxidation Reaction Kinetics of Nanosized Zinc Sulfide.* Journal of Nanomaterials, 2014. **2014**: p. 1-8.

30. Xue, Y., X. Wang, and Z. Cui, *The effects of particle size on the kinetic parameters in the reaction of nano-NiO with sodium bisulfate solution.* Progress in Reaction Kinetics and Mechanism, 2011. **36**(4): p. 329-341.

31. Borgwardt, R.H., *Calcination kinetics and surface area of dispersed limestone particles.* AIChE Journal, 1985. **31**(1): p. 103-111.

32. Borgwardt, R.H. and K.R. Bruce, *Effect of specific surface area on the reactivity of CaO with SO2.* AIChE Journal, 1986. **32**(2): p. 239-246.

33. Escardino, A., J. Garcia-Ten, and C. Feliu, *Kinetic study of calcite particle (powder) thermal decomposition: Part I.* Journal of the European Ceramic Society, 2008. **28**(16): p. 3011-3020.

34. Weng, Z., et al., *A Detailed Assessment of Global Rare Earth Element Resources: Opportunities and Challenges.* Economic Geology, 2015. **110**(8): p. 1925-1952.

35. Weng, Z.H., et al., *Assessing rare earth element mineral deposit types and links to environmental impacts.* Applied Earth Science, 2013. **122**(2): p. 83-96.

36. Carrillo Garcia, A., *Thermal decomposition of a rare earth ore*, in *Chemical Engineering*. 2019, Polytechnique Montreal: Montreal.

37. Khawam, A. and D.R. Flanagan, *Solid-state kinetic models: Basics and mathematical fundamentals.* Journal of Physical Chemistry B, 2006. **110**(35): p. 17315-17328.

38. Vyazovkin, S., et al., *ICTAC Kinetics Committee recommendations for collecting experimental thermal analysis data for kinetic computations.* Thermochimica Acta, 2014. **590**: p. 1-23.

39. Cheng, H., et al., *Application of TG-FTIR to study SO2 evolved during the thermal decomposition of coal-derived pyrite.* Thermochimica Acta, 2013. **555**: p. 1-6.

40. Hong, Y. and B. Fegley, *The kinetics and mechanism of pyrite thermal decomposition.* Berichte der Bunsengesellschaft für physikalische Chemie, 1997. **101**(12): p. 1870-1881.

41. Hu, G., et al., *Decomposition and oxidation of pyrite.* Progress in Energy and Combustion Science, 2006. **32**(3): p. 295-314.

42. Paulik, J., F. Paulik, and M. Arnold, *Simultaneous TG, DTG, DTA and EGA Technique for the Determination of Carbonate, Sulphate, Pyrite and Organic Material in Minerals, Soils and Rocks.* Journal of Thermal Analysis, 1982. **25**: p. 327-340.

43. Srinivasachar, S. and A.A. Boni, *A Kinetic-Model for Pyrite Transformations in a Combustion Environment.* Fuel, 1989. **68**(7): p. 829-836.

44. Trittschack, R. and B. Grobety, *Dehydroxylation kinetics of lizardite.* European Journal of Mineralogy, 2012. **24**(1): p. 47-57.

45. Villieras, F., et al., *Development of microporosity in clinochlore upon heating.* Clays and Clay Minerals, 1994. **42**(6): p. 679-699.

46. Odogorova, L.P., et al., *Natural Mg-Fe clinochlores Enthalpies of formation and dehydroxylation derived from calorimetric study.* American Mineralogist, 2016. **101**: p. 1431-1437.

47. Redfern, S.A.T., *The kinetics of dehydroxylation of kaolinite.* Clay Minerals, 1987. **22**: p. 447-456.

48. Levenspiel, O., *The Chemical Reactor Omnibook*. 1989.

49. Hyatt, E.P., I.B. Cutler, and M.E. Wadsworth, *Calcium Carbonate Decomposition in Carbon Dioxide Atmosphere.* Journal of the American Ceramic Society, 1958. **41**(2): p. 70-74.

CHAPTER 7 ARTICLE 3: PRODUCTION OF RARE EARTH OXIDES FROM RAW ORE IN FLUIDIZED BED REACTOR

Adrián Carrillo García, Mohammad Latifi, Said Samih and Jamal Chaouki

Process Development Advanced Research Lab (PEARL), Chemical Engineering Department, Polytechnique Montreal

C.P. 6079, Succ. Centre-ville, Montreal, Quebec, Canada, H3C 3A7

(Journal of Industrial and Engineering Chemistry, submission date: September 28th 2019)

ABSTRACT

This study deals with the calcination of a rare earth bearing ore to produce rare earth oxides in a fluidized bed reactor, with the aim of demonstrating the advantage of calcining bigger particles to decompose complex minerals such as monazite by its mineral association within a particle. Rare earth oxides were produced by the decomposition of its bearing minerals, bastnäsite and monazite along with the gangues. During the calcination, bastnäsite decomposed at relatively low temperature while monazite reacted with the associated gangue (CaO) at high temperature. The formation of cracks, evaluated by BET and SEM analysis, allowed the particle's degassing while the size remained constant, thus describing a crackling core behavior.

The association of monazite to calcite for bigger particles (-60 mesh) allowed its decomposition to produce rare earth oxides with a monazite conversion of 50 %. Also, an extraction process comprised of calcination and mild acid leaching enriched the rare earth oxides in the ore by 3.34 and improved leaching efficiency of the gangues compared to smaller size (enrichment ration of 2.35). Using bigger particle sizes in the upstream process of a mining industry, i.e. comminution, can also reduce the energy consumption.

GRAPHICAL ABSTRACT

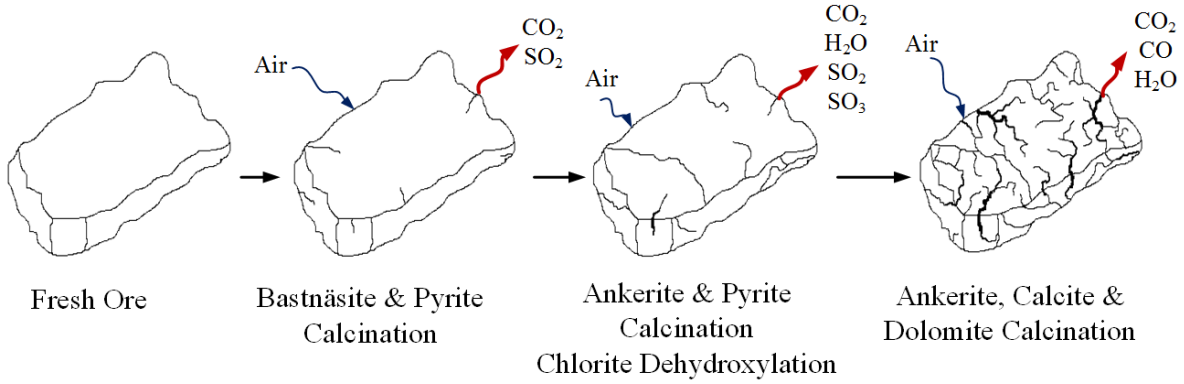

KEYWORDS

Rare Earth, Calcination, Fluidized bed, Cracking, Lixiviation, Monazite association

7.1 Introduction

Rare earth elements (REE) are metals represented by the lanthanide group, scandium and yttrium [1]. The increasing demand of REEs driven by their applications makes them a critical material in the future to come [1-3]. Some important applications are in the clean energy, e.g. neodymium in the permanent magnets [4, 5], and electronic device industry.

These elements are easily found on earth in the form of minerals. From the many forms of minerals known to contain REEs, i.e. carbonatite, halide, oxide, phosphate and silicate, bastnäsite ($(REE)FCO_3$), monazite and xenotime ($(REE)ThPO_4$) are the three main REE bearing minerals from which extraction of REE is viable with a REE concentration between 50 to 75% [1, 6, 7]. These minerals are often found in large deposits with carbonatite and alkaline gangues [1, 8-10].

Their conventional production process starting from the deposits is comprised of a complex array of processes notably in four main steps: 1) mining and milling, 2) physical beneficiation, 3) hydrometallurgy and 4) individual separation of REE [1, 11, 12]. While the first step focuses on reduction of the rocks to the desired size of the ore, physical beneficiation increases the rare earth concentration without modifying the structure of its bearing minerals [1, 6]. Once an elevated concentration of minerals is reached, the minerals of the concentrate undergo roasting and hydrometallurgical steps to transform the rare earth bearing minerals to a more leachable or treatable structure, for instance, in the form of sulfates or chlorides. The objective of this thermochemical processing is to produce a high-grade mixture of rare earth elements (e.g. above 90%), for example, in the form of either rare earth oxides or rare earth chlorides (depending on the process economy and market needs).

The thermochemical processing is known for using severe conditions to treat the ore, especially roasting at a high temperature (e.g. above 200 ºC with sulfuric acid) with a high acid to ore ratio [1, 11-14]. It should be denoted that rare earth elements are usually adjacent to metals such as iron, calcium, magnesium, manganese, radioactive elements of thorium and uranium, etc that must be separated subsequent to the roasting step. Therefore, we would face a complex array of hydrometallurgical steps such as leaching, precipitation, filtration, chemical oxidation, and calcination where a considerable mass and type of the reagents are required.

An alternative to the hydrometallurgical step is the pyrometallurgy or calcination. This process is a technology widely used in the mineral industry and aims to produce metal oxide [15-17]. The production of oxides renders the metal more susceptible to leaching than the mineral form. Studies regarding the calcination of rare earths ore focus on the treatment of concentrated ores minerals, and are combined with mild conditions of subsequent hydrometallurgical steps for impurities removal [1, 18-20].

The concern with the rare earth bearing minerals is the difficulty to produce rare earth oxides through calcination due to their mineral form. Calcination is particularly not effective for bastnäsite and monazite. Despite its calcination at relatively low temperature, 400 ºC, bastnäsite produces two rare earths phases: rare earth oxide and rare earth fluoride [21]. On the other hand, monazite does not decompose standalone at a high temperature while it has a melting temperature around 2000 ºC [22, 23]. To overcome these problematics, some authors have shown that mixing these minerals with other reactants (i.e. fluxes) might reduce the calcination temperature, for instance by forming eutectic, and allow the decomposition of the phosphate minerals to from rare earth oxides [20, 24-27].

Authors have developed a process for direct production of rare earth oxides from a raw ore that contains rare earth bearing minerals of bastnäsite and monazite along with the gangues mainly being carbonates such as calcite, dolomite, and ankerite. This process is to overcome serious issues and complexity of the physical beneficiation step (i.e. concentrate production), and of the minerals cracking step (i.e. liberation of elements by acid/alkali baking) that are quite common in the conventional REE production processes.

In this new process, the raw ore directly undergoes thermal cracking with air in newly developed micro fluidized bed reactors to produce rare earth oxides [28]. The selection of the reactor, i.e. fluidized bed, is the core of the process, and compared to other reactors such as rotary kilns [29, 30], fluidized beds ensure a proper mixing of fine particles and heat transfer, which are essential to fulfill the calcination for endothermic reactions as it is the case of minerals [31]. In addition, due to gas hold up, e.g. CO_2, in some of the reactors, calcination might end up with longer reaction times, poor product quality due to incomplete oxidation, reverse reactions and agglomeration [29,

30, 32]. Thus, one of the objectives of this study is to evaluate the performance of the calcination of rare earth bearing ores in fluidized bed reactor to produce rare earth oxides.

When performing calcination in fluidized beds, the release of gases such as CO_2 for carbonate minerals and the collision of the particles due to the intense mixing in the reactor tend to crack the particles [33, 34]. This drawback can induce a higher entrainment and reduce the calcination performance. To evaluate the attrition of the particles, authors deepen in the morphological and particle evolution during calcination.

On the other hand, the morphological change of particles can be useful in the subsequent leaching step. The presence of cracks or finer particles may improve the selective separation of rare earth elements by rendering the core of the particle available to acid. Authors present a combined calcination and leaching study on various particle sizes to show the importance of the selection of a convenient size cut for the calcination process. In it, the metal oxide production during calcination without the addition of any flux and the leaching selectivity will be evaluated.

Finally, the rare earth oxide production by the calcination in a fluidized bed reactor of a rare earth bearing ore will be performed. The aim of the study is to evaluate the performance of the calcination based on the decomposition, the particle's morphology and the subsequent rare earth extraction process.

7.2 Experimental

7.2.1 REE ore

Niobec Inc. provided the ore from its deposit in Saguenay, Canada. The mineral composition of the ore, represented in Table 7.1, was measured by QEMSCAN, at XPS Expert Solutions. In the ore, carbonate minerals are the main representative with approximately 76.9 wt.% of the ore; while rare earth minerals are 3.39 wt.%. QEMSCAN also allowed to evaluate the mineral association and the liberation size of minerals within the ore. Such data may be used to evaluate the efficiency of physical beneficiation processes, or as it was used in this research to know the maximal theoretic conversion that a mineral could undergo through solid-solid interaction.

Table 7.1 Mineral composition of Niobec ore from QEMSCAN analysis

Mineral	Dolomite	Calcite	Ankerite	Bastnäsite	Monazite	Chlorite	Pyrite	Other
modal composition, wt.%	50	13.2	13.7	1.96	1.43	4.43	2.86	12.42

7.2.2 Calcination apparatus and procedure

We applied the calcination of the Niobec ore in a fluidized bed thermogravimetric analyzer (FB-TGA) developed at Polytechnique Montreal [35]. This reactor allows the accurate measure of the mass loss during the calcination in a fluidized bed reactor. The equipment consists of a quartz reactor with a 1'' inner diameter and 6'' length heated by a vertically assembled tubular furnace, while the mass of the fluidized bed is measured by a load cell placed at the bottom of the reactor [35]. During calcination, the outlet gas was measured by a MKS 2030 MultiGas FTIR 2 and a Varian 4900 Micro Gas Chromatography (GC).

We carried out the tests with the ore of a particle size between 63 and 125 μm and a density of 3110 $kg \cdot m^{-3}$. That is, the ore represented Geldart's group B particles with a minimum fluidization velocity (u_{mf}) at ambient conditions of 0.82 cm/s. The u_{mf} was estimated by measuring the change of the total pressure drop across the bed at multiple gas velocities.

The calcination was performed under air atmosphere with a constant heating rate of 20 ºC/min from ambient temperature to 800 ºC, at which the sample roasting continued until the recording showed the mass was stabilized indicating the end of the reaction. The gas flowrate was changed during the test to ensure the bed was close to minimum fluidization velocity at any given temperature. By operating close to minimum fluidization velocity, we could ensure the fluidization with small bubble size and reduce that way the effect of hydrodynamics during calcination.

7.2.3 FB-TGA and analysis of particles morphology

The change in the particle morphology and size upon treatment in a fluidized bed reactor was studied in the course of calcination in FB-TGA setup. To do so, the roasting test was stopped and cooled down at different temperatures from 400 ºC to 800 ºC, approximately at every 50 ºC increment. Each calcined product was then characterized: the particle size and its distribution were analyzed with a Master Sizer 3000 from Malvern Instruments, while a pycnometer AccuPyc II 1340 from Micromeritics was used for the density. A Hitachi TM3030Plus scanning electron microscopy was used to analyze the particle's morphology. We employed a Brunauer–Emmett–Teller (AX1C-MP-LP) from Quantachrome Instruments to estimate the surface area by the adsorption/desorption of nitrogen, and the pores in terms of type and volume.

7.2.4 Fluidized bed reactor model

All the experiments carried out in the micro fluidized bed reactors were performed at conditions close to minimum fluidization regime. At those conditions, gas bubbles are relatively small, and effect of hydrodynamics are reduced. The mixing of the solid particles in the dense bed induce the gas mixing, so as simplification, the reactor can be modeled as a continuous stirred tank reactor for the dense bed and as plug-flow reactor for the freeboard region [35-38]. Mass balance equation will thus change based on the zone of reactor:

- Dense or fluidized bed zone:

The mass balance of each gas can be written as in equation 7.1 [39]:

$$\frac{dC_{i,g}\,V}{dt} = \dot{F}_{i,in} - \dot{F}_{i,out} + \sum_{g-s} \vartheta_{ij} r_j V \qquad (7.1)$$

Where $C_{i,g}$ is the concentration of gas i (mol/m^3), V is the volume of the fluidized bed zone (m^3), ϑ_{ij} is the stoichiometric coefficient of gas i for the gas-solid reaction j, r_j is the rate of reaction of mineral j (mol/(m^3·s)), and $\dot{F}_{i,in}$ and $\dot{F}_{i,out}$ respectively are the inlet and outlet molar flow rates of the gas i (mol/s). The reaction rate for the decomposition of each mineral are represented in Table 7.2.

The mass balance of solid can be represented as equation 7.2 [39]:

$$\frac{dw_s}{dt} = R_s \tag{7.2}$$

Where w_s is the solid that has reacted in the reactor (kg), R_s is the total reaction rate of solid (kg/s). On that regard, the total reaction rate of solid was presented in a previous work [40].

- Freeboard zone:

In the freeboard, the mass balance of each gas can be written as in equation 7.3 [39]:

$$\frac{dC_{i,g}}{dt} = \sum_{g-g} \vartheta_{im} r_m - u_g \frac{dC_i}{dz} \tag{7.3}$$

Where the first term represents the gas homogeneous reactions (negligible in this work), u_g is the gas velocity (m/s) and z the height of the reactor (m). The second term represents the variation of gas concentration along the freeboard and depends on the gas-solid reaction taking place in the freeboard, as shown in equation 7.4:

$$u_g \frac{dC_i}{dz} = \xi_{g-s} \sum_{g-s} \vartheta_{i,j} r_j \tag{7.4}$$

$$\xi_{g-s} = 1 - 0.75 \left(\frac{C_S}{C_{S,Hb}} \right)^{0,4} \tag{7.5}$$

$$\frac{dC_s}{dz} = -a\, C_s \tag{7.6}$$

$$a = 315 \frac{\overline{d_p^{0,64}}}{U_g} \tag{7.7}$$

Where ξ_{g-s} is the gas-solid contact efficiency (equation 7.5), C_S and $C_{S,Hb}$ are the solid concentration at height z of the freeboard (kg/m^3) and at the top of the dense bed respectively, and a is the decay factor (equation 7.7) [41]. As solid concentration (equation 7.6) decay along the freeboard, gas-solid reaction's efficiency does too. In this case, as the particle size is small ($\overline{d_p} < 40\ \mu m$) and the gas velocity is close to minimum fluidization velocity, the decay factor is high (approximately 53), so that the concentration of solids in the freeboard can be considered negligible.

- Reaction rates:

Minerals reaction rates were estimated in a previous work [40] and are presented in Table 7.2.

7.2.5 Solid-solid interaction during calcination in an IHFBR

It is important to select a proper size distribution of particles to operate a fluidized bed reactor in an industrial scale in favor of maximum conversion of the REE bearing minerals to REO with a fast kinetic, minimum loss of particles in the reactor outlet, and maximum recovery of REE in the downstream separation steps. For this purpose, the ore was sieved to particle sizes below 20µm, 63 µm, 125 µm and 250 µm; respectively in terms of mesh size, - 635, - 230, - 120 and - 60.

The calcination tests for each particle size cut were carried out in an induction heating fluidized bed reactor (IHFBR) [42, 43] where the evolved gas stream was analyzed.

Subsequent to each test, the leftover powders in the reactor (calcined product) was analyzed by LECO to specify its carbon content. Its particle size distribution was also determined by a master sizer Malvern 3000 to ensure the consistency with the procedure described in Section 7.2.3. The mineralogy, i.e. REE oxide production and monazite decomposition, was performed by XRD and Rietveld method using a Bruker-AXS D8 DISCOVER diffractometer configured with a Cu-Kα radiation with XRD patterns recorded between a 2θ range of 20º to 90º.

7.2.6 Leaching of REE from the calcined powders

We applied acid leaching with a 0.1 M hydrochloric acid solution and a hydrochloric acid to solid ratio of 1:1 for 90 min at ambient temperature to the solid product of calcination. The low concentrated solution was able to dissolve the calcium and magnesium oxide while leaving the rare earths in the cake. We specified the leaching performance by measuring the enrichment ratio and recovery of REE in the filtered cake, and by measuring the recovery of the impurities, e.g. calcium, iron, manganese and magnesium in the leachate (leach liquor). The solid product was characterized by Neutron Activation Analysis (NAA) [44], while the liquid product was analyzed by Inductively

coupled plasma spectroscopy (ICP-MS) from Perkine-Elmer NexION 300 at Polytechnique Montreal.

7.3 Results and discussion

7.3.1 Calcination and morphology evolution of a rare earth ore

Thermal studies are often performed in conventional thermogravimetric analyzers with a small mass of sample (e.g. 10 to 20 mg) to avoid any detrimental impact of heat or external mass transfer on the reaction kinetics [45, 46]. However, these studies cannot always be transposed or compared to industrial scale reactors, e.g. effect of hydrodynamics or heat and mass transfer resistances in the reactor [35].

Given that REE ores are heterogeneous in term of concentration of the constructive elements, including the Niobec ore, we applied and compared the calcination of the Niobec ore in both FB-TGA and a conventional TGA (TGA Q5000 from TA instruments) for a range of particles (63 to 125 µm). We also ran a test in the FB-TGA setup under a fixed bed operation regime as a background since some researchers consider TGAs as a fixed bed reactor (even though not necessarily a right term). The obtained thermograms are illustrated in Figure 7.1a.

When 10 mg of ore were calcined in a TGA (WHSV of 294 h^{-1}), approximately 38.6 wt.% of the mass was lost in the form of gases and total decomposition of the sample took place when 800 ºC was reached. On the other hand, when calcining 10 g of sample in a fixed bed regime (WHSV= 0.74 h^{-1}), the sample endured a long calcination process at 800 ºC, i.e. 4h, to achieve full conversion (Figure 7.1a). The trend of mass loss observed in the fixed bed regime was expected due to the detrimental presence of heat transfer and diffusion of the gaseous products to the reaction bulk and from the bulk to the reactor outlet. An important conclusion of this observation is the necessity of a mixed flow regime in between the gas and the solid phases of the calcination of the ore particles.

Fluidized bed reactors are known to improve the gas-solid contact thus favoring the calcination reaction [31]. Even if, the hydrodynamic characteristics of the FB-TGA (due to its low U/U_{mf} ratio) would be far from the true behavior in large scale fluidized bed reactors in terms of superficial gas

velocity (i.e. fluidization regime), rate of particles agglomeration or attrition, wall effect, etc, we employed the FB-TGA as a representative of fluidized bed reactors. This reactor is definitely suitable to measure the mass variation and study the physical change of the particles in the course of calcination of Niobec ore under presence of hydrodynamic forces in a gas-solid fluidized bed reactor.

The use of the FBTGA to calcine 10 g (WHSV= 5.5 h^{-1}) of ore avoided the limitations of a fixed bed regime and presented a similar mass loss of decomposition as the TGA test for 10 mg (Figure 7.1a), the final mass loss difference between them could be adjudicated to small variations in the feed composition. Nonetheless, the use of the FB-TGA changed the thermogram of the process. Using a fluidized bed, the air-solid contact and the temperature distribution are improved compared to the conventional TGA, where the hydrodynamics effect of the reactor are negligible, and to the fixed bed reactor which is known to have heat transfer effect, inducing the calcination process to start earlier. Samih et al 2018 related this phenomenon to a reduction of the activation energy of the reactions in the fluidized reactor [39].

The calcination in the FB-TGA presented a limitation when using a higher amount of mass, 30 g (WHSV= 1.9 h^{-1}) instead of 10 g (WHSV= 5.5 h^{-1}), due to the high amount of gas that was produced at elevated temperature (pertinent to the trends in Figure 7.1a) and the low elimination rate of this produced gas. At approximately 700 ºC, the CO_2 produced during the calcination indicated that the reaction rate of the rare earth bearing ore attained its maximum (Figure 7.1b). At this point, the amount of gas produced is too high compared to the volume of the reactor, thus limiting the outgassing of the reactor. This limitation was translated by a change in the thermogram and the need of a longer reaction to achieve full conversion. Therefore, other calcination studies performed in FB-TGA for this work were done with approximately 10 g of sample.

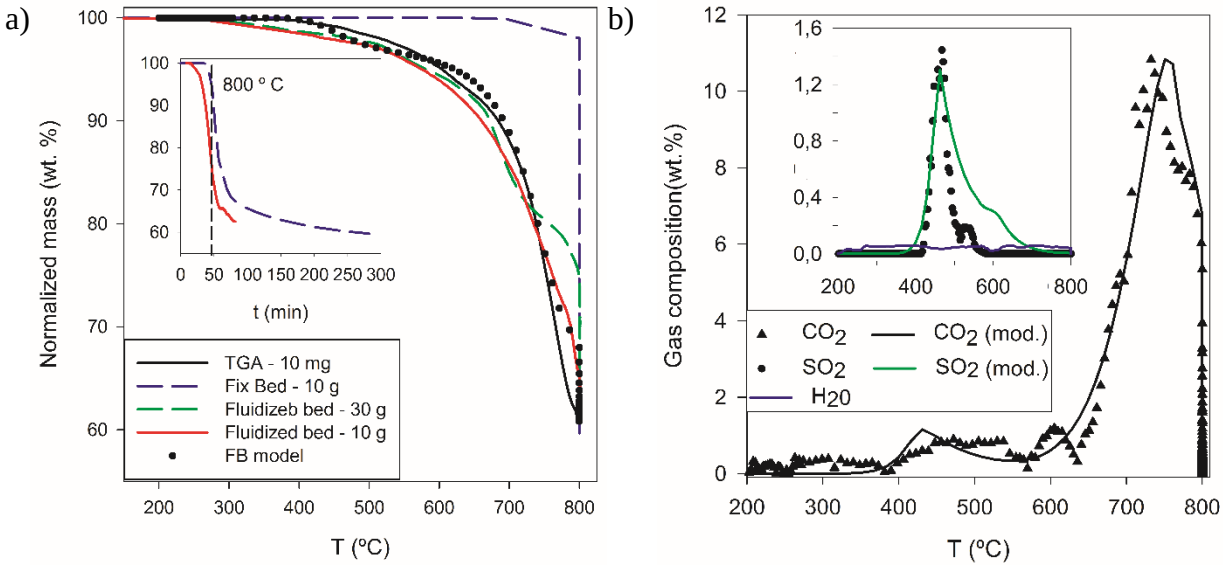

Figure 7.1 Calcination of a rare earth bearing ore in a fluidized bed TGA: a) Thermograms; b) Evolved gas analysis (experimental and model)

The combination of the evolved gas analysis of the FB-TGA calcination (Figure 7.1b) and the mineralogical study by XRD performed on the fresh ore and on the calcined samples in a fluidized bed reactor (FB-TGA) at various temperatures (Figure 7.2) revealed the ore's composition changes along a rise in temperature. A progressive conversion versus temperature of the REE bearing minerals and the adjacent gangues produced CO_2, SO_2 and H_2O, which were respectively related to the decomposition of carbonates, pyrite and chlorite minerals to the oxide form of the metals. Table 7.2 summarizes the main reactions occurring during the calcination.

The calcination started approximately at 400 ºC with the decomposition of bastnäsite [21] and pyrite [47-49] that ended at 550 ºC (Reactions 7.1 & 7.2, Table 7.2). Table 7.2 represents all reactions described in this manuscript. These reactions could be traced by the production of rare earth oxides and hematite detected by XRD measurements made at 600 ºC (Figure 7.2-b) and the detection of CO_2 and SO_2 by the GC/FTIR system at that temperature interval (Figure 7.1b). After drying of the free or bonded water, the production of water observed above 400 ºC was related to the dehydroxylation reaction of chlorite minerals, which as described in literature undergoes a complex decomposition process [50, 51]. As can be seen in Figure 7.1, the reactor model developed

for the calcination of the rare earth ore in micro fluidized reactor is in quite good agreement with the experimental data derived from the fluidized TGA, and justify the reaction steps by tracking the gases production. As some differences can be observed especially in the ore weight study, those are caused, as explained earlier by the reduction in a fluidized bed of the activation energy of minerals' decomposition which was not considered in this model [39].

The main decomposition reactions, i.e. calcite, dolomite, and ankerite (Reactions 7.3 to 7.5) occurring above 600 ºC, resulted in the high production of CO_2, and the detection of calcium and magnesium oxide by XRD (Figure 7.2-c & d).

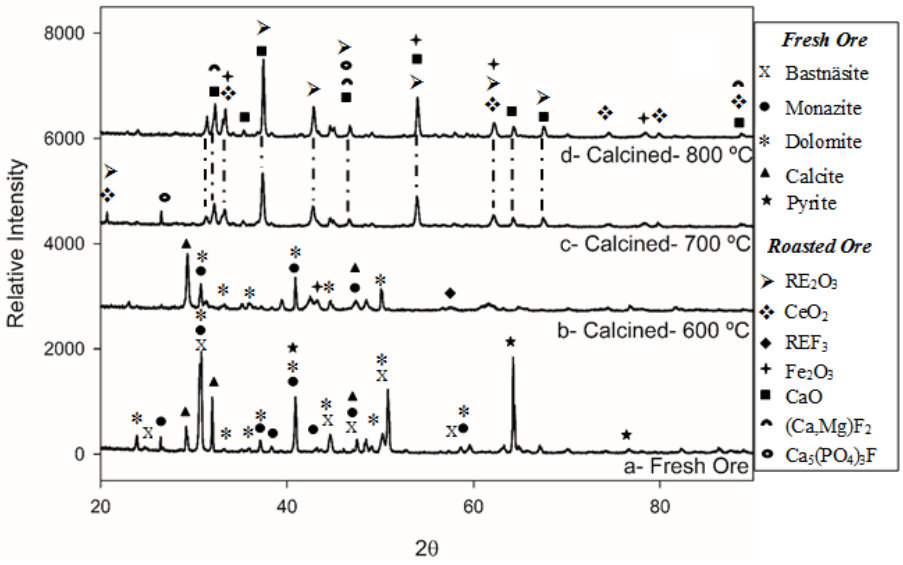

Figure 7.2 Diffractograms of a rare earth bearing ore (d_p 63 to 125 µm) during calcination

During calcination, the oxidative atmosphere of air induced a change of cerium's oxidative state from cerium III (Ce_2O_3) to IV (CeO_2) (Figure 7.2-d). Similar observation were made for the calcination of bastnäsite [21].

On the other hand, some minerals, e.g. quartz or barite, remained unaltered due to their high temperature resistance, while others, e.g. monazite, underwent a reaction with other solid forms produced during calcination (Reactions 7.6 & 7.7). In this case the reaction of monazite with the calcium oxide was possible due to the presence of both components within the grain, but similar interaction of monazite with other solid components have been studied in literature [23, 25, 52].

Table 7.2 Overall reaction of the individual minerals during calcination

Mineral	Reaction & Reaction rate (s^{-1})	
Bastnäsite	$3REFCO_3 \rightarrow RE_2O_3 + REF_3 + 3CO_2$	(7.1)
	$r_{bast} = 5.28 \cdot 10^{14} exp\left(-\frac{203300}{R\,T}\right)(1-\alpha)$	
Pyrite	$2FeS_2 + 11/2O_2 \rightarrow 2FeS \rightarrow Fe_2O_3 + 4SO_2$	(7.2)
	$r_{pyr,1} = 3.88 \cdot 10^{16} exp\left(-\frac{240900}{R\,T}\right)(1-\alpha)$	
	$r_{pyr,2} = 7.15 \cdot 10^{15} exp\left(-\frac{280800}{R\,T}\right)(1-\alpha)$	
Calcite	$CaCO_3 \rightarrow CaO + CO_2$	(7.3)
	$r_{calc} = 1.32 \cdot 10^{10} exp\left(-\frac{209400}{R\,T}\right)2\,(1-\alpha)^{0.5}$	
Dolomite	$CaMg(CO_3)_2 \rightarrow CaO + MgO + 2CO_2$	(7.4)
	$r_{dolo} = 9.74 \cdot 10^{9} exp\left(-\frac{209100}{R\,T}\right)2\,(1-\alpha)^{0.5}$	
Ankerite	$Ca(Mg_{(1-x)}Fe_x)(CO_3)_2 \rightarrow (1-x)MgO + x/2Fe_2O_3 + CaO + 2CO_2$	(7.5)
	$r_{ank1} = 1.84 \cdot 10^{14} exp\left(-\frac{270100}{R\,T}\right)(1-\alpha)$	
	$r_{ank2} = 1.79 \cdot 10^{11} exp\left(-\frac{236600}{R\,T}\right)2\,(1-\alpha)^{0.5}$	
REF_3	$2REF_3 + 3CaO \leftrightarrow RE_2O_3 + 3CaF_2$	(7.6)
Monazite	$6REPO_4 + CaF_2 + 9CaO \rightarrow 2Ca_5F(PO_4)_3 + 3RE_2O_3$	(7.7)

The calcination of an ore is often accompanied by its particles' structural changes due to the decomposition of the minerals at high temperatures. These changes are related to the path of decomposition of the minerals, the most common being the change of size and porosity. These phenomena can occur individually, e.g. shrinkage of particle without pore formation, or together [38, 53, 54]. The effect of the minerals decomposition on the average particle size, the particle density and the surface area during the calcination in a fluidized bed is presented in Table 7.3, and on the porosity of particles is in Figure 7.3a.

Since the superficial gas velocity in the FB-TGA is not very high (U/U_{mf} ~ 1.1), we did not expect attrition of particles due to collision between the particles. This was a promising opportunity to investigate the particle's morphology during calcination.

While the average particle size remained constant with some fluctuations in the magnitude of an average particle size of 110 µm, the particle skeletal density and the surface area increased progressively along the decomposition attaining its maximum when the ore was fully calcined. The increase in the surface area considering that the particle size remains constant is related to a porosity increment in the particles, while the particle skeletal density increase, i.e. 11.5 %, is related to the formation of denser products compared to the original mineral, e.g. calcium oxide (3.34 g/cm^3) versus calcite (2.71 g/cm^3).

Table 7.3 Particle properties evolution during calcination of a REE bearing ore

T (ºC) [time in min]	0 [0]	625 [0]	700 [0]	750 [0]	800 [0]	800 [30]	800 [60]	800 [90]
X	0	0.18	0.37	0.56	0.66	0.95	0.99	1
$\overline{\boldsymbol{d_p}}$(µm)	104.4	111.1	104.3	110.1	104.7	104.8	105.8	110.6
ρ_{sk} (g/cm^3)	3.11	3.13	3.16	3.21	3.27	3.39	3.46	3.47
S_p (m^2/g)	1.012	4.237	7.033	7.887	8.576	8.693	8.800	8.919
Here in, conversion of the ore was defined as: $\boldsymbol{X} = \frac{\boldsymbol{m_0 - m_i}}{\boldsymbol{m_0 - m_{100\%\,calc.}}}$ Where m_0 is the mass of fresh ore fed into the reactor, m_i is the mass of sample during calcination, and $m_{100\%\,calc}$ is the mass of ore after the calcination is completed.								

Initially the ore, with an initial porosity of 0.01 %, was not porous, but during the calcination the sample's porosity increased until finalization of the calcination (BET measurements, Figure 7.3a). At that point, a maximum porosity of approximately 0.45 % was achieved. As for the mass loss of sample during calcination, the rate of pore formation started to kick off at approximately 550 ºC and ramped up until full decomposition of the ore. In other words, with respect to the unchanged particle size of the ore, the kinetic of pore formation or porosity had an analogous trend to the one of the ore's mass loss or conversion (Figure 7.3a).

By considering the aforementioned observations, the Levenspiel's crackling core model [38] explains best the morphology change of the Niobec ore particles in the course of calcination.

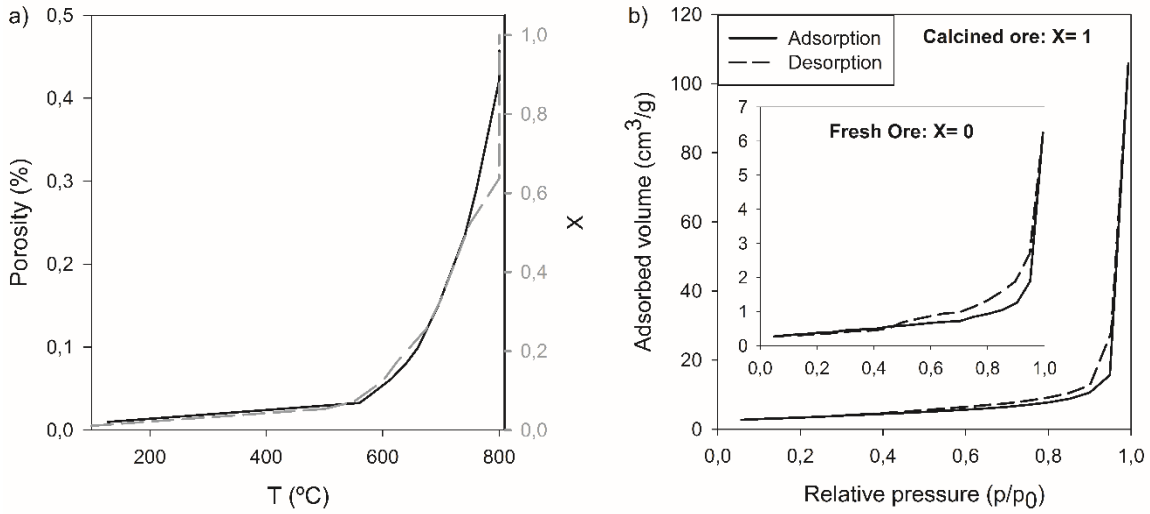

Figure 7.3 Porosity during calcination of a rare earth bearing ore: a) Porosity evolution; b) Langmuir isotherms

The pore analysis can also give an information of the route of the decomposition of the sample depending on the shape of the hysteresis of a Langmuir isotherm, e.g. progressive decomposition or decomposition from the inside to the outside. Four main types of pores can be described: both-ends open pores with a constant diameter and a particular shape (hysteresis 1), ink-bottle shaped pores (hysteresis 2), slit shaped pores (hysteresis 3) and narrow slit like pore (hysteresis 4) [55]. In this article, only the Langmuir isotherms of the feed and the final product have been represented in Figure 7.3b. In these representations, the isotherm curves described a hysteresis of type 3 which are known to describe the formation of slit mesoporous-like pores, which can be interpreted as cracks occurring in the grain of ore particles.

The formation and expansion of cracks were confirmed by SEM microscopy. Particle's SEM images at various steps of the calcination are represented in Figure 7.4. By comparing the images at each conversion (associated with a calcination temperature), a trend of expansion of the cracks is realized in all spatial direction, and thus confirming the evolution of pores (i.e. micro pores here) along with the progress of calcination.

It is worth mentioning that the ore particles had irregular morphologies before, during and after the calcination. Also, even though particles were cracked, they did not split into smaller particles, which should be due to the fluidization regime being close to minimum fluidization state. Future investigation should be dedicated to study the extend of particles cracking and possibility of their attrition under intense hydrodynamic forces in the calcining fluidized bed reactor.

From another point of view, given a fine particle size (i.e. with an average about 100μm), the level of interparticle forces at such high temperatures (e.g. capillary forces) were insignificant when the hydrodynamic forces were mild; that is, particles did not tend to sinter and finally agglomerate.

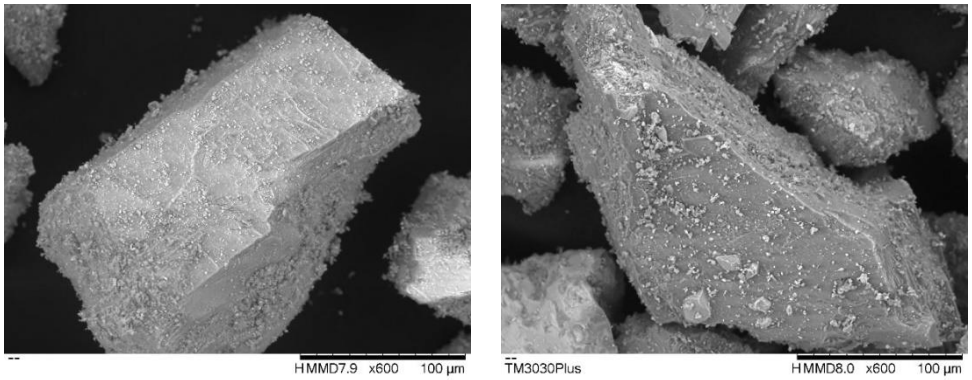

X = 0% X = 12.4%

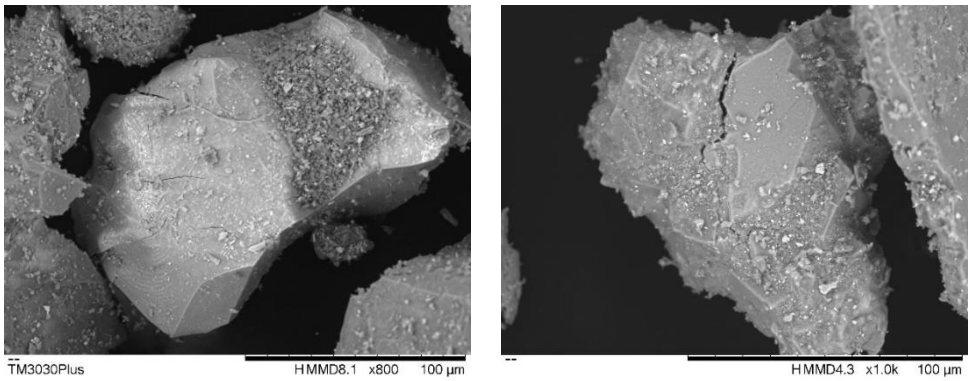

X = 33.1% X = 52.3%

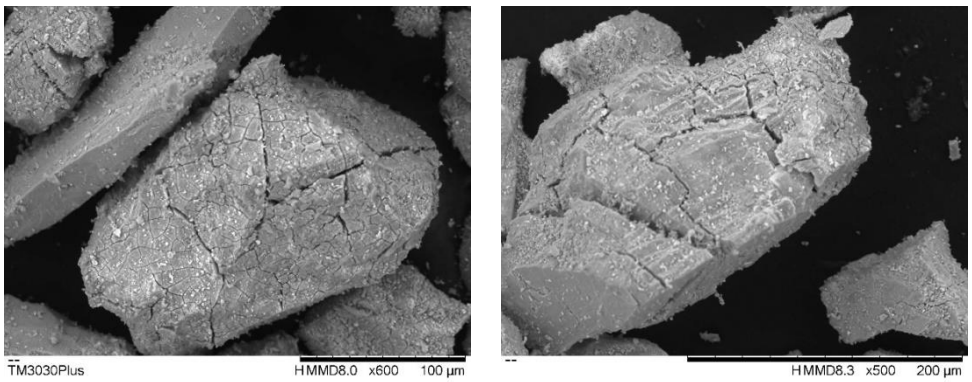

X = 96.4% X = 100%

Figure 7.4 SEM images of a rare earth at different calcination conversion

7.3.2 Liberation vs association

In mineral processing, crushing and grinding define the first step of the process. In it, the liberation size defined as the size at which the valuable minerals, i.e. bastnäsite and monazite in this study, are fully liberated from the gangue is a key parameter of design [56]. Obtaining the liberation size increases the efficiency downstream process by physical beneficiation, since liberated minerals are easier to separate from the gangue [6, 57].

In this work, where approximately 70 wt.% of the gangue material are carbonatite minerals, QEMSCAN analysis allowed to verify the presence of the valuable minerals bastnäsite and monazite in the form of fine grains, with a mean grain size of 14 and 13 µm respectively (Table 7.4). Thus, REE minerals are more susceptible to be liberated at low particle size.

Table 7.4 Mean size grain of the main minerals of Niobec ore

Mineral	**REE minerals**		**Gangue**				
	Bastnaesite	**Monazite**	**Calcite**	**Dolomite**	**Ankerite**	**Pyrite**	**Quartz**
Mean size grain (µm)	14	13	20	27	22	25	14

By QEMSCAN analysis it was also possible to study the association of the REE minerals to the gangue for different cut sizes, as represented in Figure 7.5. In general, bastnäsite and monazite are disseminated, and for particles above 55 µm, they are mainly associated with carbonatite gangue minerals (80 wt.% or more). They start to be liberated when the ore is grinded to a particle size below 150 µm and 115 µm respectively. As presented by the mean grain size of a mineral (Table 7.4), when particles are grinded below 20 µm, approximately 80 wt.% of bastnäsite and 78 wt.% of monazite are fully or partially liberated while the rest is associated to quartz, mica or carbonate minerals (Figure 7.5).

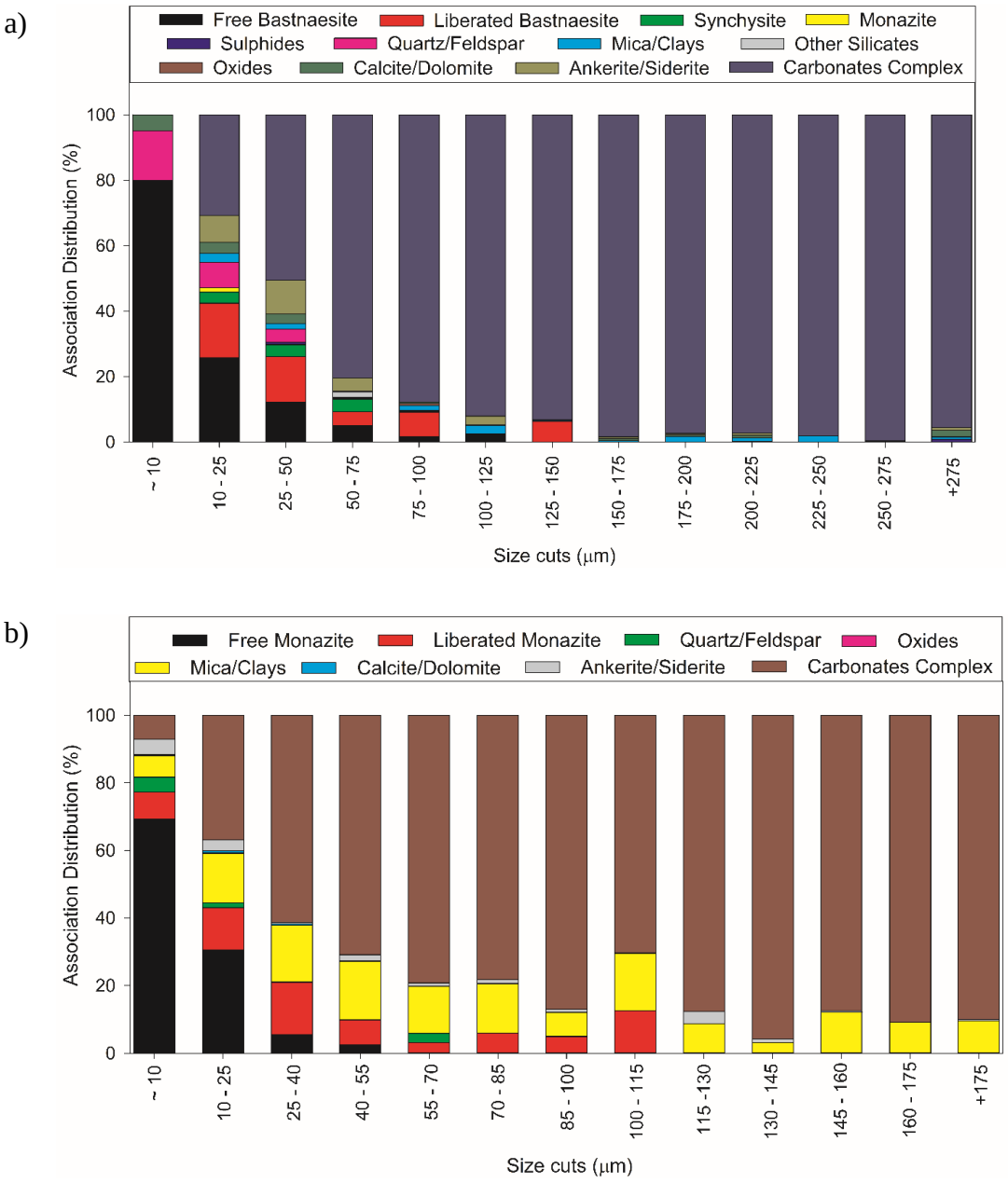

Figure 7.5 Mineral association of a) bastnäsite and b) monazite in the raw rare earth ore

As opposed to the interest of liberation size in mineral processing, the association of minerals can be of interest for the interaction or solid-solid reactions taking place within minerals. On that regard, some studies related to calcination of pure mineral forms have shown that monazite

interacts with other oxide components at high temperature, e.g. with CaO to form $Ca_3(PO_4)_2$ starting at 700 ºC, while it does not decompose on its own [23, 25, 52].

A similar reaction as the one described in literature was observed when performing the calcination of a rare earth ore with a 63 to 125 µm particle size cut in a fluidized bed. At this size, approximately 70 wt.% of monazite is associated with carbonate minerals, e.g. calcite (Figure 7.5). The calcium oxide from this study was inherently produced in the course of the calcination of the calcite, dolomite and ankerite of the Niobec ore (Reactions 7.3-7.5). This contact between calcium oxide and monazite allows the reaction between them to take place within a particle in the form of Reaction 7.7. The formation of fluorapatite ($Ca_5F(PO_4)_3$) (0.21 wt.%), undetected in the raw ore, was detected by QEMSCAN analysis. Figure 7.6 represents a comparison of the modal mineralogy of an ore before and after calcination. Considering the mineral association of monazite for each particle size cut, bigger particles will improve the production of rare earth oxides (monazite conversion) (Table 7.5).

Besides the particle size of the ore, the kinetics, described as slow in literature [58], and the reactor selection may affect the solid-solid reaction. Fluidized bed reactors, despite being advantageous for gas-solid reactions, reduce the contact between minerals when they are found in separated particles. Therefore, it is important to evaluate the contact within a particle, since as there is no attrition during the calcination in a fluidized bed, the minerals' association is still ensured.

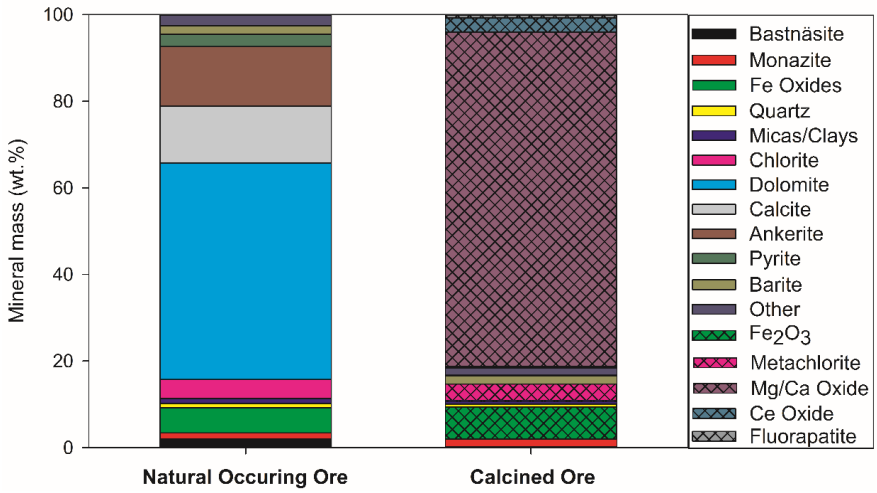

Figure 7.6 Modal mineralogy of Niobec fresh and calcined ore (measured with QEMSCAN)

7.3.3 Impact of particle size on calcination performance and extraction of REO

The selection of an appropriate particle size plays a major role in the mineral processing from the efficiency and the economy points of view. In this research, we opted for four size cuts, i.e. below 20, 63, 150 and 250 µm, to illustrate how a specific size might improve the process performance to recover rare earth elements with a high enrichment ratio (or selectivity).

Hence, we analyzed three main criteria: the effect of particle size on the calcination (ore and monazite conversion), the capability to recover the maximum rare earth elements with a high selectivity in a downstream leaching process by a mild acid, and a perspective economic impact it might have on the overall process economy (comminution, calcination, and leaching).

The efficiency of the fluidized bed calcination process on the particle size was evaluated considering the decomposition mechanism and effect on the particle size for each size cut of the calcination and the decomposition by solid-solid reaction of monazite with the calcium oxide.

We employed the IHFBR initially to obtain an insight about the kinetic differences between each size cut (Figure 7.7). The thermograms did not show any appreciable difference, and as shown in Figure 7.7, the calcination finalized after a few minutes at 800 ºC. As it can be expected by the difference in particle sizes, the calcination started earlier for smaller particles, nonetheless, the final reaction time was similar reaction for all particles (Figure 7.7b). In addition, carbon analysis of the calcined samples by LECO indicated that all samples reached full conversion (Table 7.5). Thus, the particle size did not affect the gas-solid reactions of the calcination process; on the other hand, this is advantageous to operate the fluidized bed reactor in a coarser size of particles because it reduces the size of cyclones for solids recovery, and subsequently the risk of powders loss from the reactor outlet.

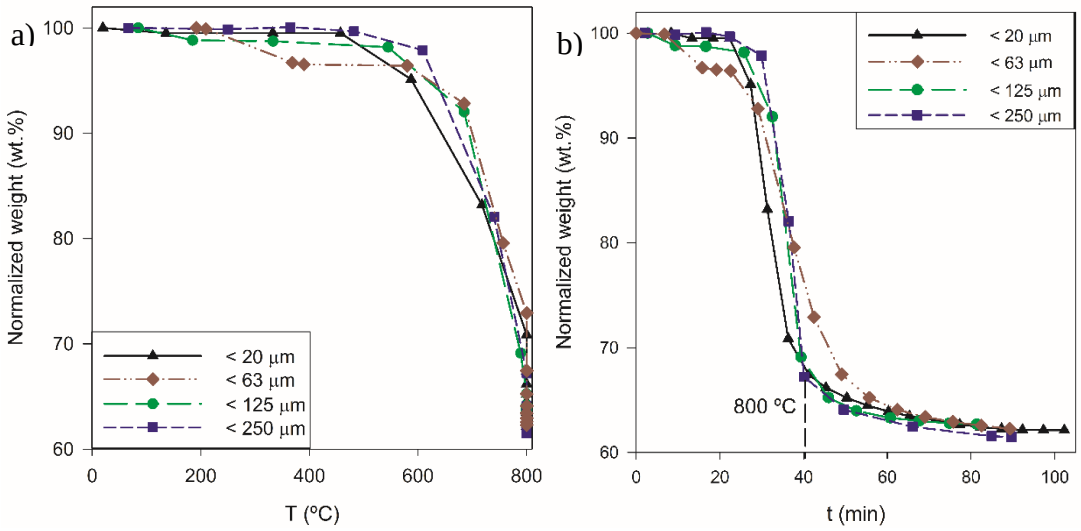

Figure 7.7 Thermogram of a rare earth ore calcination in an IFBHR reactor at 800 ºC versus: a) Temperature; b) Time

The assertion made in Section 7.3.1 regarding the unchanging particle size during calcination was also confirmed in this study for particles above 20 µm. However, in case of the <20 µm size cut, the average particle size increased after calcination due to agglomeration (Table 7.5 & Supplementary data). This cut size of particles belongs to Geldart's group C particles that are known to be cohesive particles having tendency to agglomerate [59]. Nonetheless, this agglomeration did not affect the calcination process.

During calcination, monazite, by its association with CaO (Figure 7.5b), decomposed by solid-solid reaction under a high temperature (Figure 7.6). Mineral association in an ore varies depending on the particle size and the liberation size of the mineral. For monazite, its association to carbonatite minerals increases with the particle size of the ore, reaching around 80 wt.% for particles above 55 µm.

To evaluate the decomposition of monazite, its conversion, defined by Equation 8, was calculated based on the concentration before and after calcination (estimated by QEMSCAN). It must be noted that the mineral concentration for particles below 20 µm slightly differed from those of Table 6.1, and monazite concentration for that size cut was around 1.6 wt.%.

$$X_{monazite} = \frac{w_{mon,in}/ml - w_{mon,out}}{w_{mon,in}/ml} \cdot 100 \quad (8)$$

Where $X_{monazite}$ denotes the conversion of monazite in %, $w_{mon,in}$ and $w_{mon,out}$ are monazite's mass fraction before and after calcination in wt.%, and ml is the fraction of mass remaining in the reactor after calcination (approximately 0.621).

At the same conditions of calcination, the degree of dephosphorization was higher for larger particles (125 or 250 µm), where approximately 50% of monazite was decomposed, while for small particles where monazite is almost fully liberated or free, only 10% of monazite decomposed (Table 7.5). This result was caused by the association between monazite and the calcium oxide that is necessary to favor the reaction.

Table 7.5 Results from a calcining and leaching processes on a rare earth ore

	Calcination process				**Leaching process**			
d_p **(µm)**	$\overline{d_p}$ **(µm)**	**Sp (m^2/g)**	**$C_{removal}$ (wt.%) [a]**	**Monazite Conversion (%)**	**TREE Enrichment ratio [b]**		**Solid phase Recovery (%)**	
					Calc.	**FO**	**TREE**	**Ca**
< 20	26.7 ±2.1 (10.5 ±0.3)	6.819 (3.313)	99.4	10.7	1.6	2.3	91.4	14.5
< 63	28.8 ±1.1 (27.6 ±1.7)	8.814 (2.459)	99.5	44.7	2.1	3.1	90.2	10.7
< 125	39.1 ±2.4 (37.6 ±2.6)	9.667 (2.071)	99.5	49.0	2.1	3.0	90.8	9.3
< 250	102.3 ±6.0 (98.2 ±4.7)	10.355 (1.988)	99.5	53.2	2.3	3.3	90.9	5.0

The particle's characteristics of the raw ore for each cut size can be found in parenthesis.
[a] Carbon was measured by LECO analysis
[b] Enrichment ratio expressed as a function of the calcined product (Calc.) and the natural ore feed (FO)

From the point of view of the calcination process, a bigger particle size, i.e. 125 or 250 µm, is preferred for the process since they are easier to fluidize, and it will allow a higher dephosphorization of monazite in the ore. It must be noted that to maximize monazite's dephosphorization, the ore's residence time in the reactor should be longer than 1h.

As a second part of the analysis, the calcined ore underwent an acid leaching treatment. The rare earth elements were recovered with most of the iron and manganese in the solid phase, while calcium and magnesium were leached (Figure 7.8a). The calcination process modified the sample properties especially by increasing the particles porosity, thus improving the leaching.

To evaluate the effect of the particle size on the leaching, the elemental recovery in the solid phase is illustrated in Figure 7.8 and the rare earth element enrichment ratio can be found in Table 7.5. The acid treatment allowed to effectively separate calcium and magnesium from the ore by recovering more than 83% of these elements on the leachate. The separation rate increased with the grain size, since calcium separation rate increased from 86.5% to 95% for calcined particles below 20 and 250 µm respectively. Similar trends were observed for magnesium and iron, whose separation rate from the rare earths elements increased with the size. In the case of magnesium, the increase was not significant, going from 83% to 86.1%; but the separation rate for iron was enhanced by 50%, from 21% to 33% recovery in the leachate. Despite the effect of the particle size on the leaching of these impurities (Ca, Mg and Fe), the recovery of rare earth elements and manganese in the solid phase remained independent of the particle size with approximately 90% and 86% of recovery respectively (Figure 7.8a).

Focusing on the rare earth elements as the interest of the ore, their recovery rate could be divided in two groups, cerium and the rest of rare earth elements. During calcination cerium tend to form cerium oxide IV (CeO_2) while other rare earths are oxide III (RE_2O_3) [60]. The change of oxidation state implies a distinct behavior of cerium during leaching. In that regard, cerium recovery in the solid phase was approximately 97%, while the recovery of other rare earths with the same oxidation state was around 84% (Figure 7.8b).

Since the leaching recovery rate of impurities increased with the particle size of the calcined ore, the enrichment ratio of rare earth elements in the solid product of the leaching followed the same tendency. For particles below 20 µm the enrichment ratio from the fresh ore (before calcination) was 2.35. This factor increased to 3.34 when leaching was performed on a calcined ore with particles below 250 µm (Table 7.5). The effect of the particle size of calcined ore on leaching can be related to the available surface area of grains for leaching. The surface area of the calcined ore increased with the particles size caused by an increase of porosity of particles, reaching 10.36 m^2/g

for calcined particles below 250 µm. In the case of particles below 20 µm the available surface area susceptible of being leached was about 6.82 m^2/g (Table 7.5), which could have been reduced by the agglomeration taking place during the calcination.

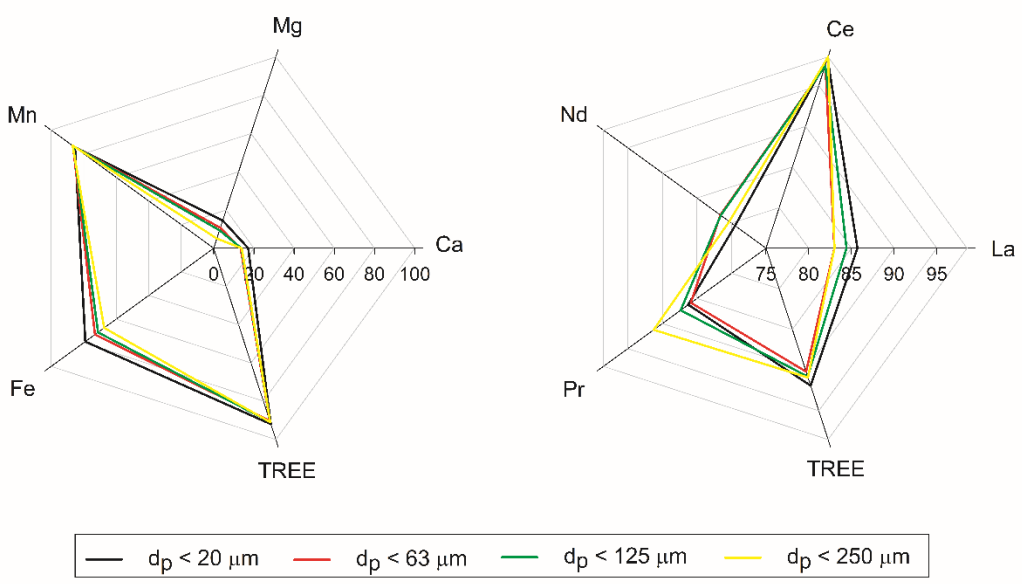

Figure 7.8 Elemental recovery in the solid phase from the acid leaching on calcined ore

From the upstream point of view, the demand for a certain particle size will impact the milling processes. Curry et al, 2014 presented a comprehensive study regarding the cost distribution in mining operations and determined that the mining and milling processes often represent the main operating costs, e.g. equipment operation and energy, of a mining project [61, 62]. It is estimated that 70% of the energy cost of a mining plant is related to the comminution of an ore, and most of this cost is generated during grinding [61, 63, 64]. This percentage may vary in function of the ore type and grain size among other factors [61, 65]. In fact, the proper selection of a particle size or an adequate technology for size reduction can induce savings in a mineral processing circuit [61, 62, 66].

In rare earth industry, concentration of metals is done by physical beneficiation which usually implies the need of smaller particles, having thus an enormous impact on the grinding and comminution processes [1]. In this study, the selection of bigger particles is appropriate to reduce

the energetic cost and the dust production during the comminution process. Such reduction can be achieved if the calcination, performed in a fluidized bed, was done for an ore with a particle size below 250 μm.

7.4 Conclusions

Calcination of a rare earth bearing ore in a fluidized bed and its effect on the particles' mineralogy and characteristics were investigated along with the effect of the particle size in the technicalities of a process. This study covered the calcination of the ore and the leaching of its respective product.

The calcination of the ore produced metal oxides, e.g. CaO or Fe_2O_3, among which the rare earth oxides produced by the decomposition of bastnäsite and monazite. While bastnäsite decomposed at low temperature (400 ºC), monazite's dephosphorization takes place by its interaction with other solid forms at high temperature (700 ºC). Due to its presence in free or liberated form, full conversion of rare earths to its oxide form cannot be achieved, but at coarser sizes, monazite's association to carbonatite gangues enhanced its transformation to oxide, being able to reach an 80 wt.% overall conversion. At lower sizes, monazite is freed or liberated, hindering its conversion.

The process performed in a fluidized bed was consistent with a test performed at same conditions (heating rate and temperature) with only a few milligrams in a thermogravimetric analyzer. The high amount of gas produced compared to the reactor size during calcination in the fluidized bed entrained some diffusion control during the decomposition. This phenomenon should not be observed in large scale reactors. The ore's roasting generated the formation of cracks as the porosity increased within the ore while the ore size remained unchanged.

The change of the samples' characteristics, such as the surface area increment, during calcination improved the elemental leaching of the impurities (Ca, Mg and Fe) found along the rare earths, and allowed to achieve an enrichment ratio of rare earths up to 3.3. From an industrial point of view, a bigger particle size (250 μm) enhanced monazite's conversion to rare earth oxides and improved the leaching performance by extracting more impurities in the leachate and having a higher enrichment ratio than other particle sizes. The selection of a bigger particle size for the calcination process was also preferable upstream, since it will reduce the energetical cost of the comminution

process. Finally, entrainment of smaller particles would be corrected in industrial scale by a cyclone.

7.5 Acknowledgements

Authors would like to acknowledge Natural Science and Engineering Research Council of Canada (NSERC/CRD) and Niobec, a company in Province of Quebec of Canada for their financial support, Michelle Kelvin and XPS Expert Process Solutions for providing the QEMSCAN analysis and Fatma Ben Dhieb for the image analysis (SEM).

7.6 References

1. Gupta, C.K. and N. Krishnamurthy, *Extractive Metallurgy of Rare Earths*. 2004: CRC Press.
2. DOE, *Critical Materials strategy*, U.S.D.o. Energy, Editor. 2015.
3. Giacalone, J.A., *The Market For The "Not-So-Rare" Rare Earth Elements* Journal of International Energy Policy, 2012. **1**: p. 11-18.
4. Dent, P.C., *Rare earth elements and permanent magnets (invited).* Journal of Applied Physics, 2012. **111**(7): p. 07A721.
5. Sagawa, M., et al., *Permanent magnet materials based on the rare earth-iron-boron tetragonal compounds.* IEEE Transactions on Magnetics, 1984. **20**(5): p. 1584-1589.
6. Jordens, A., Y.P. Cheng, and K.E. Waters, *A review of the beneficiation of rare earth element bearing minerals*. Minerals Engineering, 2013. **41**: p. 97-114.
7. Simandl, G.J., *Geology and economic sifnificance of current and future rare earth element sources*, in *51st Annual Conference of Metallurgists* J.R. Goode, G.A. Moldoveanu, and M.S. Rayat, Editors. 2012: Niagara Falls.
8. Mariano, A.N. *Nature of economic mineralization in carbonatites and related rocks*. in *Carbonatites: Genesis and Evolution*. 1989. London.
9. Mariano, A.N. *Economic geology of rare earth elements*. in *Reviews in Mineralogy*. 1989. Washington DC: Mineralogical Society of America.
10. Wall, F. and A.N. Mariano, *Rare earth minerals in carbonatites: A discussion centred on the Kangankunde carbonatite, Malawi*, in *Rare Earth Minerals: Chemistry, Origin, and Ore Deposits*, A.P. Jones, F. Wall, and C.T. Williams, Editors. 1996, Chapman & Hall: London. p. 193-225.

11. Gupta, C.K. and N. Krishnamurthy, *Extractive Metallurgy of Rare-Earths.* International Materials Reviews, 1992. **37**(5): p. 197-248.
12. Habashi, F., *Extractive metallurgy of rare earths.* Canadian Metallurgical Quarterly, 2013. **52**(3): p. 224-233.
13. Chi, R., et al., *Recovery of rare earth from bastnasite by ammonium chloride roasting with fluorine deactivation.* Minerals Engineering, 2004. **17**(9-10): p. 1037-1043.
14. Kul, M., Y. Topkaya, and I. Karakaya, *Rare earth double sulfates from pre-concentrated bastnasite.* Hydrometallurgy, 2008. **93**(3-4): p. 129-135.
15. Criado, J.M. and A. Ortega, *A study of the influence of particle size on the thermal decomposition of CaCO3 by means of constant rate thermal analysis.* Thermochimica Acta, 1992. **195**: p. 163-167.
16. Földvári, M., *Handbook of thermogravimetric system of minerals and its use in geological practice*, ed. G.I.o. Hungary. Vol. 213. 2011, Budapest.
17. Reller, A., et al., *Thermochemical Reactivity of Metal Carbonates.* Chimia, 1991. **45**: p. 262-266.
18. Guentner, J., et al., *Recovery of rare earth elements from complex raw materials by Outotec's Solutions*, in *IMPC 2016: XXVIII International Mineral Processing Congress Proceedings*. 2016: Quebec City.
19. Xing, P., et al., *High temperature dephosphorus behavior of Baotou mixed rare earth concentrate with carbon.* Journal of Rare Earths, 2010. **28**: p. 194-197.
20. Yuan, S., et al., *Roasting decomposition of mixed rare earth tailings by CaO in reducing atmosphere.* Rare Metals, 2014.
21. Xiang, J., et al., *Thermal decomposition behaviour of natural bastnasite crystal in calcination.* Transaction of NFsoc, 1994. **4**(4): p. 34-38.
22. Hikichi, Y. and T. Nomura, *Melting Temperatures of Monazite and Xenotime.* Journal of the American Ceramic Society, 1987. **70**(10): p. C-252-C-253.
23. Hikichi, Y., T. Ota, and T. Hattori, *Thermal mechanical and chemical properties of sintered monazite (La, Ce, Nd or Sm).* Mineralogical Journal, 1997. **19**(3): p. 123-130.
24. Huang, Y., et al., *Leaching kinetics of rare earth elements and fluoride from mixed rare earth concentrate after roasting with calcium hydroxide and sodium hydroxide.* Hydrometallurgy, 2017. **173**: p. 15-21.
25. Kumari, A., et al., *Thermal treatment for the separation of phosphate and recovery of rare earth metals (REMs) from Korean monazite.* Journal of Industrial and Engineering Chemistry, 2015. **21**: p. 696-703.
26. Wu, W.Y., et al., *Reaction process of monazite and bastnaesite mixed rare earth minerals calcined by CaO-NaCl-CaCl2.* Transactions of Nonferrous Metals Society of China, 2007. **17**(4): p. 864-868.

27. Xing, P.F., et al., *High temperature dephosphorization behavior of monazite concentrate with charred coal.* Transactions of Nonferrous Metals Society of China, 2010. **20**(12): p. 2392-2396.

28. Samih, S., et al., *From complex feedstocks to new processes: The role of the newly developed micro-reactors.* Chemical Engineering and Processing - Process Intensification, 2018. **131**: p. 92-105.

29. Kohav, T., J.T. Richardson, and D. Luss, *Axial dispersion of solid particles in a continuous rotary kiln.* AIChE Journal, 1995. **41**(11): p. 2465-2475.

30. Rasouli, M., et al., *Investigating the dynamics of cylindrical particles in a rotating drum using multiple radioactive particle tracking.* AIChE Journal, 2016. **62**(8): p. 2622-2634.

31. Menéndez, M., et al., *Experimental Methods in Chemical Engineering: Reactors---Fluidized Beds.* The Canadian Journal of Chemical Engineering, 2019.

32. Watkinson, A.P. and J.K. Brimacombe, *Limestone calcination in a rotary kiln.* Metallurgical Transactions B, 1982. **13**(3): p. 369-378.

33. Bemrose, C.R. and J. Bridgwater, *A review of attrition and attrition test methods.* Powder Technology, 1987. **49**(2): p. 97-126.

34. Jia, L., et al., *Attrition of Calcining Limestones in Circulating Fluidized-Bed Systems.* Industrial & Engineering Chemistry Research, 2007. **46**(15): p. 5199-5209.

35. Samih, S. and J. Chaouki, *Development of a fluidized bed thermogravimetric analyzer.* AIChE Journal, 2015. **61**(1): p. 84-89.

36. Aghabararnejad, M., G.S. Patience, and J. Chaouki, *Transient modeling of biomass steam gasification with Co3O4.* Fuel, 2015. **140**: p. 354-364.

37. Evans, P., T. Paskach, and J. Reardon, *Detailed kinetic modeling to predict syngas composition from biomass gasification in a PBFB reactor.* Environmental Progress & Sustainable Energy, 2010. **29**(2): p. 184-192.

38. Levenspiel, O., *The Chemical Reactor Omnibook*. 1989.

39. Samih, S. and J. Chaouki, *Coal pyrolysis and gasification in a fluidized bed thermogravimetric analyzer.* The Canadian Journal of Chemical Engineering, 2018. **96**(10): p. 2144-2154.

40. Carrillo Garcia, A., *Thermal decomposition of a rare earth ore*, in *Chemical Engineering*. 2019, Polytechnique Montreal: Montreal.

41. Kunii, D. and O. Levenspiel, *Fluidization Engineering*. 1991, Boston.

42. Latifi, M., F. Berruti, and C. Briens, *A novel fluidized and induction heated microreactor for catalyst testing.* AIChE Journal, 2014. **60**(9): p. 3107-3122.

43. Latifi, M. and J. Chaouki, *A novel induction heating fluidized bed reactor: Its design and applications in high temperature screening tests with solid feedstocks and prediction of defluidization state.* AIChE Journal, 2015. **61**(5): p. 1507-1523.

44. Abdollahi Neisiani, M., et al., *Novel approach in k 0 -NAA for highly concentrated REE Samples.* Talanta, 2018. **180**: p. 403-409.

45. Vyazovkin, S., et al., *ICTAC Kinetics Committee recommendations for performing kinetic computations on thermal analysis data.* Thermochimica Acta, 2011. **520**(1-2): p. 1-19.

46. Vyazovkin, S., et al., *ICTAC Kinetics Committee recommendations for collecting experimental thermal analysis data for kinetic computations.* Thermochimica Acta, 2014. **590**: p. 1-23.

47. Hong, Y. and B. Fegley, *The kinetics and mechanism of pyrite thermal decomposition.* Berichte der Bunsengesellschaft für physikalische Chemie, 1997. **101**(12): p. 1870-1881.

48. Schorr, J.R. and J.O. Everhart, *Thermal Behavior of Pyrite and Its Relation to Carbon and Sulfur Oxidation in Clays.* Journal of The American Ceramic Society, 1969. **52**(7).

49. Srinivasachar, S. and A.A. Boni, *A Kinetic-Model for Pyrite Transformations in a Combustion Environment.* Fuel, 1989. **68**(7): p. 829-836.

50. Odogorova, L.P., et al., *Natural Mg-Fe clinochlores Enthalpies of formation and dehydroxylation derived from calorimetric study.* American Mineralogist, 2016. **101**: p. 1431-1437.

51. Villieras, F., et al., *Development of microporosity in clinochlore upon heating.* Clays and Clay Minerals, 1994. **42**(6): p. 679-699.

52. Hikichi, Y., K.-i. Hukuo, and J. Shiokawa, *Solid State Reactions between Rare Earth Orthophosphate and Oxide.* Bulletin of the Chemical Society of Japan, 1980. **53**(5): p. 1455-1456.

53. Levenspiel, O., *Chemical Reactor Engineering*. Second Edition ed, ed. W.I. Edition. 1972.

54. Veglio, F. and F. Beolchini, *Removal of metals by biosorption: a review.* Hydrometallurgy, 1997. **44**(3): p. 301-316.

55. Sing, K.S.W., *Reporting physisorption data for gas/solid systems with special reference to the determination of surface area and porosity (Recommendations 1984).* Pure and Applied Chemistry, 1985. **57**(4): p. 603-619.

56. Barbery, G., *Mineral Liberation: Measurement, Simulation and Practical Use in Mineral Processing*. 1991: Éditions GB.

57. Jordens, A., et al., *Processing a rare earth mineral deposit using gravity and magnetic separation.* Minerals Engineering, 2014. **62**: p. 9-18.

58. Xue, B., et al., *Kinetics of Mixed Rare Earths Minerals Decomposed by CaO with NaCl-CaCl2 Melting Salt.* Journal of Rare Earths, 2010. **28**(Spec. Issue): p. 86.

59. Yao, W., et al., *Fluidization and agglomerate structure of SiO2 nanoparticles.* Powder Technology, 2002. **124**(1-2): p. 152-159.

60. Zhao, L., et al., *Thermal decomposition and oxidation of bastnaesite concentrate in inert and oxidative atmosphere.* Journal of Rare Earths, 2018. **36**(7): p. 758-764.

61. Curry, J.A., M.J.L. Ismay, and G.J. Jameson, *Mine operating costs and the potential impacts of energy and grinding.* Minerals Engineering, 2014. **56**: p. 70-80.

62. Gupta, A. and D.S. Yan, *Size Reduction and Energy Requirement*, in *Mineral Processing Design and Operation*. 2006, Elsevier: Netherlands.

63. Ballantyne, G.R., M.S. Powell, and M. Tiang, *Proportion of energy attributable to comminution*, in *Proceedings of 11th Mill Operators' Conference*. 2012, Australasian Institute of Mining and Metallurgy: Hobart, Tasmania. p. 25-30.

64. Norgate, T.E. and S. Jahanshahi, *Improving the sustainability of primary metal production - The need for a life cycle approach*, in *Proceedings of XXV International Mineral Processing Conference (IMPC)*. 2010, Australasian Institute of Mining and Metallurgy: Brisbane, Qld, Australia. p. 3575-3584.

65. Crowson, P., *Some observations on copper yields and ore grades.* Resources Policy, 2012. **37**(1): p. 59-72.

66. Evans, C.L., et al., *Improving energy efficiency across mineral processing and smelting operations – a new approach*, in *Proceedings of SDIMI Conference*. 2009, The Australasian Institute of Mining and Metallurgy: Gold Coast, QLD, Australia. p. 9-13.

CHAPTER 8 GENERAL DISCUSSION

Rare earth elements extraction is made of a complex array of unit processes that together are source of important environmental problems and low rare earth recovery. To reduce environmental impacts caused by the hydrometallurgy of the process, some studies have performed thermal studies with an agent addition to the rare earth concentrate produced after physical beneficiation. The addition of the agent varied based on the REE mineral, since fluorine deactivation from bastnäsite was achieved with the addition of an alkali agent; while monazite concentrate decomposition at lower temperature was achieved by addition of a lime or a salt.

In this work, the production of rare earth oxides as an early stage of the process by thermal decomposition is presented. As a difference to other studied thermal decomposition processes where the addition of an agent to reduce monazites decomposition or to deactivate fluorine downstream is necessary, this process takes advantage of the mineral composition of the ore to deal with those issues. While fluorine is captured in the form of calcium fluoride and fluorapatite, monazite, by its association with calcite, is decomposed at around 700 to 800 ºC. On that regard, the reaction of monazite takes place with the calcium oxide which is a product from the calcination of the calcite taking place during calcination.

At first, the reaction mechanism of the ore was developed in order to prepare a comprehensive kinetic model for the thermal decomposition of the ore. The kinetic study was thus divided in two parts, the study of decomposition of individual minerals following the reaction mechanism and the lumping or combination of the individual minerals kinetic to have a more general kinetic model that was able to describe the decomposition of the Niobec ore.

Regarding the minerals' decomposition, it was observed that main minerals of the ore, i.e. carbonatites, decomposed at high temperature (600 to 800ºC), producing CO_2 gas and metal oxides. During these reactions, some researchers described the reverse reaction to take place due to the pressure increase of the gas product. Nonetheless, in this research it has been shown that such situation of reversible reaction can be neglected in the thermal decomposition of the ore performed in a fluidized bed or with a high gas flowrate. This neglection is caused by formation of pores and the high gas flow rate that allow the fast sweeping of the product gas. This was assumed for the calcination taking place in the fluidized bed reactor and was demonstrated for the calcination

performed during the kinetic analysis in the TGA (Chapter 5). Despite showing that there is not any reversible reaction in laboratory scale for the calcination in TGA (at high flowrates) and fluidized bed, when calcination is brought to industrial scale, the selection of the reactor will have an important effect on the gas sweeping and by extension on the reversible reaction. Such is the case for fixed beds or rotary kilns, where the gas produced inside the particles diffuses slowly through the layers of particles, increasing thus the reactor's pressure. Kinetics developed in this study cannot be used to model those reactors, since mass transfer limitation and reversible reactions, that were considered negligible in this work, will have an important effect on the calcination's performance. Such effect was shown in Figure 7.1 of Chapter 7, where calcination in a fixed bed needed more than four hours to achieve full conversion. Other factors that will affect the calcination performance and the reversible reactions are the reactor hydrodynamics and the mass transfer between the gas and the solid, since gas-solid contact and thermal gradients will also affect the decomposition of minerals.

Introducing the effect of equilibrium in the kinetic study would increase the accuracy of the global kinetic model as it is based on the combination of the individual minerals kinetic. On that regard, the use of the model developed in this work is limited to carbonatite-based deposits (approximately 50% of the rare earth deposits) and could be improved for future use to other calcination studies of an ore if several other minerals were to be included into the model. For instance, in this work, the minerals considered for the kinetic study were those with a concentration higher than 0.9 wt.%. The selection was based on the effect that low concentrated minerals would have on the global calcination and the difficulty to find a pure form of some of these minerals. Increasing the kinetic study of minerals could thus be useful to generate a simile of a database for kinetic studies purpose which could widen the use of the model to more deposits types. A limit for this kind of lumped model will always be the bottleneck found during the modal mineralogy analysis, since during analysis, some minerals cannot be described accurately and are presented as a more generic name, e.g. mica or clays, due to the presence of a mixture of this mineral group within the ore. Therefore, most of the limitations that could avoid developing a global model forward, are related to mineral characterization limitation.

As opposed to flotation and other physical beneficiation process where smaller particle sizes are preferable due to the liberation size of the minerals of interest, calcination's performance increased

with the particle size (Chapter 7). Even though fluidized beds are not recommended reactors to have solid-solid reactions, increasing the particle size of the calcined ore also increased the association of monazite with calcite within the particle. The increased minerals association allowed a higher decomposition of monazite to produce rare earth oxide. In the same study it was shown that calcining bigger particles created a higher porosity compared to smaller particles, such morphology modification allowed a more selective leaching of the gangue material. Therefore, calcination process is useful to reduce the cost of grinding and the problems related to fines that are found in more conventional processes.

Despite showing promising results, a thorough economic evaluation of a calcination process for rare earth production still needs to be prepared. In order to be comparable to a conventional process that includes physical beneficiation and a more aggressive hydrometallurgy, the economic analysis should be prepared considering all the chain of production from the ore to the final product, since applying thermal decomposition on the ore instead of the concentrates completely modifies the rare earth process.

CHAPTER 9 CONCLUSION AND RECOMMENDATIONS

9.1 Conclusions

The calcination study performed on a rare earth bearing ore has shown to produce rare earth oxides from bastnäsite and monazite rare earth bearing minerals.

The calcination of the rare earth ore presented two types of reactions, gas-solid and solid-solid. Gas-solid reactions were tracked by thermogravimetric tests and three steps of decomposition defined by its pure minerals. At lower temperature (approximately 400 ºC), bastnäsite (1.96wt.%), decomposed producing rare earth oxides. Between the first and the second reaction step (at around 500 ºC), some other minor minerals, e.g. pyrite and chlorite, decomposed producing SO_2 and H_2O. The last step of reaction (600 ºC) was the main step since the carbonate gangue minerals, e.g. calcite, represented 76.9 wt.% of the ore.

The decomposition of the carbonate gangue minerals produced among other compounds calcium oxide, which by its association to monazite was able to decompose the rare earth phosphate mineral at high temperatures producing rare earth oxide. In this case, monazite's decomposition is limited by its association with carbonatite minerals and cannot achieve full conversion since part of the mineral is free, liberated or in contact with other minerals (quartz or mica).

Understanding the reaction mechanism of the ore's calcination allowed the development of a global kinetic model for the ore's decomposition. This model was based on the kinetic parameters of the calcination of the individual minerals composing the ore and was adapted to predict the calcination of the ore with different particle sizes.

The kinetic model was then validated in a fluidized bed micro-reactor, where the calcination of the ore was performed. This reactor was selected in this work due to its enhanced gas-solid mixing and gas sweeping. A morphological study of the ore during the calcination in the fluidized bed reactor showed that the particle size remained constant while cracks were formed during the calcination. The formation of cracks along the reaction facilitated the degassing of CO_2 and SO_2. The low attrition and shrinkage of particles during the calcination ensured the contact between monazite and calcium oxide that was previously mentioned and allowed the decomposition of monazite to take place. Monazite's decomposition was also favored by a proper selection of the particle size,

since for bigger particle size (< 250 µm) a higher monazite-calcium oxide association was found and thus monazite's conversion to rare earth oxide increased.

Finally, the enrichment of rare earth element also increased with bigger particles, since calcination of those particles increased the available surface area for acid leaching. With a higher surface area, more gangue was leached, and for an ore particle size below 250 µm, 95 wt.% of calcium (gangue) was leached, while more than 90 wt.% of rare earth elements remained in the solid cake. Thus, with this process a high rare earth recovery and a rare earth enrichment ratio of 3.3 were achieved.

9.2 Recommendations

This work shed light on the calcination of a rare earth bearing ore for the production and concentration of rare earth oxides. In addition to this insight, there is still room for new studies that could complement this work:

- Study the kinetics of monazite decomposition with CaO.

Several studies regarding the decomposition of monazite are available in literature [9, 13, 15, 17]. Nonetheless, just a few discuss about its reaction with calcium oxide [13, 17], and only one describes the kinetics of such reaction [17]. Since the latter is the only one that describes the kinetics of such reaction, a more extensive study regarding the effect of the grain size of each mineral on the decomposition is missing. In order to complement this work, a reaction between both compounds with the grain size found by QEMSCAN could shed more light on the reaction between both minerals.

- Increase the heating rates of the calcination to mimic the industrial process.

Several heating rates have been studied to develop and validate a kinetic study of the calcination of the rare earth ore. These heating rates are low (2 to 40 ºC/min) compared to industry where the ore would enter a hot environment. It would be thus interesting to perform some tests at the maximum heating rate allowed by the reactors used in this work. This study could help when a more precise model of the fluidized bed reactor is developed.

- Study the effect of hydrodynamics on the calcination of the ore through the modeling of a more precise fluidized bed reactor.

The model of the fluidized bed reactor developed in this work was made for conditions close to minimum fluidization conditions. Such conditions imply that small bubbles circulate through the dense bed and thus kinetics can be better studied by limiting the effect of hydrodynamics in the bed. Nonetheless, bubble size is also affected by the reactor's dimensions, and in industrial scale reactors hydrodynamics will affect the calcination process. Thus, an industrial fluidized bed reactor that accounts for the hydrodynamics could be modeled. The model could allow at the same time the reactor design and by extension the cost estimation.

A comparison between using a single fluidized bed reactor or multiple reactors in series could also be done to evaluate energy consumption and cost estimation [145].

- Estimate the attrition of particles in a fluidized bed reactor.

As it was mentioned in Chapter 7, the particle size remained constant during the calcination of the rare earth ore at minimum fluidization conditions. As in the previous recommendation, when at industrial scale, fluidization does not take place at minimum fluidization velocity but at higher gas velocity, i.e. bubbling regime. In such case particles tend to break, reducing the particle size and increasing the entrainment into the freeboard. If such attrition takes place in this process, it should also be introduced in the industrial fluidized bed reactor model.

- Capture the CO_2 produced during calcination of the rare earth bearing ore.

Nowadays, climate change caused by CO_2 emissions is a big concern and a limitation for processes such as the one of this work whose emissions are caused by the decomposition of carbonatite minerals. On that regard, several studies of CO_2 capture exist and some of them focus on the capture with calcium phases, e.g. CaO.

In this process composed of calcination and acid leaching, most of calcium (above 90 wt.%) is found in the aqueous phase hindering CO_2 capture. Nonetheless, there are several studies regarding CO_2 capture with calcium hydroxide. The latter could thus be produced by neutralizing the acid solution.

- Complete the downstream process for the extraction of rare earth elements.

In this work rare earth elements were enriched to a rare earth oxide concentration of 7 wt.%. The process should continue to produce a high concentrate rare earth oxide. Once the process is complete a cost estimation could be performed to evaluate the feasibility of the process in an industrial scale. Otherwise, calcination is not comparable to the conventional process, since the downstream process (acids and conditions) is completely modified.

REFERENCES

1. Gupta, C.K. and N. Krishnamurthy, *Extractive Metallurgy of Rare Earths*. 2004.
2. Farrokhpay, S., *The significance of froth stability in mineral flotation — A review.* Advances in Colloid and Interface Science, 2011. **166**(1-2): p. 1-7.
3. Jordens, A., Y.P. Cheng, and K.E. Waters, *A review of the beneficiation of rare earth element bearing minerals.* Minerals Engineering, 2013. **41**: p. 97-114.
4. Chelgani, S.C., et al., *A review of rare earth minerals flotation: Monazite and xenotime.* International Journal of Mining Science and Technology, 2015. **25**(6): p. 877-883.
5. Jordens, A., et al., *Surface chemistry considerations in the flotation of bastnäsite.* Minerals Engineering, 2014. **66-68**: p. 119-129.
6. International Atomic Energy Agency, I., *Radiation Protection and NORM Residue Management in the Production of Rare Earths from Thorium-Containing Minerals*. 2011, International Atomic Energy Agency: Vienna, Austria.
7. Weng, Z.H., et al., *Assessing rare earth element mineral deposit types and links to environmental impacts.* Applied Earth Science, 2013. **122**(2): p. 83-96.
8. Chen, Y., et al., *A review of non-conventional metals extracting technologies from ore and waste.* International Journal of Mineral Processing, 2011. **98**(1-2): p. 1-7.
9. Wu, W.Y., et al., *Reaction process of monazite and bastnaesite mixed rare earth minerals calcined by CaO-NaCl-CaCl2.* Transactions of Nonferrous Metals Society of China, 2007. **17**(4): p. 864-868.
10. Yuan, S., et al., *Roasting decomposition of mixed rare earth tailings by CaO in reducing atmosphere.* Rare Metals, 2014.
11. Hikichi, Y., T. Ota, and T. Hattori, *Thermal mechanical and chemical properties of sintered monazite (La, Ce, Nd or Sm).* Mineralogical Journal, 1997. **19**(3): p. 123-130.
12. Xiang, J., et al., *Thermal decomposition behaviour of natural bastnasite crystal in calcination.* Transaction of NFsoc, 1994. **4**(4): p. 34-38.
13. Hikichi, Y., K.-i. Hukuo, and J. Shiokawa, *Solid State Reactions between Rare Earth Orthophosphate and Oxide.* Bulletin of the Chemical Society of Japan, 1980. **53**(5): p. 1455-1456.
14. Hikichi, Y. and T. Nomura, *Melting Temperatures of Monazite and Xenotime.* Journal of the American Ceramic Society, 1987. **70**(10): p. C-252-C-253.
15. Kumari, A., et al., *Thermal treatment for the separation of phosphate and recovery of rare earth metals (REMs) from Korean monazite.* Journal of Industrial and Engineering Chemistry, 2015. **21**: p. 696-703.
16. Sun, S., et al., *Effect of CaO on Fluorine in the Decomposition of REFCO3.* Journal of Rare Earths, 2007. **25**(4): p. 508-511.

17. Xue, B., et al., *Kinetics of Mixed Rare Earths Minerals Decomposed by CaO with NaCl-CaCl2 Melting Salt.* Journal of Rare Earths, 2010. **28**(Spec. Issue): p. 86.

18. Jones, A.P., F. Wall, and C.T. Williams, *Rare Earth Minerals: Chemistry, Origin and Deposits*, ed. C. Hall. 1996, London.

19. Simandl, G.J., *Geology and economic sifnificance of current and future rare earth element sources*, in *51st Annual Conference of Metallurgists* J.R. Goode, G.A. Moldoveanu, and M.S. Rayat, Editors. 2012: Niagara Falls.

20. Wang, S.J., *Rare Earth Metals: Resourcefulness and Recovery.* Jom, 2013. **65**(10): p. 1317-1320.

21. Jones, A.P., F. Wall, and C.T. Williams, *Rae Earth Minerals. Chemistry, origin and deposits* 1996.

22. Driscoll, M.O., *An Overview of Rare Earth Minerals Supply and Applications*, in *Materials Science Forum*. 1991. p. 409-420.

23. Zhang, J. and C. Edwards, *A Review of Rare Earth Mineral Processing Technology*, in *44th Annual Canadian Mineral Processors Operators Conference*. 2012: Ottawa, Ontario, Canada.

24. Kogel, J.E., et al., *Industrial Minerals & Rocks: Commodities, Markets and Uses*. 7th ed. 2006: Society for Mining, Metallurgy, and Exploration, Inc.

25. Goode, J.R., *Thorium and rare earth recovery in Canada: the first 30 years.* Canadian Metallurgical Quarterly, 2013. **52**(3): p. 234-242.

26. Rose, E.R., *Rare Earths of the Grenville Sub-Province, Ontario and Quebec*, G.S.o. Canada, Editor. 1960: Ottawa.

27. Gibson, M. and I. Parkinson, *Once Ignored on the Periodic Table, Don't Ignore them now-A Rare Earth Element Industry Review*. 2011, CIBC World Bank Inc.

28. Alon, J.C.C.L.I. and Y. He, *Reregulation of China's rare earth production and export.* International Journal of Emerging Markets, 2014. **9**(2): p. 236-256.

29. Zhang, L., et al., *Did China's rare earth export policies work? — Empirical evidence from USA and Japan.* Resources Policy, 2015. **43**: p. 82-90.

30. Brumme, A., *Market analysis of rare earth elements*, in *Wind Energy Deployment and the Relevance of the Rare Earths: An Economic Analysis*, S. Gabler, Editor. 2014. p. 17-48.

31. Han, A.P., J.P. Ge, and Y.L. Lei, *An adjustment in regulation policies and its effects on market supply: Game analysis for China's rare earths.* Resources Policy, 2015. **46**: p. 30-42.

32. Survey, U.S.G., *Mineral Commodity Summaries 2010*, U.S.D.o.t.I.U.S.G. Survey, Editor. 2010: Reston, Virginia, United States.

33. Survey, U.S.G., *Mineral Commodity Summaries 2011*, U.S.D.o.t.I.U.S.G. Survey, Editor. 2011: Reston, Virginia, United States.

34. Survey, U.S.G., *Mineral Commodity Summaries 2012*, U.S.D.o.t.I.U.S.G. Survey, Editor. 2012: Reston, Virginia, United States.

35. Survey, U.S.G., *Mineral Commodity Summaries 2013*, U.S.D.o.t.I.U.S.G. Survey, Editor. 2013: Reston, Virginia, United States.

36. Survey, U.S.G., *Mineral Commodity Summaries 2014*, U.S.D.o.t.I.U.S.G. Survey, Editor. 2014: Reston, Virginia, United States.

37. Survey, U.S.G., *Mineral Commodity Summaries 2015*, U.S.D.o.t.I.U.S.G. Survey, Editor. 2015: Reston, Virginia, United States.

38. Survey, U.S.G., *Mineral Commodity Summaries 2016*, U.S.D.o.t.I.U.S.G. Survey, Editor. 2016: Reston, Virginia, United States.

39. Sternberg, J., *How the great rare-earth metals crisis vanished*, in *Wall Street Journal*. January 2014.

40. London, I.M., et al., *Rare Earth Elements*. Conference of metallurgists (COM) hosted by MS&T'13, ed. I.M. London, et al. 2013, Montreal, Quebec: Met Soc.

41. Goode, J.R., G. Moldoveanu, and M.S. Rayat, *RARE EARTHS 2012*. 51st Annual Conference of Metallurgists, COM, ed. J.R. Goode, G. Moldoveanu, and M.S. Rayat. 2012, Niagara Falls: Met Soc.

42. Golev, A., et al., *Rare earths supply chains: Current status, constraints and opportunities.* Resources Policy, 2014. **41**: p. 52-59.

43. DOE, *Critical Materials strategy*, U.S.D.o. Energy, Editor. December 2011.

44. Schlinkert, D. and K.G. van den Boogaart, *The development of the market for rare earth elements: Insights from economic theory.* Resources Policy, 2015. **46**: p. 272-280.

45. Xie, F., et al., *A critical review on solvent extraction of rare earths from aqueous solutions.* Minerals Engineering, 2014. **56**: p. 10-28.

46. Carron, M.K., D.L. Skinner, and R.E. Stevens, *Determination of thorium and of rare earth elements in cerium earth minerals and ores.* Analytical Chemistry, 1955. **27**: p. 1058-1061.

47. Giacalone, J.A., *The Market For The "Not-So-Rare" Rare Earth Elements* Journal of International Energy Policy, 2012. **1**: p. 11-18.

48. Ault, T., S. Krahn, and A. Croff, *Radiological Impacts and Regulation of Rare Earth Elements in Non-Nuclear Energy Production.* Energies, 2015. **8**(3): p. 2066-2081.

49. Humphries, M., *Rare Earth Elements: The Global Supply Chain*, C. U.S. Congressional Research Service, Editor. 2010.

50. DOE, *Critical Materials strategy*, U.S.D.o. Energy, Editor. 2015.

51. Binnemans, K., et al., *Recycling of rare earths: a critical review.* Journal of Cleaner Production, 2013. **51**: p. 1-22.

52. Meyer, L. and B. Bras, *Rare Earth Metal Recycling.* 2011 Ieee International Symposium on Sustainable Systems and Technology (Issst), 2011.

53. Jaireth, S., D.M. Hoatson, and Y. Miezitis, *Geological setting and resources of the major rare-earth-element deposits in Australia.* Ore Geology Reviews, 2014. **62**: p. 72-128.

54. Grenier, L. and J.F. Tremblay, *NI 43-101 Technical report, Surface diamond drilling exploration program for rare earth elements*. 2013, IAMGOLD Corporation.

55. Hou, Z., et al., *The Himalayan Mianning–Dechang REE belt associated with carbonatite–alkaline complexes, eastern Indo-Asian collision zone, SW China.* Ore Geology Reviews, 2009. **36**(1-3): p. 65-89.

56. Orris, G.J. and R.I. Grauch, *Rare Earth Element Mines, Deposits, and Occurrences*, U.S.G.S. USGS and U.S.D.o.t. Interior, Editors. 2002: Reston, VA, USA.

57. Weng, Z., et al., *A Detailed Assessment of Global Rare Earth Element Resources: Opportunities and Challenges.* Economic Geology, 2015. **110**(8): p. 1925-1952.

58. London, I.M., G.P. Hatch, and B. Davis, *Significant strides toward REE production in Canada*, in *53rd Annual Conference of Metallurgists*. 2014, Canadian Institute of Mining, Metallurgy and Petroleum: Vancouver.

59. Hatch, G.P. *TMR Advanced Rare-Earth Projects Index*. 2015 July 13 2016].

60. Moustafa, M.I. and N.A. Abdelfattah, *Physical and Chemical Beneficiation of the Egyptian Beach Monazite.* Resource Geology, 2010. **60**(3): p. 288-299.

61. Xiong, W., et al., *Flotation-magnetic separation for the beneficiation of rare earth ores.* Minerals Engineering, 2018. **119**: p. 49-56.

62. Cheng, J., Y. Hou, and L. Che, *Flotation separation on rare earth minerals and gangues.* Journal of Rare Earths, 2007. **25**: p. 62-66.

63. Fang, J. and D. Zhao, *Separation of rare earth from tails of magnetite separation in Bao Steel's concentrator.* Metal Mine, 2003. **321**: p. 47-49.

64. Kumari, A., et al., *Process development to recover rare earth metals from monazite mineral: A review.* Minerals Engineering, 2015. **79**: p. 102-115.

65. Gupta, C.K. and N. Krishnamurthy, *Extractive Metallurgy of Rare-Earths.* International Materials Reviews, 1992. **37**(5): p. 197-248.

66. Kelly, E.G. and D.J. Spottiswood, *The theory of electrostatic separations: a review – Part I. Fundamentals.* Minerals Engineering, 1989. **2**(1): p. 33-46.

67. Navarro, J. and F. Zhao, *Life-Cycle Assessment of the Production of Rare-Earth Elements for Energy Applications: A Review.* Frontiers in Energy Research, 2014. **2**.

68. Habashi, F., *Extractive metallurgy of rare earths.* Canadian Metallurgical Quarterly, 2013. **52**(3): p. 224-233.

69. Sadri, F., A.M. Nazari, and A. Ghahreman, *A review on the cracking, baking and leaching processes of rare earth element concentrates.* Journal of Rare Earths, 2017. **35**(8): p. 739-752.

70. Zhu, Z.W., Y. Pranolo, and C.Y. Cheng, *Separation of uranium and thorium from rare earths for rare earth production - A review.* Minerals Engineering, 2015. **77**: p. 185-196.

71. Cox, J.J., et al., *Technical Report on the Eco Ridge Mine Project, Elliot Lake Area, Ontario, Canada*, R.P.A. Inc., Editor. 2012: Toronto, Ontario.

72. Goode, J.R., et al., *The recovery of rare earths, uranium and pyrite from Pele Mountains proposed Eco Ridge Mine Project*, in *Conference of Metallurgists Proceedings*. 2014, Canadian Institute of Mining, Metallurgy and Petroleum: Vancouver.

73. Hadley, T. and E. Catovic, *Beneficiation and extraction of REE from northern mineral's browns range heavy rare earth project*, in *Conference of Metallurgists Proceedings* 2014, Canadian Institute of Mining, Metallurgy and Petroleum: Vancouver.

74. Kul, M., Y. Topkaya, and I. Karakaya, *Rare earth double sulfates from pre-concentrated bastnasite.* Hydrometallurgy, 2008. **93**(3-4): p. 129-135.

75. Vijayalakshmi, R., et al., *Processing of xenotime concentrate by sulphuric acid digestion and selective thorium precipitation for separation of rare earths.* Hydrometallurgy, 2001. **61**(2): p. 75-80.

76. Ball, R.W., *Extraction of rare eath from monazite sand and rare earth residue*, in *Department of Chemistry*. 1927, University of British Columbia.

77. Abreu, R.D. and C.A. Morais, *Purification of rare earth elements from monazite sulphuric acid leach liquor and the production of high-purity ceric oxide.* Minerals Engineering, 2010. **23**(6): p. 536-540.

78. Crouse, D.J. and K.B. Brown, *Recovery of thorium, uranium and rare earths from monazite sulfate liquors by the amine extraction (AMEX) process*, U.S.A.E. Commission, Editor. 1959, Oak Ridge National Laboratory.

79. Gomes, J.C.C., et al., *Leaching process of cerium extraction from mixture of cerite-monazite mineral.* Advanced Materials Forum Iii, Pts 1 and 2, 2006. **514-516**: p. 1653-1657.

80. Kim, E. and K. Osseo-Asare, *Aqueous stability of thorium and rare earth metals in monazite hydrometallurgy: Eh-pH diagrams for the systems Th-, Ce-, La-, Nd- (PO4)-(SO4)-H2O at 25 degrees C.* Hydrometallurgy, 2012. **113**: p. 67-78.

81. Li, M., et al., *Mixed rare earth concentrate leaching with HCl-AlCl3 solution.* Rare Metals, 2013. **32**(3): p. 312-317.

82. Zou, D., J. Chen, and D.Q. Li, *Separation chemistry and clean technique of cerium(IV): A review.* Journal of Rare Earths, 2014. **32**(8): p. 681-685.

83. Alex, P., A.K. Suri, and C.K. Gupta, *Processing of xenotime concentrate.* Hydrometallurgy, 1998. **50**: p. 331–338.

84. Amaral, J.C.B.S. and C.A. Morais, *Thorium and uranium extraction from rare earth elements in monazite sulfuric acid liquor through solvent extraction.* Minerals Engineering, 2010. **23**(6): p. 498-503.

85. de Vasconcellos, M.E., C.A.d.S. Queiroz, and A.d. Abrão, *Sequential separation of the yttrium—heavy rare earths by fractional hydroxide precipitation.* Journal of Alloys and Compounds, 2004. **374**(1-2): p. 405-407.

86. Rice, A.C., *Preparation of rare-earth chloride solutions*. 1959: U.S. Dept. of the Interior, Bureau of Mines.

87. Zhu, G., et al., *Chlorination kinetics of fluorine-fixed rare earth concentrate.* Minerals Engineering, 2003. **16**(7): p. 671-674.

88. Huang, X.W., et al., *Technology development for rare earth cleaner hydrometallurgy in China.* Rare Metals, 2015. **34**(4): p. 215-222.

89. Wang, L.S., et al., *Toward greener comprehensive utilization of bastnaesite: Simultaneous recovery of cerium, fluorine, and thorium from bastnaesite leach liquor using HEH(EHP).* Chemical Engineering Journal, 2013. **215**: p. 162-167.

90. Borra, C.R., et al., *Leaching of rare earths from bauxite residue (red mud).* Minerals Engineering, 2015. **76**: p. 20-27.

91. Ochsenkuhn-Petropulu, M., et al., *Pilot-Plant Investigation of the Leaching Process for the Recovery of Scandium from Red Mud.* Ind. Eng. Chem. Res., 2002. **41**: p. 5794-5801.

92. Ochsenkuhn-Petropulu, M., et al., *Recovery of lanthanides and yttrium from red mud by selective leaching.* Analytica Chimica Acta, 1996. **319**: p. 249-254.

93. Srnirnov, D.I. and T.V. Molchanova, *The investigation of sulphuric acid sorption recovery of scandium and uranium from the red mud of alumina production.* Hydrometallurgy, 1997. **45**: p. 249-259.

94. Li, H., et al., *A new hydrometallurgical process for extracting rare earths from apatite using solvent extraction with P350.* Journal of Alloys and Compounds, 2006. **408-412**: p. 995-998.

95. Monir, M.A. and A.M. Nabawia, *Recovery of lanthanides from Abu Tartur phosphate rock, Egypt.* Hydrometallurgy, 1999. **52**: p. 199-206.

96. Abdel-Rehim, A.M., *An innovative method for processing Egyptian monazite.* Hydrometallurgy, 2002. **67**(1-3): p. 9-17.

97. Alex, P., R.C. Hubli, and A.K. Suri, *Processing of rare earth concentrates.* Rare Metals, 2005. **24**(3): p. 210-215.

98. Amer, T.E., et al., *A suggested alternative procedure for processing of monazite mineral concentrate.* International Journal of Mineral Processing, 2013. **125**: p. 106-111.

99. Chi, R., et al., *Recovery of rare earth from bastnasite by ammonium chloride roasting with fluorine deactivation.* Minerals Engineering, 2004. **17**(9-10): p. 1037-1043.

100. de Vasconcellos, M.E., et al., *Enrichment of yttrium from rare earth concentrate by ammonium carbonate leaching and peroxide precipitation.* Journal of Alloys and Compounds, 2006. **418**(1-2): p. 200-203.

101. El-Nadi, Y.A., J.A. Daoud, and H.F. Aly, *Modified leaching and extraction of uranium from hydrous oxide cake of Egyptian monazite.* International Journal of Mineral Processing, 2005. **76**(1-2): p. 101-110.

102. Han, K.N., et al., *Opportunities and challenges for treating rare-earth elements.* Geosystem Engineering, 2014. **17**(3): p. 178-194.

103. Kuzmin, V.I., et al., *Combined approaches for comprehensive processing of rare earth metal ores.* Hydrometallurgy, 2012. **129**: p. 1-6.

104. Moldoveanu, G.A. and V.G. Papangelakis, *Recovery of rare earth elements adsorbed on clay minerals: I. Desorption mechanism.* Hydrometallurgy, 2012. **117**: p. 71-78.

105. Moldoveanu, G.A. and V.G. Papangelakis, *Recovery of rare earth elements adsorbed on clay minerals: II. Leaching with ammonium sulfate.* Hydrometallurgy, 2013. **131**: p. 158-166.

106. Panda, R., et al., *Leaching of rare earth metals (REMs) from Korean monazite concentrate.* Journal of Industrial and Engineering Chemistry, 2014. **20**(4): p. 2035-2042.

107. Tian, J., et al., *Process optimization on leaching of a lean weathered crust elution-deposited rare earth ores.* International Journal of Mineral Processing, 2013. **119**: p. 83-88.

108. Xu, Y.H., et al., *Decomposition of bastnasite and monazite mixed rare earth minerals calcined by alkali liquid.* Journal of Rare Earths, 2012. **30**(2): p. 155-158.

109. Järvinen, O., et al., *Method and Device for Treating Anode Slime*. 2006: Finland.

110. Masun, K.M., I.C. Weir, and J.R. Goode, *TECHNICAL REPORT ON THE FOXTROT PROJECT, NEWFOUNDLAND & LABRADOR, CANADA*. 2016: Toronto, ON, Canada.

111. Chi, R., et al., *Preparation of enriched cerium oxide from bastnasite with hydrochloric acid by two-step leaching.* Metallurgical and Materials Transactions B-Process Metallurgy and Materials Processing Science, 2006. **37**(2): p. 155-160.

112. Clarke, F.W. and H.S. Washington, *The composition of the earth's crust*. 1924, United States Geological Survey (USGS): Washington.

113. Criado, J.M. and A. Ortega, *A study of the influence of particle size on the thermal decomposition of CaCO3 by means of constant rate thermal analysis.* Thermochimica Acta, 1992. **195**: p. 163-167.

114. Földvári, M., *Handbook of thermogravimetric system of minerals and its use in geological practice*, ed. G.I.o. Hungary. Vol. 213. 2011, Budapest.

115. Reller, A., et al., *Thermochemical Reactivity of Metal Carbonates.* Chimia, 1991. **45**: p. 262-266.

116. Guentner, J., et al., *Recovery of rare earth elements from complex raw materials by Outotec's Solutions*, in *IMPC 2016: XXVIII International Mineral Processing Congress Proceedings*. 2016: Quebec City.

117. Xing, P.F., et al., *High temperature dephosphorization behavior of monazite concentrate with charred coal.* Transactions of Nonferrous Metals Society of China, 2010. **20**(12): p. 2392-2396.

118. Xu, Y., et al., *Decomposition of bastnasite and monazite mixed rare earth minerals calcined by alkali liquid.* Journal of Rare Earths, 2012. **30**: p. 155.

119. Brugger, W. and H. Greinacher, *A cracking process for rare earth ores by direct chlorination at high temperature on a ptoduction scale.* J. Metals, 1967. **19**(12): p. 32-35.

120. Zhang, J. and C. Edwards, *Mineral decomposition and leaching processes for treating rare earth ore concentrate,* in *51th Annual conference of metallurgists, COM*, J.R. Goode, G. Moldoveanu, and M.S. Rayat, Editors. 2012: Niagara falls, Ontario.

121. Wang, L., et al., *Towards cleaner production of rare earth elements from bastnaesite in China.* Journal of Cleaner Production, 2017. **165**: p. 231-242.

122. Wang, L., et al., *Recovery of fluorine from bastnasite as synthetic cryolite by-product.* J Hazard Mater, 2012. **209-210**: p. 77-83.

123. Hartley, F.R., *The preparation of anhydrous lanthanon chlorides by high-temperature chlorination of monazite.* Journal of Applied Chemistry, 2007. **2**(1): p. 24-31.

124. Merritt, R.R., *High temperature methods for processing monazite: I. Reaction with calcium chloride and calcium carbonate.* Journal of the Less Common Metals, 1990. **166**(2): p. 197-210.

125. Merritt, R.R., *High temperature methods for processing monazite: II. Reaction with sodium carbonate.* Journal of the Less Common Metals, 1990. **166**(2): p. 211-219.

126. Wu, W.-y., et al., *Reaction process of monazite and bastnaesite mixed rare earth minerals calcined by CaO-NaCl-CaCl2.* Transactions of Nonferrous Metals Society of China, 2007. **17**(4): p. 864-868.

127. Huang, Y., et al., *Leaching kinetics of rare earth elements and fluoride from mixed rare earth concentrate after roasting with calcium hydroxide and sodium hydroxide.* Hydrometallurgy, 2017. **173**: p. 15-21.

128. Hajiani, P., *Significant reduction in hydrochloric acid consumption in rare earth extraction from ferrocarbonatite (Montviel Project),* in *IMPC 2016: XXVIII International Mineral Processing Congress Proceedings*. 2016: Quebec City.

129. Vyazovkin, S., et al., *ICTAC Kinetics Committee recommendations for performing kinetic computations on thermal analysis data.* Thermochimica Acta, 2011. **520**(1-2): p. 1-19.

130. Blecic, D. and Z.D. Zivkovic, *A new method for the determination of reaction kinetics from DTA and TG curves. Part II. Application of the method of the thermal decomposition of carbonates.* Thermochimica Acta, 1983. **60**: p. 69-76.

131. Brown, M.E., et al., *Computational aspects of kinetic analysis. Part A: The ICTAC kinetics project-data, methods and results.* Thermochimica Acta, 2000. **355**: p. 125-143.

132. Kissinger, H.E., *Reaction Kinetics in Differential Thermal Analysis.* Analytical Chemistry, 1957. **29**(11): p. 1702-1706.

133. Maciejewski, M., *Computational aspects of kinetic analysis. Part B: The ICTAC Kinetics Project — the decomposition kinetics of calcium carbonate revisited, or some tips on survival in the kinetic minefield.* Thermochimica Acta, 2000. **355**: p. 145-154.

134. Ayodele, B.V., et al., *Non-isothermal kinetics and mechanistic study of thermal decomposition of light rare earth metal nitrate hydrates using thermogravimetric analysis.* Journal of Thermal Analysis and Calorimetry, 2016. **125**(1): p. 423-435.

135. Ramukutty, S. and E. Ramachandran, *Reaction Rate Models for the Thermal Decomposition of Ibuprofen Crystals* Journal of Crystallization Process and Technology, 2014. **4**: p. 71-78.

136. Farag, S., L. Kouisni, and J. Chaouki, *Lumped Approach in Kinetic Modeling of Microwave Pyrolysis of Kraft Lignin.* Energy & Fuels, 2014. **28**(2): p. 1406-1417.

137. Khawam, A. and D.R. Flanagan, *Solid-state kinetic models: Basics and mathematical fundamentals.* Journal of Physical Chemistry B, 2006. **110**(35): p. 17315-17328.

138. Dhupe, A.P. and A.N. Gokarn, *Studies in the thermal decomposition of natural siderites in the presence of air.* International Journal of Mineral Processing, 1990. **28**(3-4): p. 209-220.

139. Jagtap, S.B., A.R. Pande, and A.N. Gokarn, *Kinetics of thermal decomposition of siderite: effect of particle size.* International Journal of Mineral Processing, 1992. **36**(1-2): p. 113-124.

140. Britton, H.T.S., S.J. Gregg, and G.W. Winsor, *The calcination of dolomite. Part II.- The thermal decomposition of dolomite.* Trans. Faraday Soc., 1952. **48**: p. 63-69.

141. Escardino, A., J. Garcia-Ten, and C. Feliu, *Kinetic study of calcite particle (powder) thermal decomposition: Part I.* Journal of the European Ceramic Society, 2008. **28**(16): p. 3011-3020.

142. Britton, H.T.S., S.J. Gregg, and G.W. Winsor, *The calcination of dolomite. Part I.—The kinetics of the thermal decomposition of calcite and of magnesite.* Trans. Faraday Soc., 1952.

143. Zhao, L., et al., *Thermal decomposition and oxidation of bastnaesite concentrate in inert and oxidative atmosphere.* Journal of Rare Earths, 2018. **36**(7): p. 758-764.

144. Samih, S., et al., *From complex feedstocks to new processes: The role of the newly developed micro-reactors.* Chemical Engineering and Processing - Process Intensification, 2018. **131**: p. 92-105.

145. Kunii, D. and O. Levenspiel, *Fluidization Engineering*. 1991, Boston.

APPENDIX A HEAT TRANSFER MODEL IN TGA APPLIED ON CARBONATE MINERALS

A.1. HEAT TRANSFER MODEL FOR CORRECTION OF SAMPLE TEMPERATURE IN TGA

Prior to elaborate experimental data as for development of calcination kinetics, a correction of the temperature measured by TGA is necessary. In fact, during a TGA test, the thermocouple is positioned below the sample holder, thus measuring the temperature of the platinum pan. Due to heat transfer between the pan and the sample (Figure A. 1), there is a difference between the measured temperature and the sample temperature. A heat transfer model study was therefore necessary to evaluate the sample temperature during decomposition of each mineral. Odile et al. 2015 describe the heat transfer model occurring in TGA equipment with more details [42].

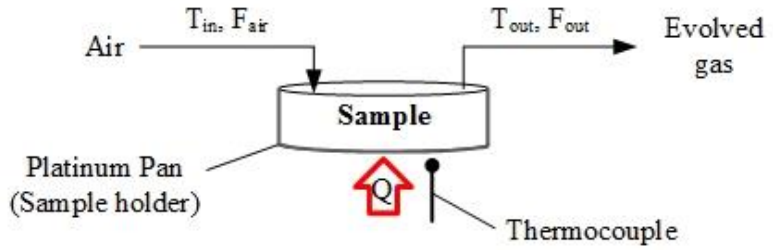

Figure A. 1 TGA schematic for heat transfer model.

The heat transfer model in the TGA system can be expressed as in Eq. A.1.

$$F_{air}C_{p,air}(T_{in} - T_{out}) + US(T_F - T_S) = mC_{p,sample}\frac{dT_s}{dt} - H_{r,i}\frac{dm}{dt} \quad [A.1]$$

Where F_{air} stands for the air mass flow rate (kg/s), $C_{p,air}$ is the heat capacity of air (J/(kg K)), T_{in} and T_{out} are the gas temperatures at the inlet and outlet of the TGA (K) (these can be assumed as the furnace temperature and the sample temperature, respectively), U is the global heat transfer coefficient (W/(m^2 K)), S is the surface at the bottom of the pan which has a 1 cm diameter ($7.85 \cdot 10^{-5}$m^2), T_F is the furnace temperature (K), T_S is the sample temperature (K), m is the sample mass (kg) which is measured by the TGA, $C_{p,sample}$ is the heat capacity of the sample (J/(kg K)), and $H_{r,i}$ is the heat of decomposition for a given mineral i (J/(kg)).

Due to the many variables affected by the temperature, as a simplification, all thermal parameters, i.e. heat capacities and thermal conductivities, of the solids and gaseous compounds were considered as constants. However, heat capacity and thermal conductivity of the sample change throughout the reaction (Eq. A.1 & A.2).

$$C_{p,sample} = (1-\propto)C_{p,mineral} + \propto C_{p,product} \quad [A.2]$$

Where α is the conversion of the decomposition, and $C_{p,mineral}$ and $C_{p,product}$ are respectively the heat capacities of the mineral and the oxide resulting from the reaction (J/(kg K)). Thermal conductivity behaves similar to the heat capacity:

$$k_{sample} = (1-\propto)k_{mineral} + \propto k_{product} \quad [A.3]$$

Since the global heat transfer coefficient estimates the conduction of heat through the pan and the sample, it can be estimated as described in Eq. A.4. This coefficient will vary through the test due to a change in the heat conduction coefficient of the sample that evolves with conversion.

$$U = \frac{1}{\frac{e_{pan}}{k_{pan}} + \frac{e_{sample}}{k_{sample}}} \quad [A.4]$$

Where e_{pan} and k_{pan} are thickness ($2 \cdot 10^{-4}$m) and the thermal conductivity of the platinum pan (72 W/ (m K)), and e_{sample} is the sample thickness that can be simplified as the height of the pan (10^{-3}m).

Thermal properties of minerals and their respective products are given in Table A. 1.

Table A. 1 Heat transfer parameters for carbonate minerals and their decomposition products

	Minerals				Products					
	Calcite	Dolomite	Siderite	Bastnaesite	CaO	MgO	Fe_2O_3	CeO_2	RE_2O_3 [a]	REF_3 [b]
Cp (J/(kg K))	814	920	683	614.7	976	923	938	425	332	523
Hr (kJ/kg)	1830	1180	1100	1630 [c]	-	-	-	-	-	-
k_j (W/(m K))	3.57	5.50	3	3	0.3	0.3	11.1	6.1	2.5	5.1
Ref.	[43-48]			[49, 50]	[44-46]			[51-55]		[49, 56]

[a] Thermal parameter for RE_2O_3 are the average value of the parameter for La and Nd oxides (III)
[b] Thermal parameter for REF_3 are an average value for La, Ce and Nd
[c] Calculated from the enthalpies of formation and the elemental composition of bastnaesite and its respective oxides and fluorides used in this research

A.2. HEAT TRANSFER MODELING RESULTS

Figure A. 2 illustrates TGA calcination curves of each mineral before and after correction of sample temperature, i.e. T_F (measured furnace temperature by thermocouple) versus T_S (corrected sample temperature).

Due to specific thermal properties of each mineral and its respective oxide products, the temperature gradient between the furnace and the sample temperature differs for each mineral; the gradient is more evident for alkaline metal carbonates such as calcite and dolomite than for other carbonate minerals.

Also, for a given mineral, difference between T_S and T_F increased for higher heating rates. For instance, in the case of calcite, the temperature gradient between T_S and T_F at the heating rate of 5 ºC/min varied between 1.2 and 6.5 ºC, whereas it varied from 4.9 to 25.2 ºC at the 20 ºC/min heating rate that is quite significant. This effect was also observed for other minerals of this study.

This analysis proves that a correction of sample temperature is necessary prior to develop a kinetic model unless otherwise the impact of erroneous kinetic parameters would propagate in design of a large-scale calcination reactor.

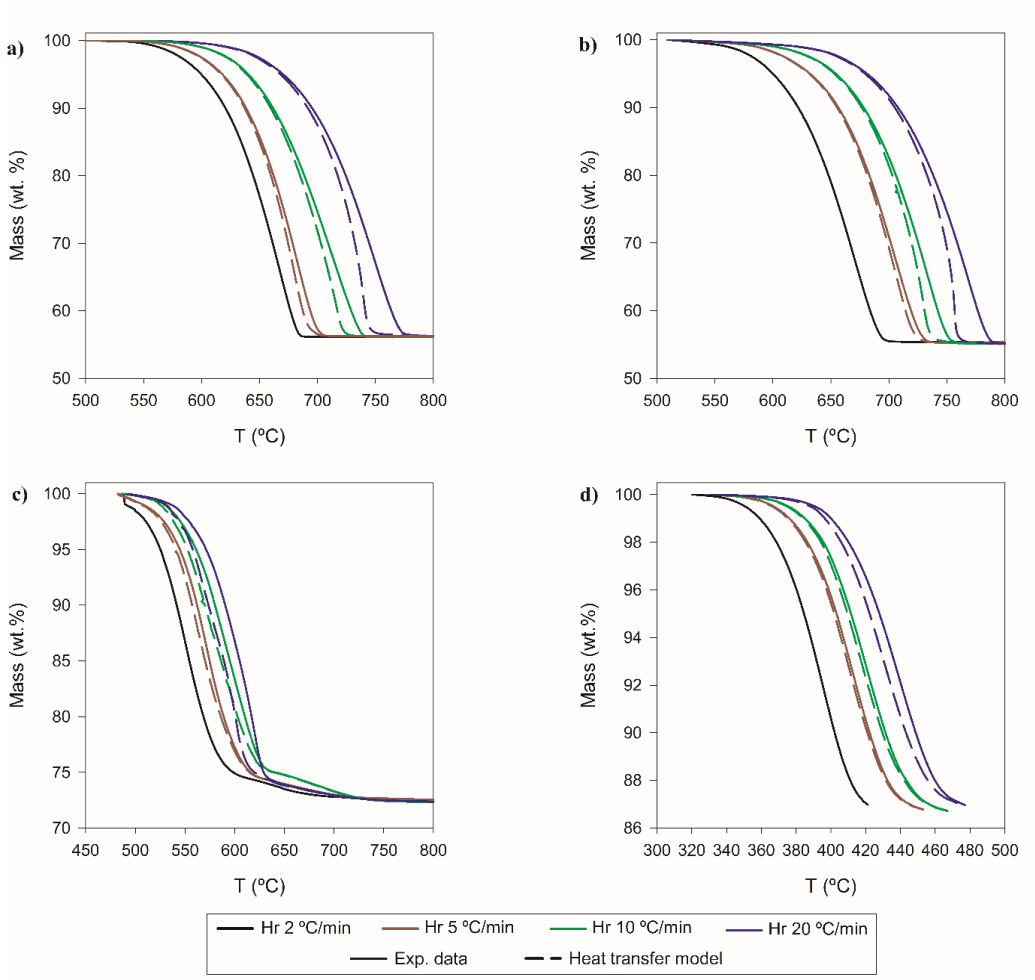

Figure A. 2 Comparison experimental and heat transfer model TG curves for:

a) Calcite; b) Dolomite; c) Siderite; d) Bastnaesite.

APPENDIX B EFFECT OF THE PURGE GAS FLOW RATE ON THE CALCINATION OF CALCITE

The importance of the gas purge flow rate (N_2) for the evacuation of CO_2 produced during calcination was evaluated in this research to ensure its fast release from the system (Figure B. 1) [19, 20]. When the flow rate of the purge gas in the TGA system is below 40 ml/min, there is a clear shift of the decomposition of calcite to higher temperatures, indicating that the CO_2 needs more time to diffusion outside of the particles, thus increasing the partial pressure of the gas inside the particles, which causes a reverse reaction of CO_2 with the oxide. This phenomenon surely affects the kinetics of calcination of the mineral.

However, when the purge flow rate is set at 40 ml/min or higher (e.g. 60 and 80 ml/min), the thermograms at these conditions are similar, indicating that the CO2 is rapidly purged from the particles, limiting the reversibility reaction and thus reducing the effect of CO2 on the kinetics.

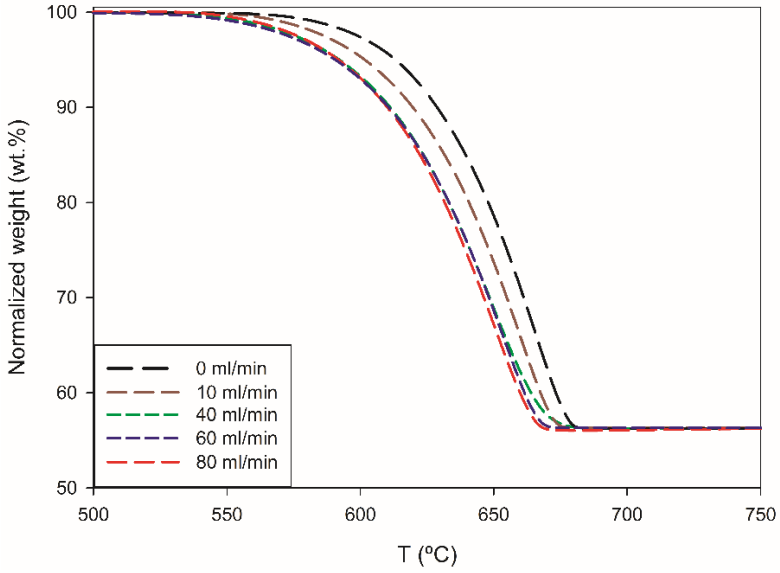

Figure B. 1 Calcination of calcite at various flow rates of the nitrogen purge gas

APPENDIX C CONTOUR MAP OF THE KINETIC PARAMETERS FOR CARBONATE MINERALS

Contour maps for the validation of the kinetic models by evaluating the kinetic parameters were developed according to the RSS (Eq. 3) and equations C.1 and C.2 [24].

$$Obj = \frac{1}{N-p}\sum\left(\left(\frac{d\alpha}{dt}\right)_{exp} - \left(\frac{d\alpha}{dt}\right)_{calc}\right)^2 \quad [C.1]$$

$$Dev\ (\%) = \sqrt{Obj} \cdot 100 \quad [C.2]$$

Figure C. 1 illustrates the contour map for the carbonate minerals.

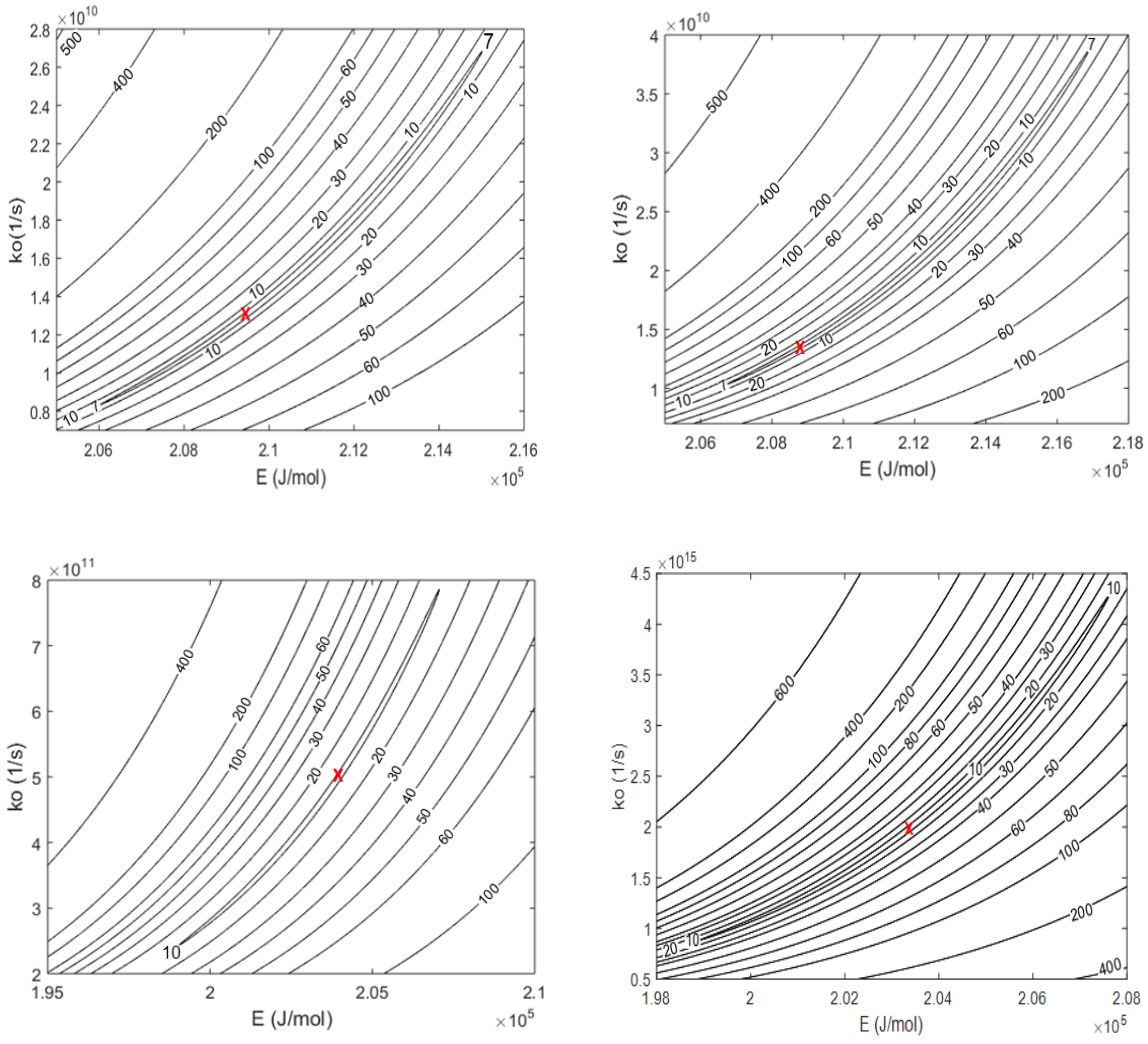

Figure C. 1 Contour maps (k0, Ea, Deviation) for the kinetic validation of carbonate minerals: a) Calcite; b) Dolomite; c) Siderite; d) Bastnaesite (the red mark represents the kinetic data from this article)

APPENDIX D KINETIC MODELING FOR THE CALCINATION OF PURE MINERALS

D.1. KINETIC MODELING COMPUTATIONAL ANALYSIS

Kinetics of pure minerals was developed by following a previous study on the calcination kinetics of carbonate minerals [36]. That work showed that differential fitting methodology, that uses all kinetic parameters as variables, i.e. reaction mechanism [37, 38], activation energy and pre-exponential factor, was effective to develop a kinetic study with high accuracy. Therefore, the differential fitting methodology was used in this research to study of the mineral kinetics.

When a mineral presented a multiple decomposition steps, each step was evaluated individually and were then combined to reproduce the overall kinetic model for the decomposition of the mineral

From the reaction rate definition (Equations D.1 & D.2), it was possible to develop the equation used for the kinetic model study by differential fitting method (Equation D.3).

$$\frac{d\alpha}{dt} = k_0^* \, e^{\left(-\frac{E_a}{R}\left(\frac{1}{T}-\frac{1}{T_r}\right)\right)} f(\alpha) \qquad [D.1]$$

$$\alpha = \frac{m_0 - m_i}{m_0 - m_f} \qquad [D.2]$$

$$ln\left(\frac{d\alpha/dt}{f(\alpha)}\right) = \ln(k_0^*) - \frac{E_a}{R}\left(\frac{1}{T}-\frac{1}{T_r}\right) \qquad [D.3]$$

Where α is defined as the conversion, expressed as a function of the decomposition mass loss; $\frac{d\alpha}{dt}$ is the reaction rate; $f(\alpha)$ is the reaction mechanism; E_a is the activation energy (J/mol), R is the universal gas constant (J/mol K), T is the actual temperature of the sample (K), T_r is a reference temperature (K); and k_0^* is a representative of the pre-exponential factor in the form of $k_0^* = k_0 \, exp(-E_a/(RT_r))$, where k_0 is the pre-exponential factor (s^{-1}).

D.2. KINETIC MODELING OF PYRITE AND CHLORITE

D.2.1. PYRITE

Pyrite is an iron sulfide which calcination, as shown in the thermogram of Figure 6.1e, occurs in a two-step roasting. The decomposition started at 390 ºC and burnt 7.2 wt.% of the pyrite; while the second step started at 500 ºC and contributed with a 24.2 wt.% mass loss of pyrite.

The calcination process was characterized by in situ detection of the produced gases (Figure 6.1e) and by XRD to understand the ongoing reaction mechanism. Figure D. 3a illustrates the diffractograms performed at each step of the roasting. The first step, as characterized by the diffractogram at 535 ºC of Figure D. 3, indicates the production of pyrrhotite. The production of pyrrhotite and iron sulfide II (FeS) can be explained through the oxidation at the surface of the particle (Reaction 6.8), while at same temperatures thermal decomposition takes place in the inner parts of the particle (Reaction 6.9). Then, the second step described the decomposition of the pyrrhotite and iron sulfide II to produce iron oxide III (Fe_2O_3), as detected in Figure D. 3a (Reaction 6.11 & 6.12). The presence of iron sulfide in the final product (Figure D. 3a) indicates the possibility of encapsulation of the iron sulfide II produced during thermal decomposition (Reaction 6.9). Despite disagreements in the literature regarding the reaction mechanism of pyrite's calcination, a mechanism similar to the one presented in this study has been reported [39-43]. Thereupon, pyrite's calcination under air conditions can be studied as a multiple step for iron oxide III production.

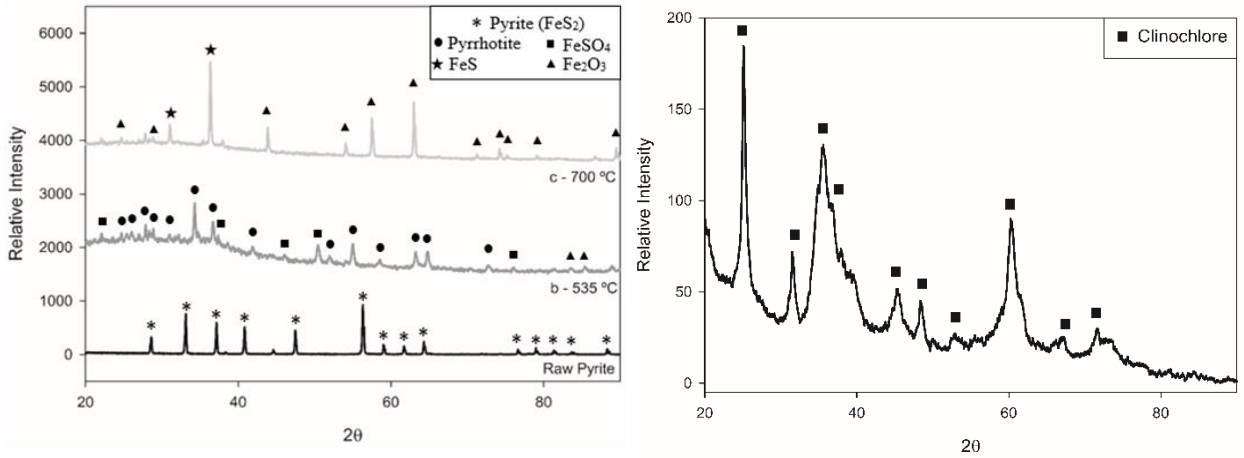

Figure D. 3 Diffractograms of minerals: a) Pyrite calcination; b) Clinochlore

The kinetics of each step were studied by differential model fitting and fitted the Mampel firt order reaction mechanism with an activation energy of 240.9 kJ/mol and 280.8 kJ/mol respectively. This mechanism often describes the presence of a crystallographic transition state, which could be due to the oxidation of iron oxide from iron oxide II to iron oxide III.

From the individual steps, a global model was developed for the calcination of pyrite under air atmosphere (Figure D. 4) by considering the intake of each step to the global roasting of the mineral (Equation D.4).

$$\left(\frac{d\alpha}{dt}\right)_{FeS2} = x_{s1}\left(Aexp\left(-\frac{E_a}{RT}\right)\right)_{Step1}(1-\alpha_1) + x_{s2}\left(Aexp\left(-\frac{E_a}{RT}\right)\right)_{Step2}(1-\alpha_2) \qquad [D.4]$$

Where x_{s1} and x_{s2} represent the fractional conversions of each step of pyrite decomposition, 23.9 and 76.1 % respectively; and α_1 and α_2 are the individual conversions for the first and second reaction respectively.

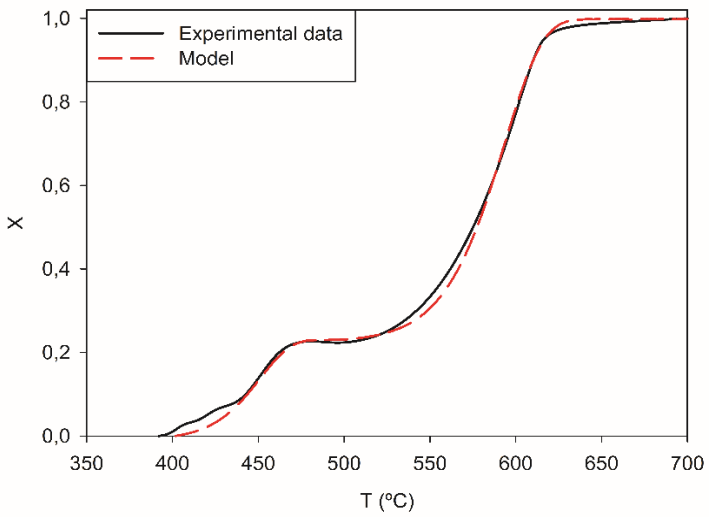

Figure D. 4 Kinetic model validation for the decomposition of pyrite under air atmosphere

D.2.2. CHLORITE - CLINOCHLORE

Chlorite represents a group of minerals whose thermal behavior is characterized by its dehydroxylation at high temperatures (above 400ºC). Due to the impossibility to discern which

kind of chlorite was present in the rare earth ore bearing mineral sample, clinochlore, one of the most common species of chlorite, was used in this study (Figure D. 3b).

The thermal study of this mineral (Figure 6.1f) confirmed the dehydroxylation that occurred in a two-step reaction. The first started at approximately 425 ºC with a 7.3 wt.% mass loss, and the second at around 675 ºC with a 1.42 wt.% of the mass loss. Other chlorite minerals studied in literature, e.g. lizardite or kaolinite, presented a similar thermal behavior, and their mass loss ranges from 4 wt.% to 9 wt.% [12, 44, 45].

Friedman's Isoconversional method was used to evaluate both steps (Figure D. 5) and proved clinochlore's calcination to be complex, since the activation energy changes all along the calcination. The complexity was explained by the constant change of structure and bounding of the mineral [44, 46, 47]. Thus, to simplify the modeling, the reaction was considered as a two-step, corresponding to the two plateaus represented in Figure D. 5. Accordingly, the first dehydroxylation was considered to last until approximately 680 ºC, corresponding to an overall conversion (α_2) of 0.85. The increasing trend at a conversion (α_1) of 0.72 indicates the start of the second reaction, thus characterizing an overlap of both stages between α_1 and α_2.

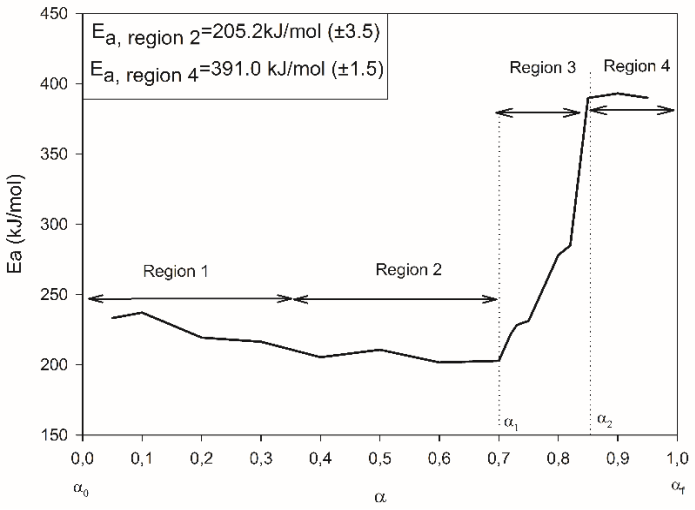

Figure D. 5 Activation energy evolution during clinochlore's decomposition (isoconversional method)

Then, the modeling was performed by model fitting, where the first dehydroxylation step described a second order reaction: $(1-\alpha)^2$ with an activation energy of approximately 231.7 kJ/mol; while the second step was represented by an Avrami-Erofeev model with a reaction order of 1 and an activation energy of 358.9 kJ/mol.

Based on these kinetic evaluations, the overall model was developed. To do so, the first step was limited by the beginning of the dehydroxylation (conversion of 0) and the fractional conversional α_2, while the second step was limited by the fractional conversion α_1 and the end of the reaction. The overall reaction rate of the dehydroxylation of clinochlore was described by Equation D.5.

$$\left(\frac{d\alpha}{dt}\right)_{clin.} = \alpha^*_{clin,1}\left(\frac{d\alpha}{dt}\right)_{step1} + \alpha^*_{clin,2}\left(\frac{d\alpha}{dt}\right)_{step2} \quad [D.5]$$

Where $\alpha^*_{clin,1}$ and $\alpha^*_{clin,2}$ respectively were the fractional conversions, delimiting the start and end of each step respect to the overall dehydroxylation of clinochlore.

The resulting overall study clinochlore's dehydroxylation model can be found in Figure D. 6. The resulted model proved to be inaccurate specially to represent the first decomposition step, which as it was previously mentioned was complicated to developed due to its structure change along the calcination.

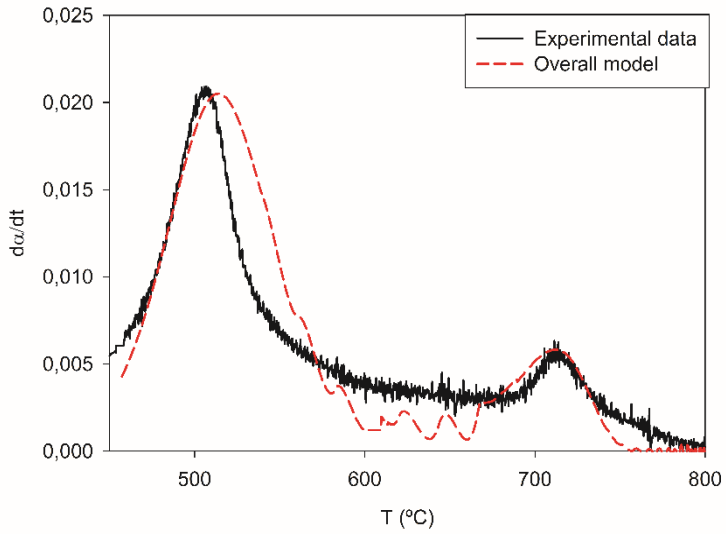

Figure D. 6 Kinetic model validation of clinochlore dehydroxylation in function of the reaction rate

APPENDIX E APPLICATION OF THE CONTRACTING CYLINDRICAL MODEL TO THE KINETIC MODEL

The mixture of many minerals in an ore and in a grain complicates the calcination modeling. In consequence, some assumptions must be made to comprehensively model the effect of the particle size on the calcination of the ore.

As main assumption, due to the mixture of many minerals and by extension many kinetic parameters and models, the ore will be considered as a unique compound. When calcined, the latter produces a gas and a solid product, so that the reaction takes place in the form of Reaction E.1.

$$\vartheta_A A_{(s)} = \vartheta_P P_{(s)} + \vartheta_G G_{(g)} \quad \text{(E.1)}$$

Where A are the minerals contained in the ore, or the ore itself; P are the products from the calcination of the ore, mainly oxides; G are the gases produced during decomposition, mainly CO_2; and the symbol ϑ_i is the stoichiometry of the reactant or product.

The calcination might be considered reversible depending on the sweeping of the gas produced.

As the simplification was defined, it will be assumed that the particles decompose following a contracting cylinder mechanism which is the predominant reaction mechanism of the ore, and describes calcite, dolomite and ankerite calcination. These minerals represent the 76.9 wt.% of the ore and more than 80% of the total conversion of the gas-solid reaction. This model describes the interface reaction control and progress towards the particle's center, while nucleation on the surface of crystals is fast. This same model is representative of the Shrinking Core Model (SCM) with reaction control for cylinder particles with unchanging size described by Octave Levenspiel [48]. The use of this mechanism led to a mathematical expression for the reaction rate (Equation E.1). In this case the reaction rate considered the decomposition of the ore and its reversibility, which as described in literature can be considered as a first order reaction with reference to the CO_2 formed [49].

$$r = 2k(T)C_A^{\frac{1}{2}} - k'C_G^S = 2k(T)[C_A^0(1-X)]^{\frac{1}{2}} - k'C_G^S \quad \text{[E.1]}$$

Where r is the rate of decomposition of the mineral, in mol/(m^2·min); C_G^S is the molar concentration of gas at the reaction interface, in mol/m^3; C_A^0 is the initial molar concentration of mineral in the particle mol/m^3; and k and k' are the constant rate of the reaction and its reversibility respectively

Then, the following assumptions by considering the reaction system were used:

- The minerals within the particles were assumed to react as a unique compound.
- Since particles had a small diameter (below 125 μm), a uniform temperature throughout the particle was assumed.
- As the reaction advanced through the particle, pores were formed resulting at the end of the decomposition in a porous particle.
- The volume of the particle was assumed constant all along the calcination. Therefore, the particle diameter remained unchanged.
- The reaction interface was defined as the available area by the boundary between the ore or minerals (A) and the solid product (P) (Equation E.2)

$$S_i = S_p V_{pA} \quad [E.2]$$

  Where S_i is the reaction interface area, in m^2; S_p is the specific surface area, in m^2/m^3; and V_{pA} the volume of the particle of ore, in m^3.

- As an intrinsic characteristic of the TGA, due to the continuous renewal of the gas in contact with the external particle surface, the outer gas was assumed to have a constant composition.
- With the same reasoning and with the presence of pores in the particle, the gas produced, mainly CO_2, was rapidly removed when it crossed the interface gas/particle surface.
- Since the gas flowrate of the sample and purge gas used in TGA is high (>80 ml/min), the transfer of the produced gas G from the surface of the particle to the gas phase was also assumed to be fast.

Expressing the reaction rate of the ore in mol/min and considering the gas phase concentration to be negligible based on the assumptions regarding CO_2 sweeping off the particles, Equation B.1 could be expressed in the form of Equation E.3.

$$-\frac{dN_A}{dt} = 2\vartheta_A S_p V_{pA} k(T)[C_A^0(1-X)]^{\frac{1}{2}} \quad [E.3]$$

Taking into account the density variation of the reactant along the calcination and applying the mass balance on the reactant, the reaction rate can be expressed in the form of:

$$\frac{dN_A}{dt} = V_{pA}\frac{d\rho_{mA}}{dt} = -V_{pA}\rho_{mA,0}\frac{dX}{dt} \quad [E.4]$$

Where $\rho_{mA,0}$ and ρ_{mA} are the molar density at time t=0 and at time t respectively in mol/m3; and X the degree of conversion of the solid reactant.

Introducing Equation E.4 in Equation E.3 gives:

$$\frac{dX}{dt} = \frac{S_p}{\rho_{mA,0}}\, k(T)[C_A^0(1-X)]^{\frac{1}{2}} \quad \text{[E.5]}$$

By the definition of the concentration, and as the reactant's molar density and concentration can be considered equivalent:

$$\frac{dX}{dt} = \frac{S_p}{(\rho_{A,0}/M_A)^{1/2}} k(T)[(1-X)]^{\frac{1}{2}} \quad \text{[E.6]}$$

Where $\rho_{A,0}$ is the mass density of the reactant A in g/m^3.

By the equivalence between the specific surface area S_p in m^2/m^3 and the specific surface area measured by BET, $S_{p,BET}$, in m^2/g:

$$S_p = S_{p,BET}\rho_{A,0} \quad \text{[E.7]}$$

And the introduction of Equation E.7 in E.6, the final reaction rate that considers the particle size is defined by Equation E.8.

$$\frac{dX}{dt} = \left(\rho_{A,0}M_A\right)^{1/2} S_{p,BET}k(T)f(X) \quad \text{[E.8]}$$

As the units from the reaction rate constant obtained experimentally by TGA for the minerals decomposition ($k'_0(T)$) is in m·s^{-1}, a transformation from the rate constant $k(T)$ of Equation E.9 (in $mol^{0.5}/(m^{1.5}s)$), is necessary:

$$\frac{k_{dpi}}{k_{20\mu m}} = \frac{k'_{0,dpi}}{k'_{0,20\mu m}} \quad \text{[E.9]}$$

It must be noted that $k'_0(T)$ represents the Arrhenius equation in m·s^{-1} while the experimental pre-exponential factor was in s^{-1}. So, based on the development of the contacting cylinder model, the pre-exponential factor can be defined as in Equation E.10:

$$k'_0 = k_0 \frac{d_{p,0}}{2} \quad \text{[E.10]}$$

Where k_0 is the apparent pre-exponential factor in s^{-1} and $\overline{d_{p,0}}$ is the average particle size diameter in m. More details regarding this expression can be found in literature [37].

Considering Equation E.10 and that the kinetic equation of the global model is based on the one developed for particle sizes below to 20 μm, the adimensional coefficient that accounts for the

change of particle size can be described as the ratio between the coefficients of a specific particle size cut and the coefficient of the base model, i.e. 20 m. Therefore, the kinetic equation including a coefficient relating the particle size and the kinetic model can be described as in Equation E.11:

$$\frac{dX}{dt} = \frac{\left((\rho_{A,0}M_A)^{1/2}S_{p,BET}\overline{d_{p,0}}\right)_{dpi}}{\left((\rho_{A,0}M_A)^{1/2}S_{p,BET}\overline{d_{p,0}}\right)_{20\mu m}} K_0(T)f(X) \qquad [E.11]$$

Where, $K_0(T)$ is the reaction rate constant in s^{-1} that can be calculated as: $K_0(T) = k_0 \cdot \exp\left(-\frac{Ea}{RT}\right)$.In this case, the coefficient of the 20 m cut size is approximately equal to 1.

APPENDIX F ARTICLE 3: SUPPLEMENTARY DATA

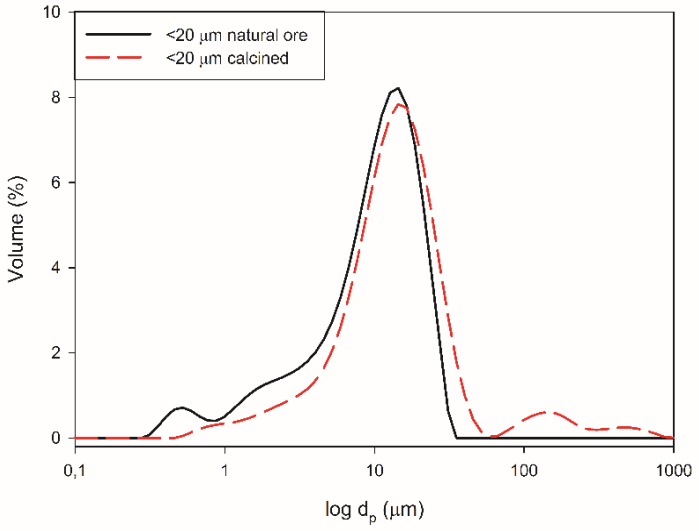

Figure S. 1 Particle size distribution of an ore with particle size below 20 µm before and after calcination

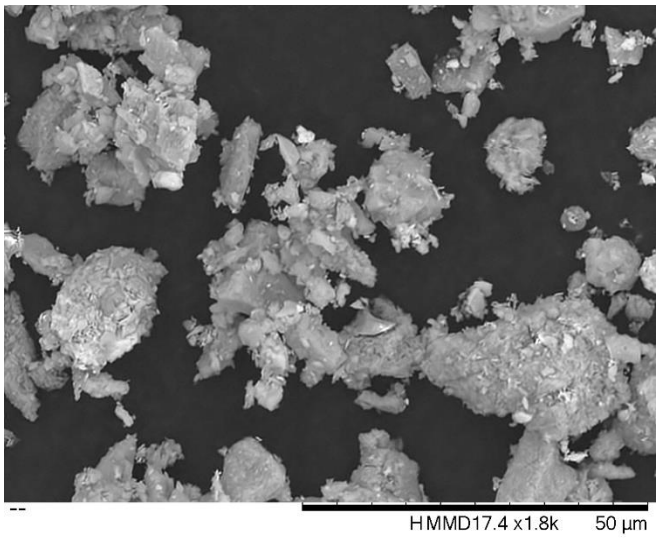

Figure S. 2 SEM picture with agglomeration of particles below 20 µm during calcination

APPENDIX G FLUIDIZED BED SETUPS

Figure G. 1 Fluidized bed thermogravimetric analyzer

Figure G. 2 Induction Heating Fluidized Bed Reactor (IHFBR) Setup